LATENT HARDENING IN PURE MAGNESIUM SINGLE CRYSTALS

LATENT HARDENING IN PURE MAGNESIUM SINGLE CRYSTALS

By Fumiaki Hiura

A Thesis
Submitted to the school of Graduate Studies
in Partial Fulfillment of the Requirements
for the Degree
Master of Science

McMaster University

MASTER OF SCIENCE (2010)
Materials Science ad Engineering

McMaster University
Hamilton, Ontario, Canada

TITLE: Latent Hardening in Pure Magnesium Single Crystals
AUTHORS: Fumiaki Hiura, B.Eng.
SUPERVISOR: Dr. Marek Niewczas

NUMBER OF PAGES: i – xiv, 1 – 101

Abstract

In order to better understand work hardening behavior of pure magnesium, latent hardening experiments with magnesium single crystals were carried out. Large magnesium single crystal samples were first deformed in tension, and subsequently sectioned for secondary tension tests. Three different initial crystallographic orientations of magnesium single crystals were prepared: crystals A and B were oriented for basal <**a**> slip, while crystal C was oriented for $\{10\bar{1}2\}$ twinning. The latent hardening test from type A and B crystals revealed that the LHR in coplanar system arising from basal – basal dislocations interactions was close to unity, whereas the LHR in non-coplanar system arising from basal – 2nd order pyramidal <**c**+**a**> dislocation interactions was around 15. The interactions between $\{10\bar{1}2\}$ twins and various slip dislocations were investigated using type C crystals. It was found that the $\{10\bar{1}2\}$ twins contributed to large strain hardening from at least a dynamic Hall – Petch mechanism. However, the role of $\{10\bar{1}2\}$ twins is complicated and further studies to understand the hardening mechanism due to $\{10\bar{1}2\}$ twinning are necessary.

Acknowledgements

First of all, the author would like to thank my supervisor Dr. Marek Niewczas for his support and encouragement throughout the master program.

The author is also grateful to Dr. Raja. K. Mishra and Mr. Robert Kubic at GM R&D center, Warren, USA for useful discussion and technical assistance with some experiments, especially SEM/EBSD analysis. This study was supported by funding from Initiative for Automotive Manufacturing Innovation (IMAI) at McMaster University.

Finally, I wish to thank Dr. Tatsuya Okada of the University of Tokushima in Japan, for introducing me to Dr. Niewczas and giving me helpful suggestions based on his experience of studying in Japan, Canada, and Denmark.

Table of contents

List of Figures

Chapter 2

Chapter 3

Chapter 4

Chapter 5

List of Tables

Chapter 2

Chapter 3

Chapter 4

Chapter 5

Chapter 1 Introduction

In recent years, utilization of magnesium and magnesium alloys increases in every modern industry and in particular in aircraft and automobile industry, because of the advantageous properties of these materials over other materials used. The important properties of magnesium and magnesium-based alloys, which make them attractive materials for structural applications, are listed below (Kainer, 2003):

- Lowest density of all construction metals at 1.8 g/cm^3
- High specific strength i.e. highest strength to density ratio
- Excellent castability and suitability for pressure die casting
- Easy machining with high cutting speeds
- Highly improved corrosion resistance
- Recyclability, including possibility of integrated recycling.

Along with the advantageous properties, there are some disadvantages to the application of magnesium and magnesium alloys. In magnesium, the $(0001) < 11\bar{2}0 >$ basal <**a**> slip is the dominant deformation mode, because the critical resolved shear stress (CRSS) of the basal <**a**> slip system is much lower of that of non-basal slip systems at room temperature. In general, homogeneous deformation in polycrystalline material requires five independent slip systems (Von Mises criterion). However, basal slip has only two independent slip systems. This gives rise to poor ductility and formability of polycrystalline magnesium and magnesium alloys, thereby limiting their applications. In order to improve the ductility and formability of magnesium and magnesium-based alloys at room temperature, it is necessary to understand the deformation behavior of pure magnesium single crystals through well-designed and systematic studies of their work hardening behavior.

In the present study, the latent hardening tests with magnesium single crystals were carried out to understand the interactions between dislocations of one slip system and those of the other slip system. So far, many latent hardening experiments in FCC crystals have been reported and proved to be one of the most powerful methods for understanding the strength of the interaction between dislocations and their effect on materials properties.

In the following, chapter 2 deals with the literature review pertinent to the present study. A description of the experimental procedure used in the present research is presented in the chapter 3. All the results are given in the chapter 4. Chapters 5 and 6 contain a discussion of the results and the summary of the most important findings of this research work.

Chapter 2 Literature Review

2.1 Slip modes in magnesium

Possible slip systems in HCP crystals are shown in Fig. 2.1 and are listed in Table 2.1. In HCP crystals, the (0001) basal plane is closed-packed and the closed-packed directions are $<11\bar{2}0>$. The shortest lattice vectors are $1/3<11\bar{2}0>$, which corresponds to the unit cell **a**-vectors in the basal plane. Therefore, the most common slip systems in HCP crystals are basal <**a**> slip. However, none of the metals known is ideally close-packed and the lattice parameter ratio c/a, usually deviates from ideal c/a = (8/3)$^{1/2}$ = 1.633, as shown in Table 2.2. This suggests that directionality occurs in inter-atom bonding. In support of this, it is found that some metals such as titanium and zirconium undergo deformation by slip mainly in prism <**a**> system.

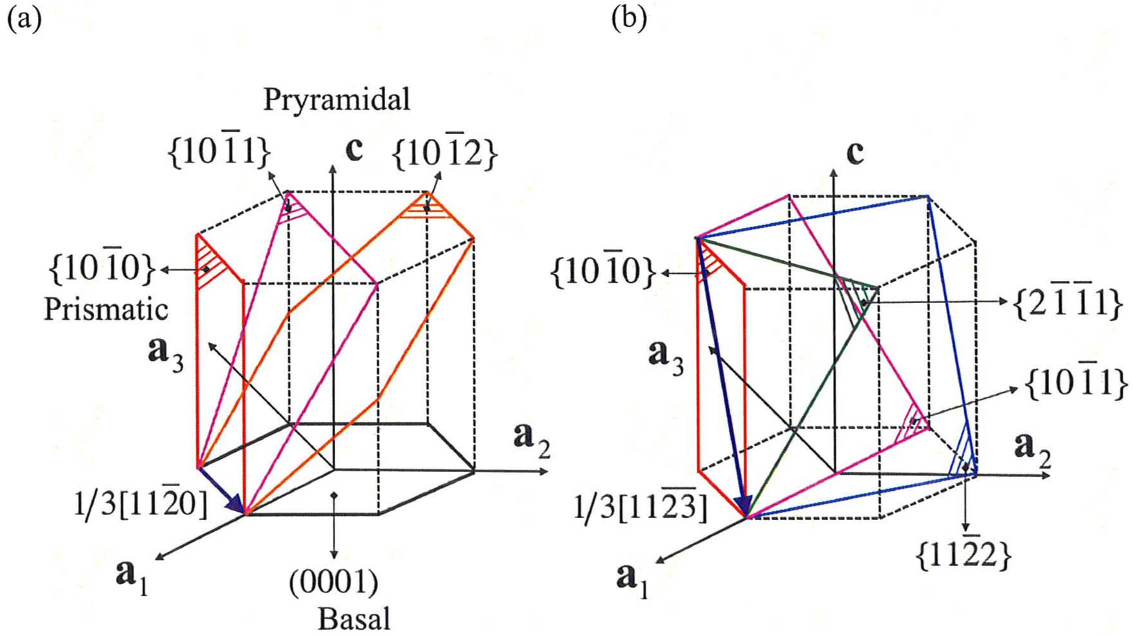

Fig. 2.1 (a) Basal, prismatic, and pyramidal slip systems with <**a**> Burgers vector, and (b) four possible pyramidal slip planes with <**c**+**a**> Burgers vector. (Yoo, 1981)

Table 2.1 Independent Modes of Deformation in HCP Crystals. (Yoo, 1981)

Direction	Plane	Crystallographic Elements	Number of Independent Mode
	Basal	$(0001)<11\bar{2}0>$	2
<**a**>	Prismatic	$\{10\bar{1}0\}<11\bar{2}0>$	2
	Pyramidal	$\{1\bar{1}0l\}<11\bar{2}0>$	4
<**c**>		$\{hki0\}[0001]$	
<**c**+**a**>	Pyramidal	$\{hkil\}<11\bar{2}3>$	5
Twinning		$\{K_1\}<\eta_1>$	0-5

Table 2.2 Properties of some hexagonal closed-packed metals at 300K (Hull and Bacon, 2001).

Metals	Be	Ti	Zr	Mg	Co	Zn	Cd
c/a ratio	1.568	1.587	1.593	1.623	1.628	1.856	1.886
Preferred slip	Basal	Prism	Prism	Basal	Basal	Basal	Basal

In polycrystalline metals, basal <**a**> slip and prism <**a**> slip do not supply sufficient slip modes to satisfy Von Mises' criterion (1928) that every grain should be able to plastic deformation generally to meet the shape changes imposed by its neighbors. According to Von Mises' criterion, five independent slip systems are necessary. In FCC crystals, the twelve $<1\bar{1}0>(111)$ slip systems provide five independent systems and satisfy the condition and so do the slip systems in BCC crystals. However, either basal <**a**> slip or prism <**a**> slip is strongly preferred in HCP crystals. If the two common slip systems are activated simultaneously, they offer only four independent modes between them. Five independent slip systems must be available to carry on arbitrary deformation of a material otherwise, grain-boundary sliding, twinning, or fracture of the crystal will occur. Consequently, non-basal slip systems play an important role in the plastic deformation in HCP crystals because they provide missing deformation modes to fulfill von Mises criterion and requirements for five independent slip systems (Groves and Kelly, 1963).

In magnesium and magnesium alloys, it is important to consider basal <**a**> slip, prism <**a**> slip, and 2nd order pyramidal <**c**+**a**> slip, as shown Fig. 2.2. The temperature dependence of the critical resolved shear stress (CRSS) for basal <**a**> slip, prism <**a**> slip, and 2nd order pyramidal <**c**+**a**> slip in magnesium are summarized in Fig. 2.3. As usually, CRSS is minimum stress to initiate slip, or stress required to initiate slip on a given slip plane and in a given direction. At room temperature, basal <**a**> slip dominates the deformation mechanism because the CRSS for the non-basal slip system such as prism <**a**> slip and 2nd order pyramidal <**c**+**a**> slip are considerably higher than that for basal <**a**> slip. Magnesium shows strong temperature dependent behavior and the CRSS for non-basal systems are decreasing rapidly as temperature rises. Basal <**a**> slip is also the main deformation mechanism at high temperature. In addition to basal <**a**> slip, non-basal slip systems such as prism <**a**> slip, and 2nd order pyramidal <**c**+**a**> slip can be active as secondary slip systems at high temperature. Miura *et. al.* (2005) studied high temperature deformation behavior in magnesium single crystals and reported the activation of prism <**a**> slip and 2nd order pyramidal <**c**+**a**> slip. The role of non-basal slip systems in magnesium will be reviewed in section 2.3.

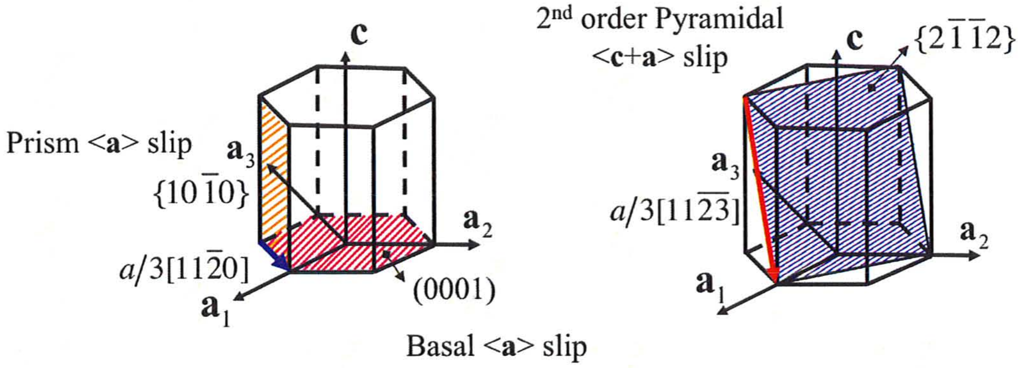

Fig. 2.2 Main slip systems in magnesium: Basal <**a**> slip, Prism <**a**> slip, and 2nd order pyramidal <**c**+**a**> slip.

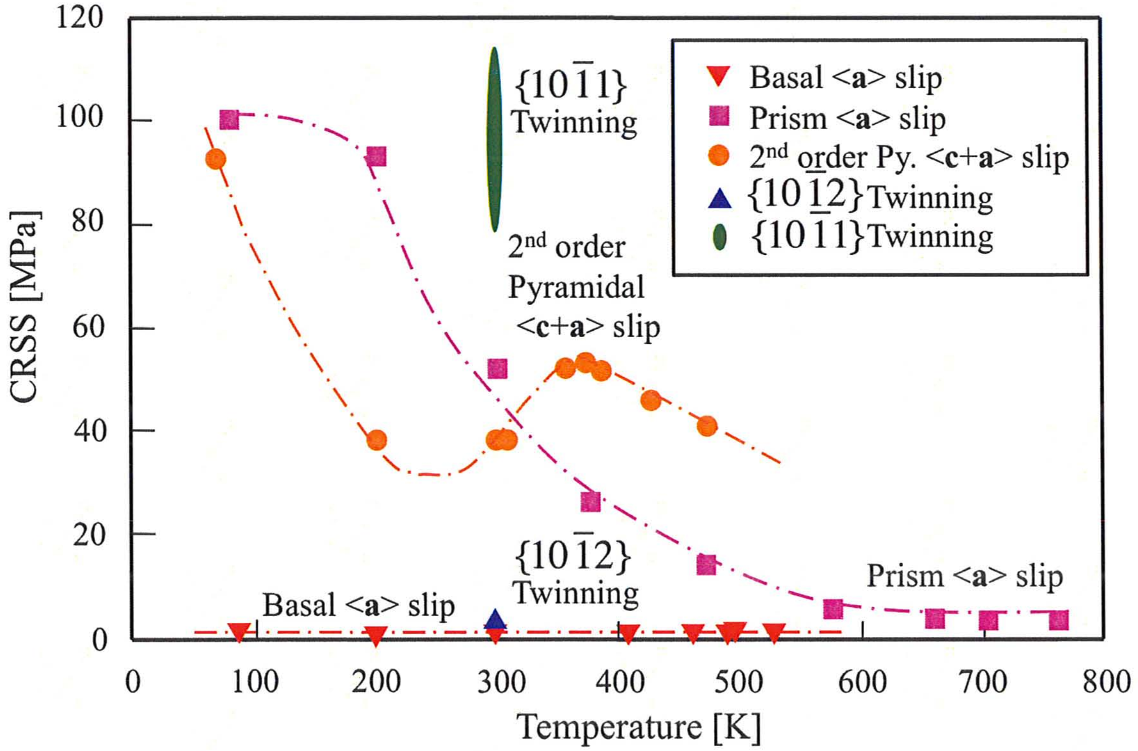

Fig. 2.3 Critical resolved shear stress as a function of temperature for basal <**a**> slip (Sheely and Nash, 1960), prism <**a**> slip (Akhtar and Teghtsoonian, 1969a, 1969b, and 1972; Ward Flynn *et. al.*, 1961), pyramidal <**c**+**a**> slip (Stohr and Poirier, 1972; Obara *et. al.*, 1973), $\{10\bar{1}2\}$ twin (Reed-Hill and Robertson, 1957; Miura, 2004), and $\{10\bar{1}1\}$ twin (Yoshinaga and Horiuchi, 1963a; Wonsiewicz and Backofen, 1967).

2.2 Deformation twinning in magnesium

Twinning is a particularly important deformation mechanism when there are only a limited number of slip systems in HCP crystals. At the beginning, the crystallography elements of deformation twinning are introduced. In the classical theory, deformation twins can be formed by homogeneous shear, s, in the original (parent) lattice. As a result, the product (twinning) lattice has the same crystal structure as the original one and the two lattices have specific crystallographic relationships. Deformation twins are characterized as the parameters of K_1, K_2, η_1, and η_2, called twinning elements, as depicted in Fig. 2.4. K_1 is the invariant plane of twinning shear and η_1 is the shear direction. The most commonly observed twin systems in HCP crystals are summarized in Table 2.3.

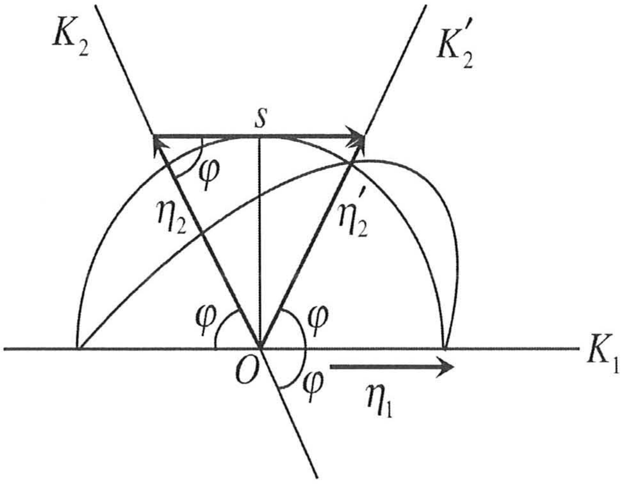

Fig. 2.4 Geometry relationships between twinning elements: K_1, K_2, η_1, and η_2.

Table 2.3 Crystallographic elements and parameters of twin systems in HCP crystals (Yoo, 1981).

K_1	K_2	η_1	η_2
$\{10\bar{1}2\}$	$\{10\overline{12}\}$	$\pm<10\bar{1}\bar{1}>$	$\pm<10\bar{1}1>$
$\{10\bar{1}1\}$	$\{10\overline{13}\}$	$<10\overline{12}>$	$<30\bar{3}2>$
$\{11\bar{2}2\}$	$\{11\overline{24}\}$	$\frac{1}{3}<10\overline{23}>$	$\frac{1}{3}<22\bar{4}3>$
$\{11\bar{2}1\}$	(0002)	$\frac{1}{3}<\bar{1}\bar{1}26>$	$\frac{1}{3}<11\bar{2}0>$

In magnesium and magnesium alloys, $\{10\bar{1}2\}$ twin (**c**-axis tension type) and $\{10\bar{1}1\}$ twin (**c**-axis compression type) are usually observed as depicted in Fig. 2.5. Generally, the twin types formed in HCP crystals depend on the direction of internal twinning stress with respect to the **c**-axis of HCP lattice. In the case of magnesium, it is expected that $\{10\bar{1}2\}$ twin is formed when tensile stress is applied along the **c**-axis, while $\{10\bar{1}1\}$ twin is formed when compression stress is applied along the **c**-axis, shown in Fig. 2.5 (Partridge, 1967; Yoo, 1981).

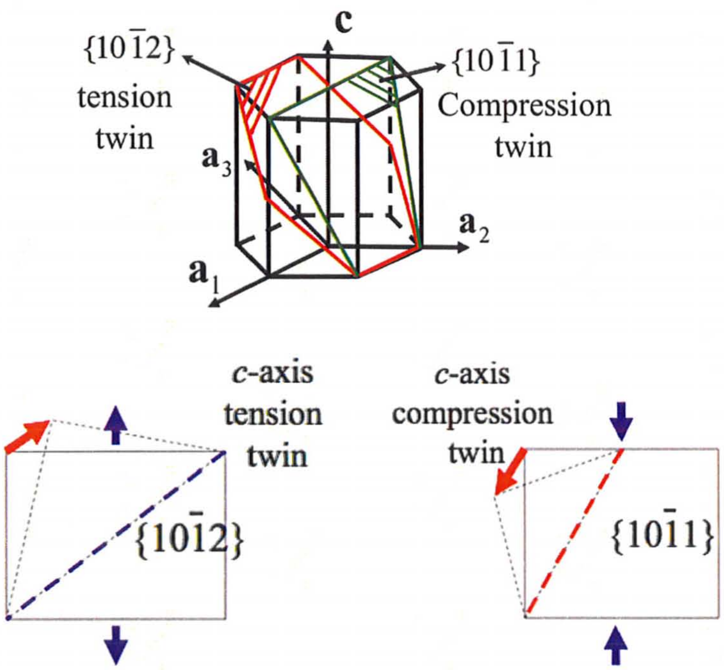

Fig. 2.5 The most common twin modes in magnesium: $\{10\bar{1}2\}$ twin (**c**-axis tension type) and $\{10\bar{1}1\}$ twin (**c**-axis compression type).

Ductile HCP metals such as titanium and zirconium form both type of twins by following the geometrical condition (Yoo, 1981). However, magnesium does not satisfy this geometrical condition. In fact, Wonsiewicz and Backofen (1967) observed $\{10\bar{1}2\}$ twins in the compression samples parallel to **c**-axis. $\{10\bar{1}2\}$ twins are also formed in polycrystalline magnesium and magnesium alloys without any relationship to the tensile direction (Asada and Yoshinaga, 1958; Barnett *et. al.*, 2004; Yang *et. al.*, 2004). The ease of $\{10\bar{1}2\}$ twin formation can be attributed to its small CRSS. It is reported that the CRSS of the $\{10\bar{1}2\}$ twins is only 2 – 3 MPa (Reed-Hill, 1957) or 2.7 – 2.8 MPa (Miura, 2004), the second smallest next to the CRSS of basal <**a**> slip. Another aspect of $\{10\bar{1}2\}$ twin is the accommodation of the stress concentration caused by anisotropic dislocation plasticity due to single basal <**a**> slip (Yang *et. al.*, 2004). Furthermore, the $\{10\bar{1}2\}$ twin can largely contribute to strain hardening for the following reasons:

- $\{10\bar{1}2\}$ twin introduce additional interfaces and the twin boundaries can act as barriers to dislocation motion.
- $\{10\bar{1}2\}$ twin accompany the rotation of **c**-axis by 86° along **a**-axis. Therefore, there is no big difference of resolved shear stress in basal <**a**> slip system between the matrix and the twin.
- Basal <**a**> dislocation with screw component in the matrix can cross-slip into the basal plane in the $\{10\bar{1}2\}$ twin. For example, basal slip bands across twin boundaries were often observed in magnesium single crystals as shown in Fig. 2.6 (Yoshinaga and Horiuchi, 1962).

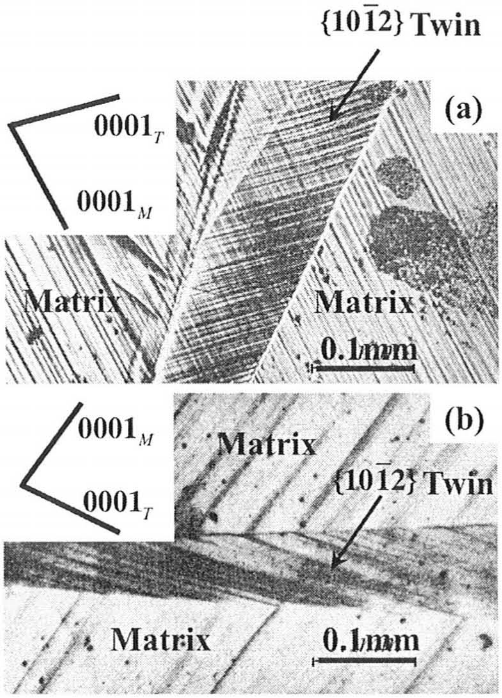

Fig. 2.6 (a) Many basal <**a**> slip traces visible inside $\{10\bar{1}2\}$ twin region. (b) The interface of basal <**a**> slip lines in both matrix and twin on the $\{10\bar{1}2\}$ twin boundaries (Yoshinaga and Horiuchi, 1962).

As described above, many studies of $\{10\bar{1}2\}$ twin have been carried out. In contrast, many questions about $\{10\bar{1}1\}$ twin still remain open. It is very difficult to measure the CRSS for the $\{10\bar{1}1\}$ twin accurately. So far, it has been reported that the CRSS for the $\{10\bar{1}1\}$ twin was much higher than that of $\{10\bar{1}2\}$ twin, 76 – 153 MPa (Wonsiewcz *et. al.*, 1967) or 114 MPa (Yoshinaga and Horiuchi, 1963). The role of $\{10\bar{1}1\}$ twin is different from that of $\{10\bar{1}2\}$ twin. As written above, the role of $\{10\bar{1}2\}$ twin appears to be the accommodation of the stress concentration caused by anisotropic basal dislocation, while the role of $\{10\bar{1}1\}$ twin have been reported to cause fracture (Read-Hill, 1957; Yoshinaga and Horiuchi, 1963; Wonsiewcz *et. al.*, 1967).

2.3 Plastic deformation behavior in magnesium single crystals

2.3.1 Homogeneous deformation by basal single slip

In magnesium single crystal, basal <**a**> dislocation slip is activated dominantly at room temperature. Tensile deformation behaviors of magnesium single crystals having basal orientation were widely reported by Burke and Hibbard (1952), Basinski (1960), Asada and Yoshinaga (1961), Hirsh and Lally (1965), and Bhattacharya (2006). When the Schmid factor for basal slip is closed to 0.5, homogeneous deformation by single basal slip occurs. According to Hirsh and Lally (1965), the angle between the slip direction and the tensile axis should be between 40° to 60° to avoid geometrical softening and inhomogeneous deformations. Fig. 2.7 shows the typical shear stress – shear strain curve for basal single slip obtained from Hirsch and Lally's experiments.

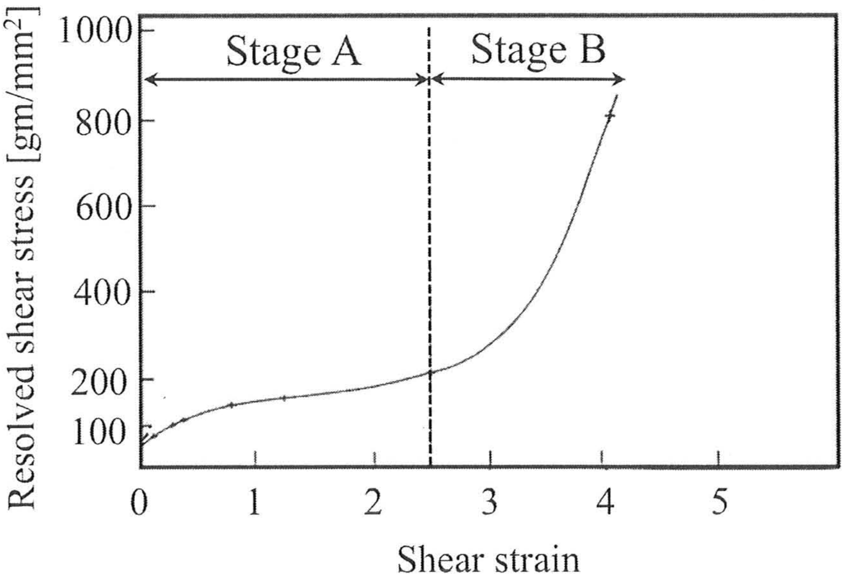

Fig. 2.7 Stress – strain curve for magnesium single crystals oriented for basal slip at room temperature (Hirsch and Lally, 1965).

The flow stress characteristic was divided into two stages of deformation according to the similar work hardening rate: Stage A (low work hardening range) and Stage B (rapid work hardening range). The main features and the mechanism of deformation in these two stages of deformation based on Hirsch and Lally's works are as follows:

Stage A

The range of stages A (easy glide stage) in magnesium single crystal oriented for basal slip extends until 250% deformation. The working hardening in this stage is about 2 x 10^{-5} μ, where μ is the shear modulus of magnesium. They observed dislocation distribution in single crystals by transmission electron microscopy (TEM) and proposed the following mechanism for this stage:

- The dislocations from the sources operating simultaneously trap one another and form dipole bands for edges and screws.

- The screw dislocations cross-slip and annihilate leaving the edge dislocation and the excess of the screws of the same sign. The flow stress in this stage is controlled by the internal stress field from edge clusters, residual screw dislocations and dislocations with non-primary Burgers vectors.
- The work hardening rate in stage A is very low because most of the dislocations annihilate or form dipoles, which have relatively small interaction radii with the mobile dislocation and therefore contribute little to the hardening effect.
- The density of the obstacles in this stage rises very slowly as the deformation proceeds.

Stage B

In this stage the work hardening rate of the crystal is typically 6 x 10^{-4} μ. The main feature of stage B is characterized as follows:

- Stage B is characterized by twinning formations, the production of dislocation tangles and the dislocation network in which three basal Burgers vectors are equally represented.
- In stage B, hardening is mainly due to the interaction between the dislocations in the basal plane. The glide of non-primary dislocations with Burgers vectors in the basal plane gives rise to the formation of hexagonal networks of dislocations on the basal plane.
- In stage B, high density of twins is observed near the fracture surface of the samples.

2.3.2 Inhomogeneous deformation

As reviewed in the previous section, there is a narrow range of orientations where plastic deformation occurs homogeneously by single slip basal system. When basal slip becomes difficult, inhomogeneous deformation, characterized by deformation bands, called kink bands, and $\{10\bar{1}2\}$ twins takes place (Burke and Hilbbard, 1952; Yoshinaga and Horiuchi, 1962). Deformation starts locally, typically in the middle part of the sample, with bending and twisting stress due to inhomogeneous deformation. In this case, $\{11\bar{2}0\}$ type kink bands are formed along the boundary of the inhomogeneous deformation. As the inhomogeneous deformation proceeds further, the kink bands accompanied by many $\{10\bar{1}2\}$ twins occur. It is very important to understand whether the kink bands are mobile or immobile for strain hardening. At the beginning stage of inhomogeneous deformation, the kink bands are relatively mobile. The kink bands forms symmetrical tilt boundaries composed of parallel edge dislocations. It is well known that those dislocations are highly mobile (Washburn and Parker, 1952). Therefore, in this stage the kink bands show little effect on the strain hardening. However, the kink bands accompanied with many $\{10\bar{1}2\}$ twins do not migrate during further deformation. Small pile-up of basal dislocations causes to produce $\{10\bar{1}2\}$ twins. If the kink bands are locked with the $\{10\bar{1}2\}$ twins, the kink bands tend to become immobile and can work as strong obstacle to gliding dislocation. Fig. 2.8 shows the schematic illustration of the kink bands with many $\{10\bar{1}2\}$ twins. By further kink bands formation and $\{10\bar{1}2\}$ twins formation, rapid hardening stage starts in the case of inhomogeneous deformation.

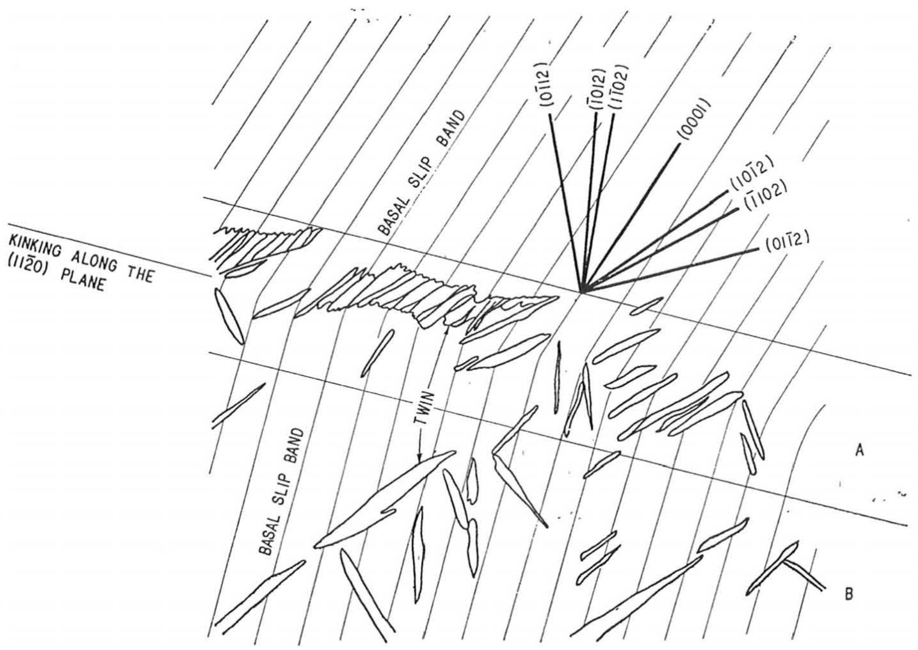

Fig. 2.8 Schematic illustration of [11$\bar{2}$0] kink bands with many {10$\bar{1}$2} twins (Yoshinaga and Horiuchi, 1962).

2.3.3 Deformation by 2nd order pyramidal <**c**+**a**> slip

The activation of 2nd order pyramidal <**c**+**a**> slip has been observed in **a**-axis tension test or **c**-axis compression test of magnesium single crystals (Read-Hill and Robertson, 1957; Yoshinaga and Horiuchi, 1963a and 1963b; Stohr and Poirier, 1972; Obara *et. al.*, 1973; Ando *et. al.*, 1992) and magnesium – lithium alloy single crystals (Ando and Tonda, 2000). The CRSS for 2nd order pyramidal <**c**+**a**> slip in magnesium is strongly temperature and strain rate dependent, as shown in Fig. 2.3.

Recently, Ando's group studied deformation behavior by 2nd order pyramidal <**c**+**a**> slip in magnesium single crystals (Ando *et. al.*, 1992) and magnesium – lithium alloy single crystals (Ando and Tonda, 2000) stretched in the **a**-axis direction and reported anomalous yield stress behavior of 2nd order pyramidal <**c**+**a**> slip at a low temperature rage of 77 to 293 K. Fig. 2.9 (a) shows the initial orientations of magnesium single crystals and Mg – Li alloy single crystals with respect to HCP unit cell they produced. Fig. 2.9 (b) and Fig. 2.10 (a) show mechanical properties of magnesium single crystals and Mg – Li alloy single crystals oriented for 2nd order pyramidal <**c**+**a**> slip in the temperature ranges from 77K to 293K, respectively. Fig. 2. 10 (b) shows temperature and additional lithium dependence of the yield stress of magnesium single crystals and Mg – Li alloy single crystals. The conclusions obtained from Ando's experimental results are summarized as follows:

- The yield stress due to 2nd order pyramidal <**c**+**a**> slip tends to increase with increasing temperature from 77K to 293K in both magnesium single crystals and Mg – Li alloy single crystals.
- The yield stress due to 2nd order pyramidal <**c**+**a**> slip in both magnesium single crystals tends to decrease with adding to lithium.

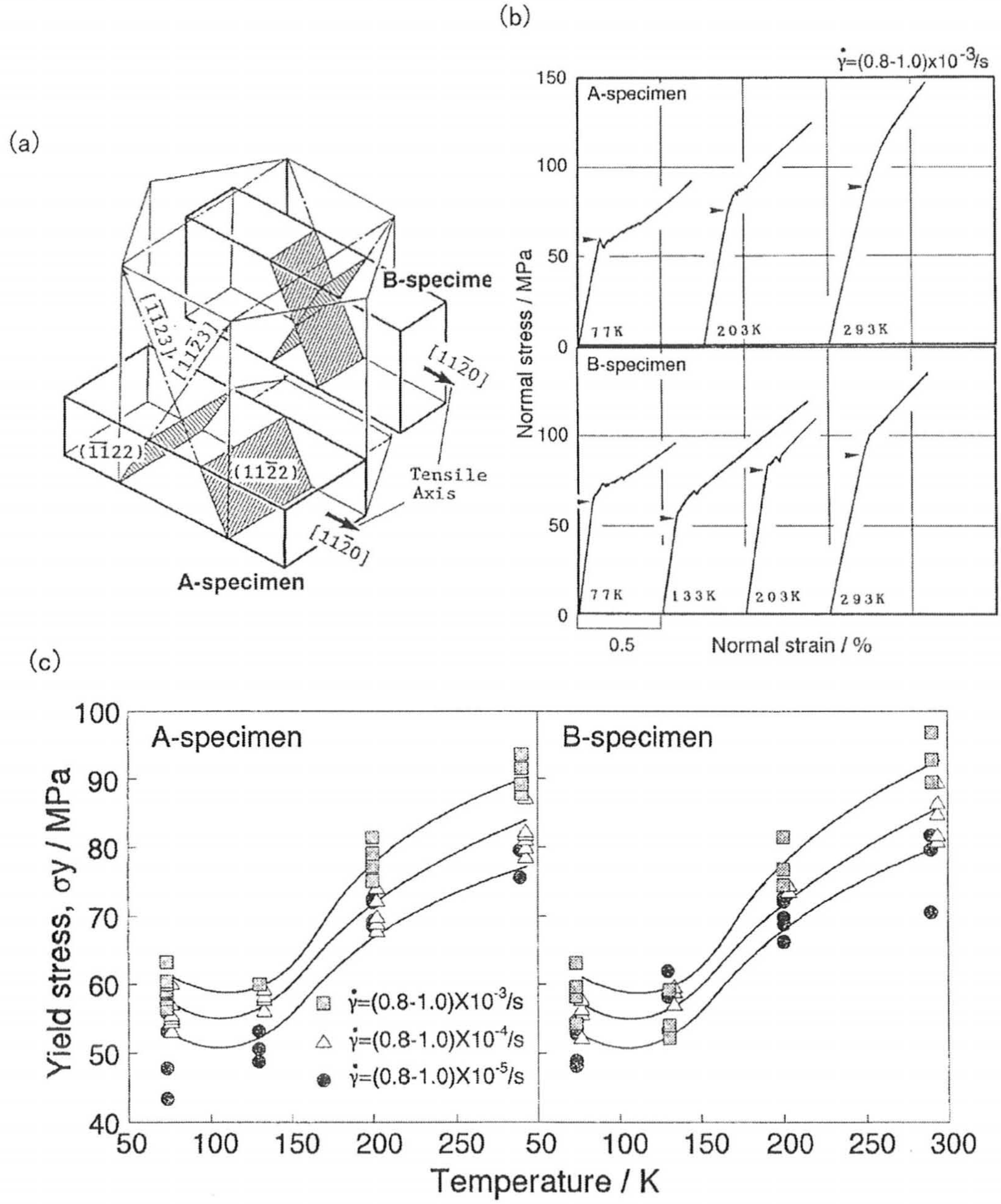

Fig. 2.9 (a) Orientation of A-type and B-type specimens relative to HCP unit cell, (b) Stress – strain curves in magnesium single crystals with various temperatures from 77K to 293K, (c) Temperature and strain rate dependence of the yield stress in magnesium singe crystals (Ando *et. al.*, 1992).

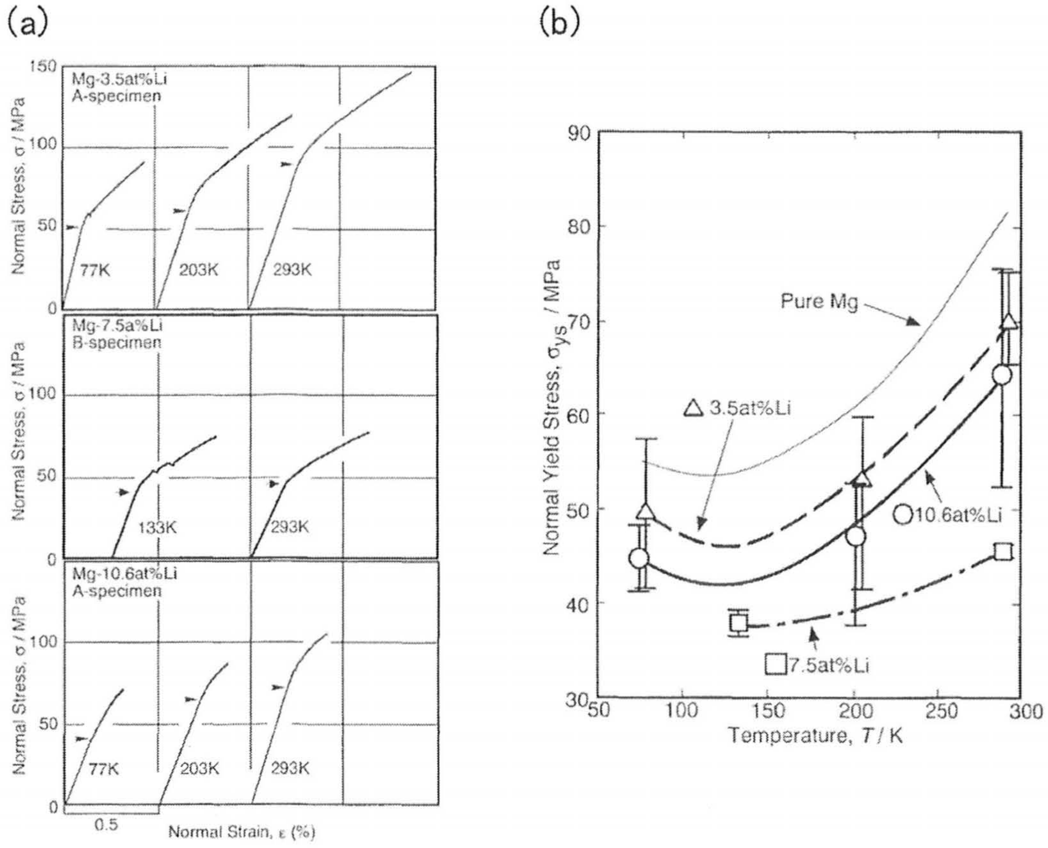

Fig. 2.10 (a) Stress – strain curves in magnesium – lithium alloy single crystals with various temperatures from 77K to 293K, (b) Temperature and additional lithium dependence of the yield stress of magnesium single crystals and magnesium – lithium alloy single crystals (Ando and Tonda, 2000).

The activation of only 2nd order pyramidal <**c**+**a**> slip has been also observed in the **c**-axis compression tests. Yoo *et. al.* (2002) discussed the temperature dependence of the CRSS for 2nd order pyramidal <**c**+**a**> slip using experimental results in their review paper, as shown in Fig. 2.11. Ando *et. al.* proposed that the yield stress due to 2nd order pyramidal <**c**+**a**> slip in magnesium single crystals and Mg – Li alloy single crystals was directly proportional to the low temperature range 77K to 293K (Ando *et. al.*, 1992; Ando and Tonda, 2000). However, the yield stress due to 2nd order pyramidal <**c**+**a**> slip tends to decrease at higher temperature region after reaching to the maximum CRSS around $T/T_m \sim 0.3 - 0.4$ according to **c**-axis compression tests by Obara *et. al.* (the temperature range: 298K – 673K) and Stohr and Poirier (the temperature range: 77K – 470K).

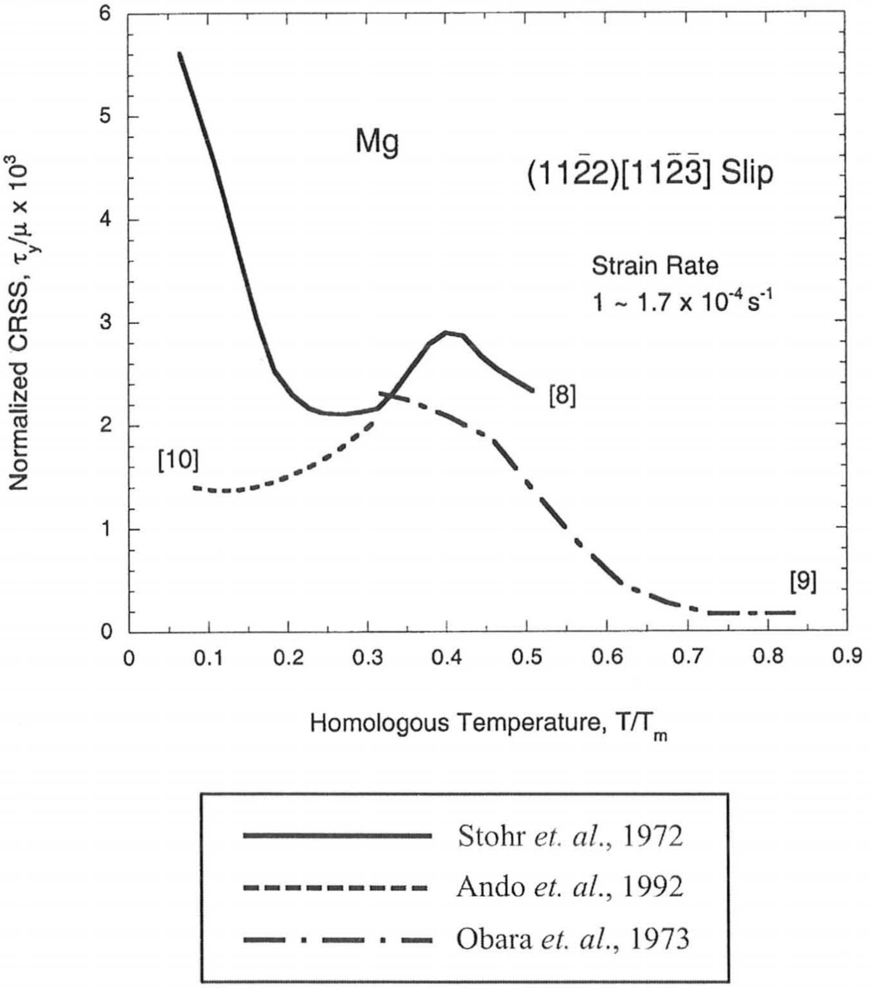

Fig. 2.11 Temperature dependence of the CRSS for 2nd order pyramidal <**c**+**a**> slip, normalized to the shear modulus at room temperature (μ = 17GPa for magnesium) in magnesium single crystals (Yoo *et. al.*, 2002).

In order to understand influence of 2nd order pyramidal <**c**+**a**> slip in magnesium and magnesium alloys on the hardening behavior, numerous theoretical and experimental studies and more recently molecular dynamic (MD) simulation have been published –

e.g., TEM studies (Obara *et. al.*, 1973; Stohr and Poirier, 1972; Ando *et. al.*, 1992; Agnew *et. al.*, 2002), theoretical mechanism such as cross-slip mechanism (Yoo *et. al.*, 2001) and MD simulation (Ando *et. al.*, 1996 and 2002). However, there are still many questions about 2nd order pyramidal <**c**+**a**> slip to be answered. The present author strongly believes that experimental approach involving latent hardening test in magnesium single crystals, will give rise to the better understanding to 2nd order pyramidal <**c**+**a**> slip in magnesium.

Finally, one must keep in mind that the very accurate initial orientation control is necessary in order to obtain only 2nd order pyramidal <**c**+**a**> slip in a magnesium single crystal. In fact, Stohr and Poirier (1972) reported that basal <**a**> slip occurred in the **c**-axis compression test in spite of a very small Schmid factor (< 0.035) and claimed "in order to obtain pure conditions of 2nd order pyramidal <**c**+**a**> slip, the angle between the applied stress and the **c**-axis must be set less than 5 arc minutes."

2.4 Latent hardening test

Work hardening is the phenomenon in which deformation on one active plane becomes more difficult and a higher stress is necessary to continue the deformation when a crystal is deformed in one slip plane. During work hardening on one slip system, other potential slip systems are largely inactive or latent. However, the potential (latent) slip systems are also hardened by dislocation pile-up and arrangement on the primary slip. This phenomenon is called latent hardening. Taylor and Elam (1925) first noticed that plastic flow stress on one active plane caused either the same or a slightly greater hardening on an inactive one in deformed aluminum crystal having FCC structure. Then, similar phenomena or latent hardening behavior was observed and reported in other crystals such as BCC (Nakada and Keh, 1966; Keh and Nakada, 1967), HCP (Edwards *et. al.*, 1953; Edwards and Washburn, 1954; Phillips Jr. and Robertson, 1958; Phillips Jr., 1961), and ionic crystals (Alden, 1963 and 1964).

In order to investigate the latent hardening behavior, there is a conventional method called latent hardening test. Figure 2.12 (a) and (b) show schematic illustration of this kind of experimental procedure. In this test, two consecutive deformations are needed on a single crystal. The method involves a large single crystal, so-called parent crystal, is slightly deformed in tension, restricted to the stage I or easy-glide region, and then smaller samples, called secondary samples, are cut at various angles from the pre-deformed parent crystal and then subjected to the secondary tensile or compression tests. Now, we must pay attention that secondary samples are chosen as dislocations on latent systems will be activated and interact with those on the primary system during secondary deformation. In order to describe latent hardening behavior, a latent hardening ratio (LHR), defined as follows, was introduced by Jackson and Basinski (1965) and have been widely used by many researchers. If a crystal is predeformed to a flow-stress σ_1, the glide system is changed and the initial flow-stress on the secondary system is σ_2, as shown in Figure 2. 12 (c), then the LHR is given by:

$$LHR = \frac{\sigma_2}{\sigma_1} \quad \ldots (2.1).$$

Measuring and comparing the plastic flow stress, work hardening rate, and LHR in the different tests can give us information about hardening behavior in various slip systems, namely self hardening or latent hardening.

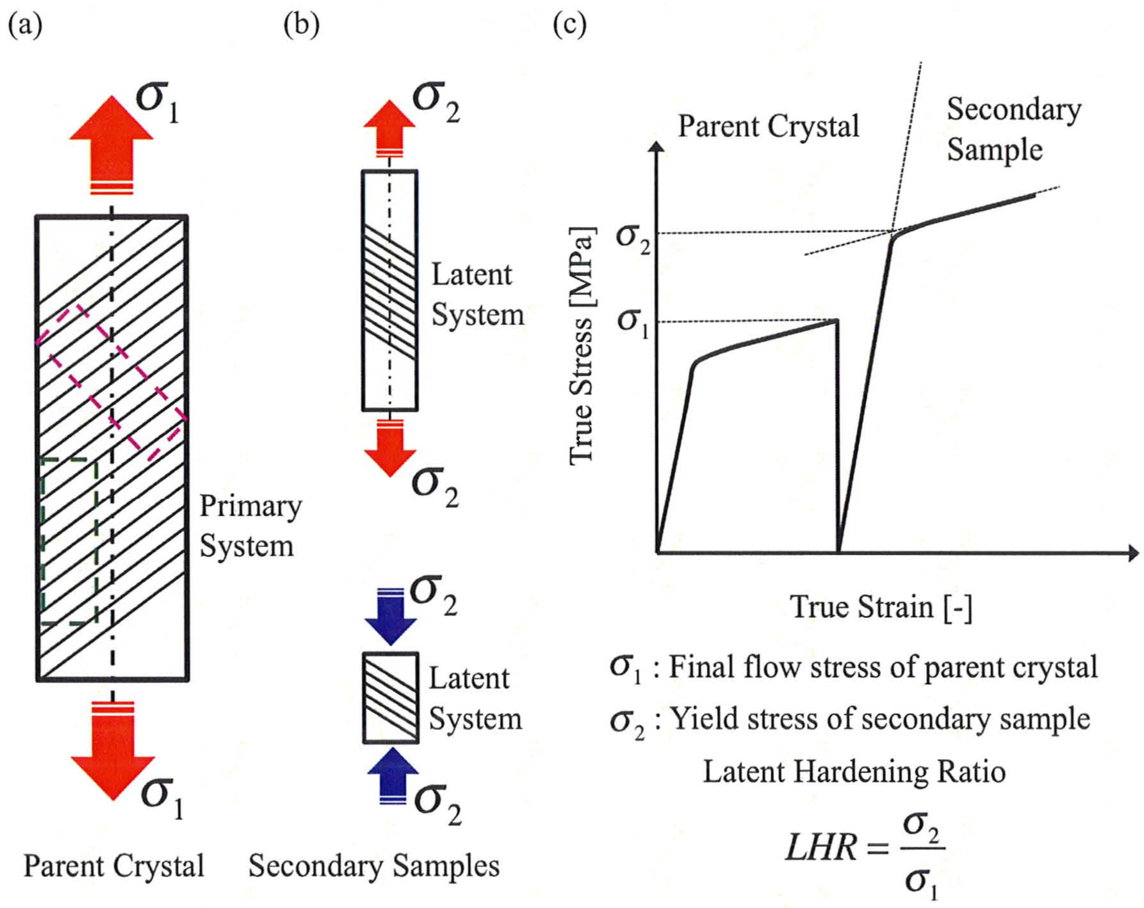

Fig. 2. 12 Experimental procedure and notation of latent hardening test: (a) deformation of parent crystal in tension, (b) deformation of secondary sample in tension and compression, and (c) the definition of latent hardening ratio.

Latent hardening test in FCC crystals have been extensively studied such as copper (Jackson and Basinski, 1965; Franciosi *et. al.*, 1980), aluminum (Kocks, 1964; Kocks and

Brown, 1965; Lake and Craig, 1972; Miyamoto *et. al.*, 1977; Franciosi *et. al.*, 1980), silver (Kocks, 1964; Ramaswami *et. al.*, 1965), copper – aluminum alloy (Wessels and Jackson, 1969; Wessels and Nabarro, 1971), silver – gold alloy (Ramaswami *et. al.*, 1965), and aluminum – magnesium alloy (Wu *et. al.*, 1997).

In the following, the general conclusions for latent hardening test in FCC crystals will be reviewed. The slip systems in FCC crystals are represented by the Schmid and Boas notation (1935), as shown Fig. 2.13 and Table 2.4. The active system in the primary test is always B4 in latent hardening test. Fig. 2.14 shows that latent systems that have comparable LHRs are in a symmetrical situation with respect to B4 (primary system) in Thomson's tetrahedral. The interactions of two dislocations can be categorized into six groups by geometrical arrangement of the Burgers vectors of the two dislocations (Baird and Gale, 1965; Franciosi *et. al.*, 1980; Hirth and Lothe, 1982). The six types of dislocation interaction are as follows:

(i) Sessile Junction (Lomer – Cottrell sessile locks) in systems A6 and C1;

(ii) Glissile attractive junctions in systems A2, C5, D1, and D6;

(iii) Hirth lock formation in systems A3 and C3;

(iv) Cross-slip in system D4;

(v) Coplanar systems in B2 and B5;

(vi) Self hardening in system B4.

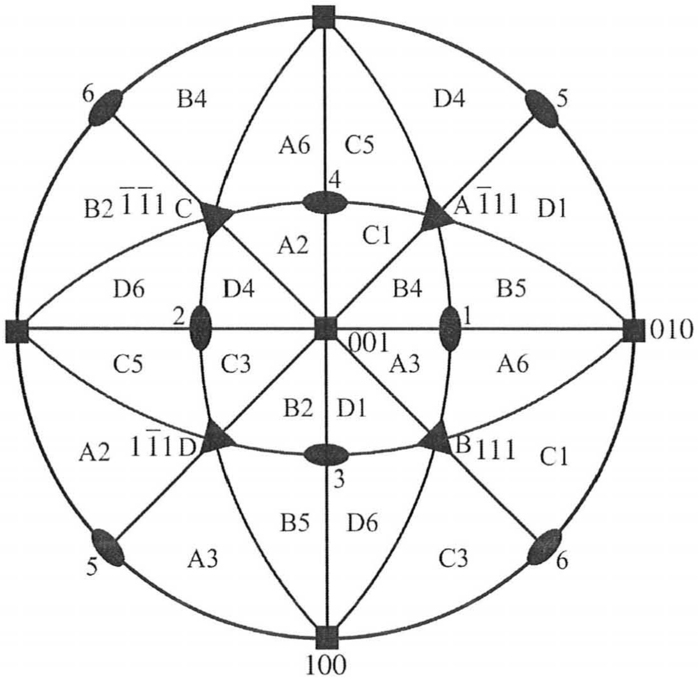

Fig. 2. 13 A stereographic projection of a cubic crystal showing various slip systems.

Table 2.4 Schmid and Boas notation for the slip systems in cubic crystals. (Schmid and Boas, 1935).

Primary system	B4	$(111)[\bar{1}01]$
	B5	$(111)[\bar{1}10]$
	B2	$(111)[0\bar{1}1]$
Conjugate system	C1	$(1\bar{1}\bar{1})[011]$
	C5	$(1\bar{1}\bar{1})[1\bar{1}0]$
	C3	$(1\bar{1}\bar{1})[101]$
Cross-glide system	D4	$(1\bar{1}1)[\bar{1}01]$
	D1	$(1\bar{1}1)[011]$
	D6	$(1\bar{1}1)[110]$
Critical system	A3	$(\bar{1}11)[101]$
	A6	$(\bar{1}11)[110]$
	A2	$(\bar{1}11)[0\bar{1}1]$

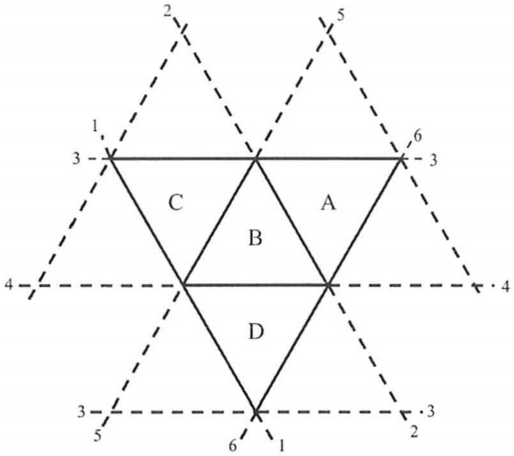

◆ Junctions with B4 (Primary system)
- Lomer – Cottrell Lock: A6 and C1
- Glissile Junctions: A2, C5, D1, and D6

◆ No Junctions with B4 (Primary system)
- Coplanar: B2 and B5
- Cross-slip: D4
- Hirth lock: A3 and C3

Fig. 2.14 Thomson tetrahedral and junction formation with primary system B4 (Franciosi *et. al.*, 1980).

If the slip plane is the same in the secondary test as that in the primary test, defined as a coplanar slip system, the flow stress is almost unchanged, while if the slip plane is changed, defined as a non-coplanar slip system, the flow stress is increased. From the LHR point of view, the LHRs of non-coplanar system such as group (i) to (iv) are generally greater than those of the coplanar systems such as group (v) and (vi). Furthermore, there are general conclusions about LHR. LHR initially increases and then decreases with pre-strain and reaches a constant value at large pre-strain. Jackson and Basinski (1965) found that LHRs on non-coplanar systems varied from 2.5 in stage I to 1.4 in stage II in copper single crystals, depending on the pre-strain. Similar behavior was observed in FCC type alloys, for example, copper – aluminum alloys (Wessels and Jackson, 1969). Franciosi *et. al.* (1980) found that LHR first increases from unity to a peak values (1.6 – 2.2 for aluminum and roughly twice higher than aluminum for copper), where the peak values occur at pre-strains of up to 0.2% and then decrease rapidly towards a residual value higher than unity at large strain (1.3 for aluminum and 1.5 for copper).

Later, some researchers (Franciosi and Zaoui 1982; Franciosi, 1985; Ohashi 1994) proposed hardening law in FCC single crystals based on self hardening and latent hardening behavior, in which both the density of mobile dislocations in the primary system and the density of immobile dislocations in the secondary systems were taken into account. This theoretical approach gave rise to more accurate hardening law than the conventional hardening law based on Schmid law in the case of multi-slip situation.

In contrast, there is a little data available concerning the latent hardening behavior in HCP crystals. However, latent hardening test in coplanar systems have been studied only by pure shear tests on various HCP metals by using zinc, magnesium, and cadmium single crystals (Edwards *et. al.*, 1953; Edwards and Washburn, 1954; Phillips Jr. and Robertson, 1958). A thin sheet of single crystals is prepared for latent hardening test by pure shear. In pure shear test, it is possible to test only the coplanar latent systems by the shear method because of severe shape restriction. In this experiment, a sheet of single crystal is deformed in one of the slip directions in the primary plane, corresponding to $<110>$ direction in FCC crystals and $<2\bar{1}\bar{1}0>$ direction in HCP crystals, and then, shearing is continued on another slip direction at 60^o, 120^o, 180^o to the first, followed by another change in slip direction. In HCP crystals, LHR increase up to 1.24 when shear direction changes to 60^o, 120^o directions, while LHR is lower than 1, when shear direction changes to 180^o direction. In other words, HCP crystals tend to be softer on stress reversal.

2.5 Objectives of the work

The importance of latent hardening test was reviewed in section 2.4. The important role of dislocations interactions in strain hardening in crystalline materials has been known for decades and in the particular case of FCC single crystals has been confirmed by latent hardening experiments. Although latent hardening test in HCP crystals by pure shear test was studied, there is little information available on latent hardening behavior in HCP crystals. Therefore, this study represents a first step to understand latent hardening behavior in HCP crystals.

Early studies about plastic deformation behavior in magnesium single crystals were described in section 2.3. Unlike FCC crystals, basal <**a**> sip is a dominant mode of plastic flow at room temperature in magnesium single crystals due to the lower symmetry of HCP structure. However, many studies of the activation of 2nd order pyramidal <**c**+**a**> slip have been reported in magnesium single crystals with the special orientation as written in section 2.3.3, which means that it is possible to study the interaction between basal <**a**> dislocation and 2nd order pyramidal <**c**+**a**> dislocation when the orientation of secondary samples is accurately controlled in latent hardening tests in magnesium single crystals.

The purpose of this study is to provide the first experimental data on the latent hardening behavior of magnesium single crystals and to determine the latent hardening ratio (LHR) for selected dislocation-dislocation and dislocation-twin interactions in magnesium single crystals by measuring and comparing the flow stresses in different latent hardening tests.

Chapter 3 Experimental Procedure

3.1 Preparation of the magnesium single crystals

High purity 99.995% magnesium single crystals were produced by a modified Bridgeman technique. The crystals were grown using a split mould made of high purity graphite coated uniformly with boron nitride. Thin boron nitride layer on the mold surface prevents reaction of liquid magnesium with the mold surface. Fig. 3.1 shows picture and schematic illustration of the graphite mold. Single crystal nucleus with known orientation was placed at the bottom of the mould and was used to grow a predetermined orientation of the crystals for experiments. The dimension of nucleus was 3mm x 3mm x 20mm. High purity magnesium ingot obtained from Timminco Metals (Ontario, Canada) was placed at the top part of the mold.

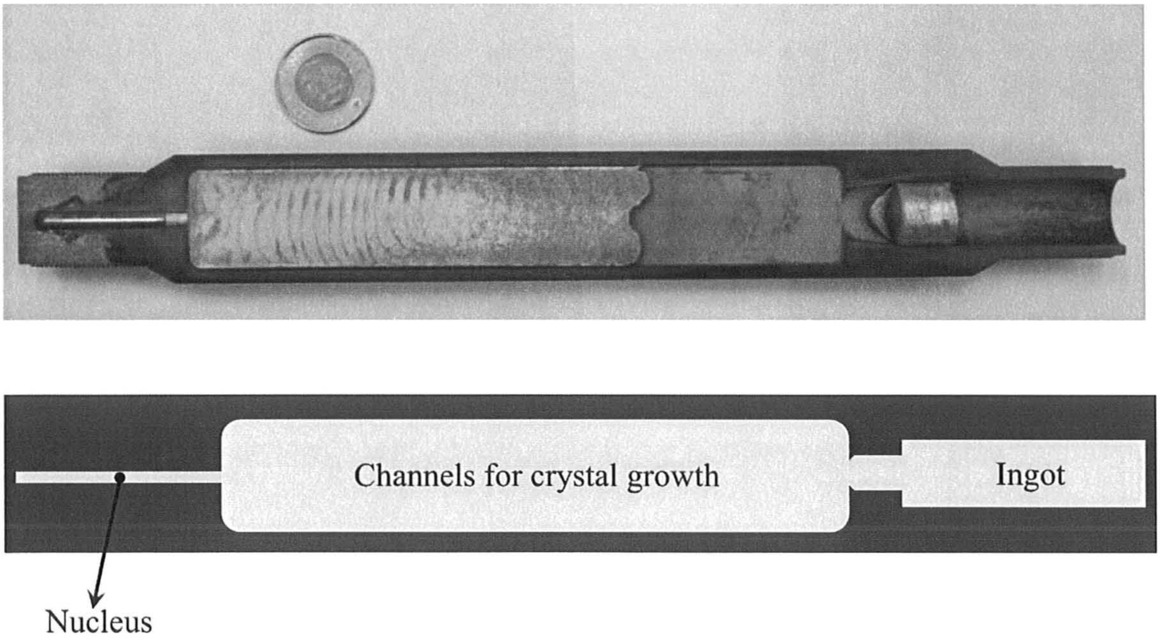

Fig. 3.1 Picture of the grown single crystal and schematic illustration of the graphite mould used for the crystal growth. The coin visible in the picture is 2$ Canadian coin.

Fig. 3.2 shows pictures of crystal growth systems consisted of a vertical furnace with platinum heating coil, rotary and diffusion pumps for vacuum, a thermal controller, an argon gas cylinder, and an alumina tube. The temperature in the furnace was recorded by K type thermocouples and the whole heating and cooling cycles of the furnace was controlled by 2416 programmable temperature and process controller (Eurotherm®).

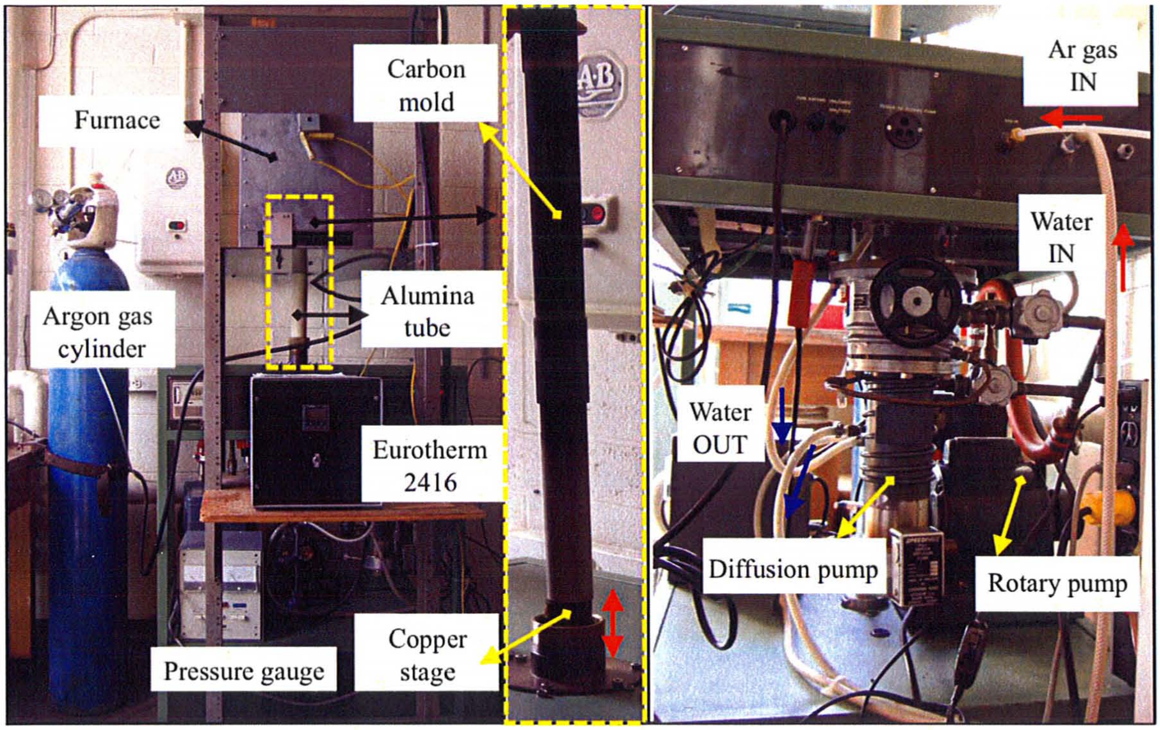

Fig. 3.2 Furnace along with the crystal growth unit used for growing single crystals.

The system is equipped with a copper stage, the height of which can be adjusted vertically with a screw driven device. The carbon mold was mounted on the height adjustable copper stage and was placed inside a high purity alumina tube. The temperature profile of the furnace was recorded by thermocouples placed in between the inside wall of the furnace and the alumina tube. The height of carbon mold was adjusted to ensure that the middle-height of the nucleus was at 933K, the melting point of magnesium. Water-cooling system was used for cooling various elements of the system such as the diffusion pump during heating. The amount of water flowing in the system can be controlled by a valve attached to the water line.

Before heating the furnace, the alumina tube was evacuated to a pressure of 10^{-6} torr using rotary and diffusion pumps. The furnace was switched on and the system was heated to 717K at the rate of 1.5K/min and kept in this temperature for 30min. Then, the diffusion pump was switched off and a high purity argon gas was flown in the chamber till the pressure of the system reached 0.5 – 0.7 atmosphere. The system was heated to 1070K at the rate of 3K/min and homogenized at this temperature for 80min. Following this process, the system was cooled to 773K at the rate of 0.3K/min and then cooled to room temperature naturally. The program for heating and cooling cycles with 2416 programmable temperature and process controller (Eurotherm®) is shown in Table 3.1.

Table 3.1 The program for heating and cooling cycles with 2416 programmable temperature and process controller (Eurotherm®).

Segment	Program	Comments
No. 1	Type rmp.r tGt 444[°C] Rate1.5 [°C/min]	Heating to 717K at the rate of 1.5[K/min].
No. 2	Type dwell dur 30.0[min]	Keep 717[K] during 30min. *Stop diffusion pump and flow in argon gas in the end of this stage.
No. 3	Type rmp.r tGt 797[°C] Rate 3.0 [°C/min]	Heating to 1070K from 717K at the rate of 3.0[K/min].
No. 4	Type dwell dur 80.0[min]	Keep 1070[K] during 80min. **Stop rotary pump in the end of this stage.
No. 5	Type rmp.r tGt 500[°C] Rate 0.3[°C/min]	Cooling to 773K from 1070K at the rate of 0.3[K/min].
No. 6	Type rmp.r tGt 20[°C]	Cooling to room temperature.
No. 7	Type END	END one cycle.

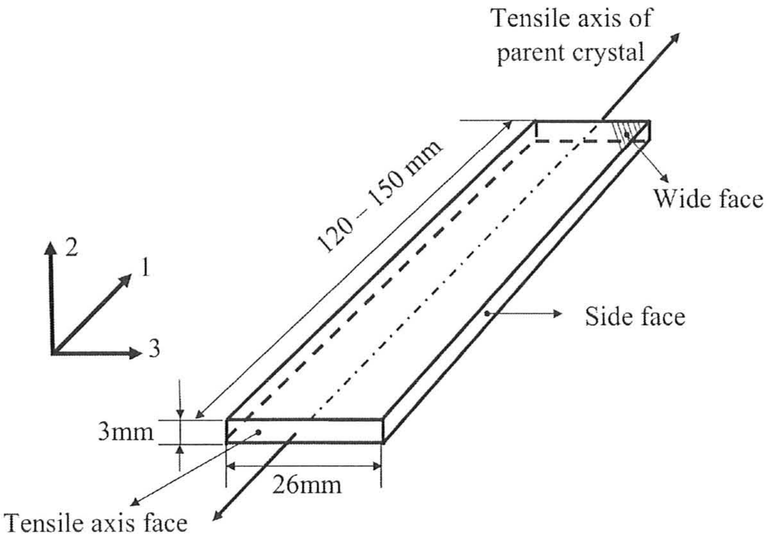

Fig. 3.3 Schematic illustration of a parent crystal with relevant dimensions. 1, 2, and 3 directions show tensile axis face normal, wide face normal, and side face normal, respectively.

One large single crystal of dimensions 3mm x 26mm x 120 – 150mm was produced in one run. Fig. 3.3 shows schematic illustration of large single crystal, hereafter called the parent crystal, where direction 1, 2, and 3 indicate tensile axis face normal, wide face normal, and side face normal, respectively. The orientations of the parent crystals were determined by X-ray back refection Laue technique. X-rays were generated by Philips PW1729 X-ray generator with 40kV voltage at 30mA current. Laue patterns were taken from three parts of wide sides of a parent crystal, 3 cm apart, and then the patterns were matched with each other to evaluate their misorientation. The crystals whose misorientations among three Laue patterns were less than 2^{o} were selected for the experiments. The Laue patterns from parent crystals were indexed using OrientExpress 3.4 (http://laue.web.psi.ch/laue-determination.htm) and stereographic projections indicating the initial orientations of parent crystals were made with OrientExpress 3.4 and WinWulff 1.1.0 (©Jcrystal Soft, http://www.jcrystal.com/). Fig. 3.4 shows the initial orientations of parent crystals on the standard (0001) stereographic projections for hexagonal lattice. Corresponding Schmid factors for principal slip and twinning modes at room temperature, which are: (i) basal <**a**> slip, (ii) 2nd order pyramidal <**c**+**a**> slip, and (iii) $\{10\bar{1}2\}$ twinning, are listed in Table 3.2. The initial orientations of the parent crystals are marked as 1, 2, and 3 on the stereographic projection where marks 1, 2, and 3 indicate the orientation of the tensile axis face, the wide face, and side face, respectively. Parent crystals A and B were oriented for basal slip, whereas parent crystal C was oriented for $\{10\bar{1}2\}$ twinning. The most favorable twinning mode in magnesium single crystal is $\{10\bar{1}2\}$ twinning and it is well known that $\{10\bar{1}2\}$ twinning takes place in tensile deformation along the **c**-axis and perpendicular to the **c**-axis, i.e. the region where Schmid factor for basal <**a**> slip is very small.

The Schmid factors of single crystals have been obtained in the following way. Consider that the tensile axis of the sample is oriented with respect to the crystal, as shown in Fig. 3.5. The angle φ and λ denote the relative orientation of the tensile axis and the normal to the slip plane and the relative orientation of the tensile axis and the slip direction within the slip system, respectively. The resolved shear stress, τ_{rss}, can be expressed by projecting the traction vector $\mathbf{t}^{(\mathbf{n})}$ on the plane with normal **n** on the slip direction:

$$\tau_{rss} = \mathbf{s} \cdot \sigma \mathbf{n} = \sigma_0 \cos\phi \cos\lambda \equiv m\sigma_0 \ldots (3.1)$$

where **s** is a unit vector in the slip direction and σ_0 is the magnitude of the externally applied tensile load. Schmid and Boas (1931) first introduced the equation (3.1) and the factor *m* is usually called Schmid factor. Unlike cubic crystals, the situation is more complicated in the case of hexagonal crystals due to four-index notation. In hexagonal crystals, the direction $[uvtw]$ normal to the plane $(hkil)$ is simply the reciprocal lattice vector $[hkil]^*$ expressed in terms of the direct lattice coordinate system (Otte and Crocker, 1965; Okamoto and Thomas, 1968). Therefore, in the usual notation,

$$[uvtw] = [hki(l\lambda^{-2})] \quad \ldots(3.2).$$

Conversely, the plane $(hkil)$ normal to the direction $[uvtw]$ is given by:

$$(hkil) = (uvt(\lambda^2 w)) \quad \ldots(3.3)$$

, where $\lambda^2 = \frac{2}{3}\left(\frac{c}{a}\right)^2$ …(3.4). The a and c are the length of the basis vectors in hexagonal crystals. In addition, the angle between two vectors, $\mathbf{r}_1 = [u_1 v_1 t_1 w_1]$ and $\mathbf{r}_2 = [u_2 v_2 t_2 w_2]$, is given by:

$$\cos(\mathbf{r}_1, \mathbf{r}_2) = \frac{\mathbf{r}_1}{\|\mathbf{r}_1\|} \cdot \frac{\mathbf{r}_2}{\|\mathbf{r}_2\|} = \frac{u_1 u_2 + v_1 v_2 + t_1 t_2 + \lambda^2 w_1 w_2}{\sqrt{u_1^2 + v_1^2 + t_1^2 + \lambda^2 w_1^2}\sqrt{u_2^2 + v_2^2 + t_2^2 + \lambda^2 w_2^2}} \quad \ldots(3.5).$$

From these equations, the Schmid factor in hexagonal crystals can be calculated. For example, when the tensile axis is parallel to $[11\bar{2}2]$, the Schmid factor for basal system $(0001)[2\bar{1}\bar{1}0]$ is given by:

$$m = \cos\phi\cos\lambda = \frac{1\cdot 0 + 1\cdot 0 + (-2)\cdot 0 + 1.7\cdot 2\cdot 1}{\sqrt{1+1+4+1.7\cdot 4}\sqrt{0+0+0+1.7\cdot 1}} \times \frac{1\cdot 2 + 1\cdot(-1) + (-2)\cdot(-1) + 1.7\cdot 2\cdot 0}{\sqrt{1+1+4+1.7\cdot 4}\sqrt{4+1+1+1.7\cdot 0}}$$

$$= 0.25$$

Similarly, the Schmid factors for other slip systems can be determined using the same calculations.

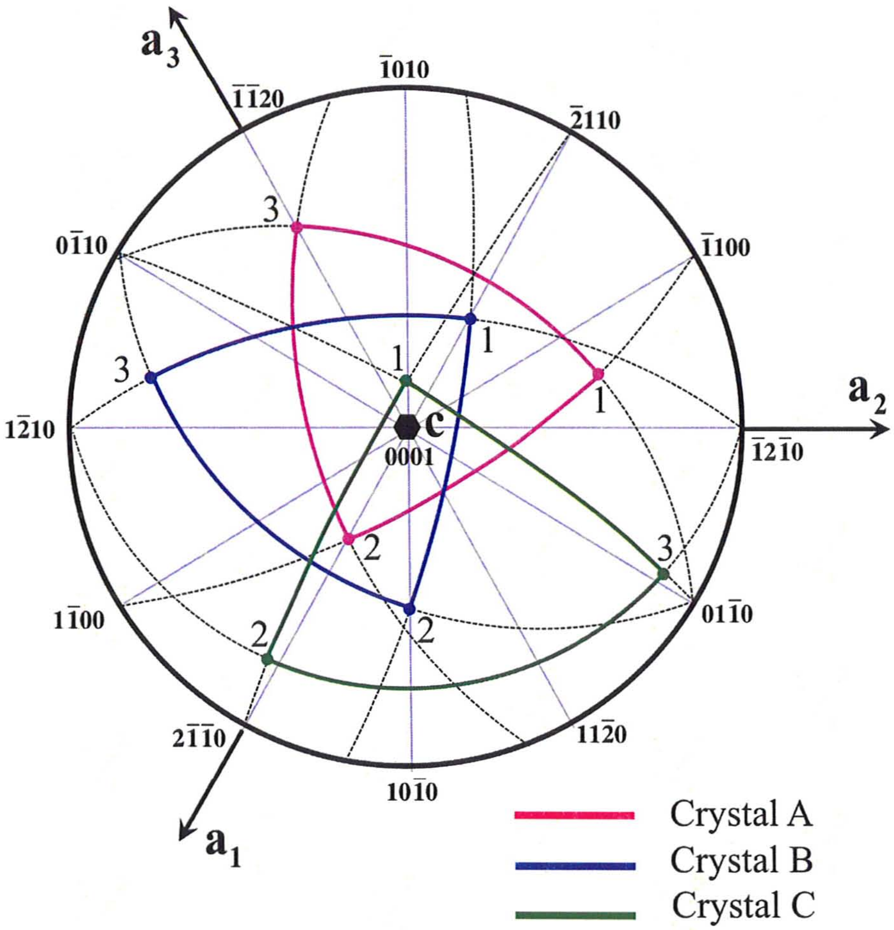

	Mark 1	Mark 2	Mark 3
Crystal A	$(\bar{6}8\bar{2}8)$	$(2\bar{1}\bar{1}4)$	$(\bar{3}\bar{3}64)$
Crystal B	$(2\bar{1}\bar{1}4)$	$(60\bar{6}8)$	$(3\bar{9}64)$
Crystal C	$(\bar{1}018)$	$(6\bar{3}\bar{3}2)$	$(04\bar{4}1)$

Fig. 3.4 The stereographic projection showing initial orientations of tensile axis, wide face, and side face in parent crystal A, B, and C. The orientations of tensile axis, wide face, and side face is indicated by marks 1, 2, and 3, respectively.

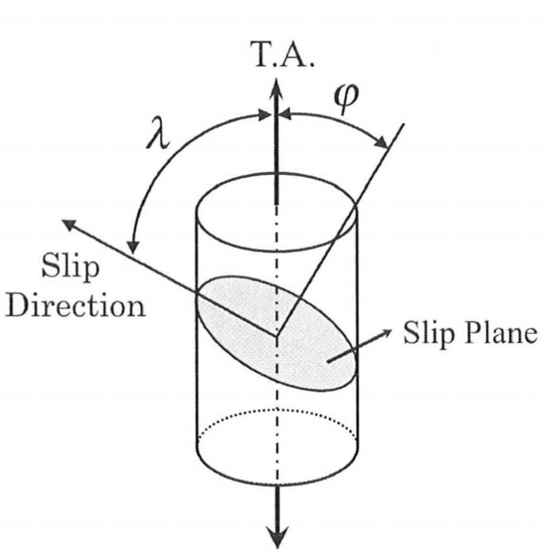

Fig. 3.5 Geometry illustrating angles between tensile axis and slip direction and slip plane normal used to calculate the resolved shear stress in a single crystal (Kelly *et. al.*, 2000).

Table 3.2 Corresponding Schmid factors of slip systems in parent crystals.

Crystals		A	B	C
Basal <**a**> Slip	(0001)[11-20]	0.11	-0.24	-0.19
	(0001)[-2110]	0.32	**0.49**	0.19
	(0001)[1-210]	**-0.42**	-0.24	0
2^{nd} order Pyramidal <**c**+**a**> Slip	(11-22)[-1-123]	0.14	0.11	0.32
	(-1212)[1-213]	0	0.33	0.42
	(-2112)[2-1-13]	0.09	0.31	**0.49**
	(-1-122)[11-23]	0.05	0.33	**0.49**
	(1-212)[-12-13]	-0.38	0.11	0.42
	(2-1-12)[-2113]	-0.20	-0.13	0.32
{10$\bar{1}$2} Twinning	(10-12)[-1011]	0.11	0.18	0.46
	(01-12)[0-111]	-0.07	0.30	**0.47**
	(-1102)[1-101]	-0.25	0.12	0.46
	(-1012)[10-11]	0.09	0.12	0.43
	(0-112)[01-11]	-0.03	0.30	0.46
	(1-102)[-1101]	-0.19	0.18	**0.47**
Remarks		Basal slip	Basal slip	{10$\bar{1}$2} twin

To remove any internal stresses generated during growing and handling, all parent crystals were chemically etched with 10% nitric acid and then annealed in a vacuum of 1.0 x 10^{-3} Pa for 72hrs at 623K. Annealed crystals were cooled very slowly over 12 hrs to room temperature. All the heating and cooling cycles during annealing the crystals were automatically controlled by TEMPSTAR^{TM} (Thermo Electric Instruments). The program with TEMPSTAR^{TM} is shown in Table 3.3.

Table 3.3 The program for heating and cooling cycles with TEMPSTAR^{TM}.

Segment	Programs	Comments
Set point 0	373K	Heating to 373K.
Time 1	3h	Heating to 623K at the rate of 83K/h.
Set point 1	623K	
Time 2	72h	Keep 623K during 12hrs.
Set point 2	623K	
Time 3	12h	Cooling to R.T. at the rate of 27.5 K/h.
Set point 3	293K (Room temperature)	
Time 4	0	END one cycle

Mirror surfaces of single crystals were prepared by electropolishing just before putting it in an Instron machine for deformation experiments. Fig. 3.6 shows the picture of experimental set-up for electrolytic polishing. The conditions given in Table 3.4 for electrolytic polishing were selected empirically after performing several electro-polishing trails with magnesium samples, where voltage, temperature and electrolyte concentration were varied to get the best conditions of electropolishing. Selection of electropolishing voltage was crucial for this metal, use of higher voltage leads to formation of pits on the surface. On the other hand too low voltage would etch the sample. The electrolyte was constantly stirred with a glass rod to avoid formation of bubbles on the surface of the sample, which could lead to the formation of uneven surface or in some cases micro voids. The samples after polishing were quickly cleaned with methanol and dried to avoid formation of oxide layer on the surfaces.

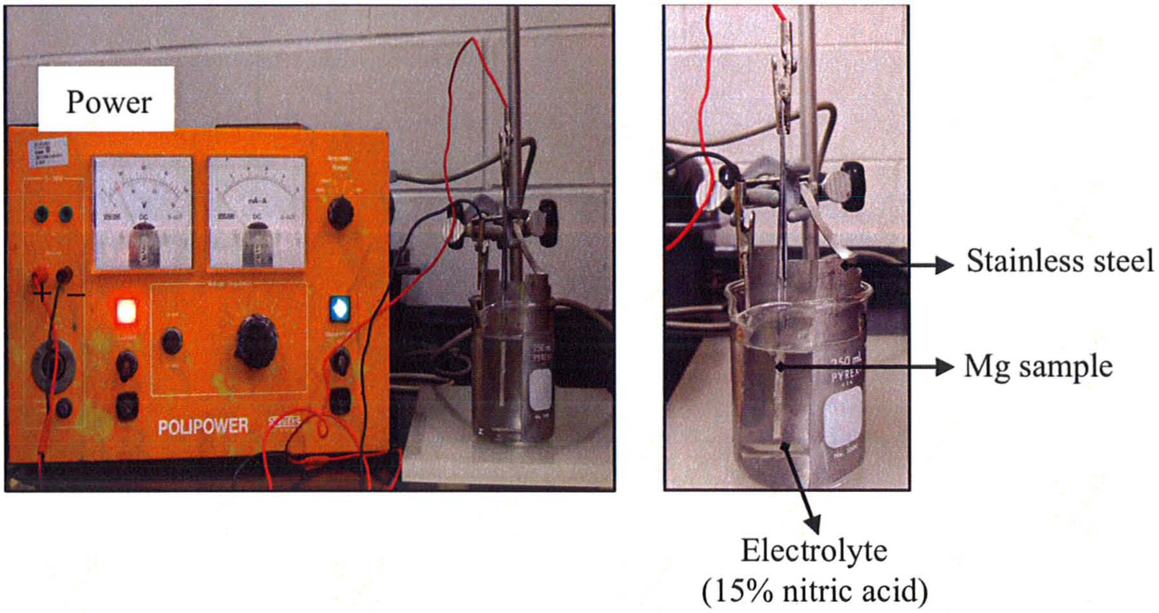

Fig. 3.6 Picture of experimental set up used for electrolytic polishing of the samples.

Table 3.4 Conditions used for electrolytic polishing of magnesium single crystals.

Electrolyte	Temperature	Voltage
Diluted nitric acid (15%) aqueous solutions.	Room temperature (25°C)	10 – 15 V DC

3.2 Tensile test of parent crystals

Parent crystals A, B, and C were deformed in tension at room temperature using Instron tensile test machine. The strain rate was 10^{-4} s^{-1}. In order to describe mechanical properties of parent crystals, four plots (true stress – engineering strain curves, resolved shear stress – resolved shear strain curves, work hardening – true stress plot, and normalized work hardening – true stress plot) were made. Each plot was obtained by the following calculations. True stress σ, engineering stress σ_0, true strain ε, and engineering strain ε_0 are given by:

$$\sigma = \frac{F}{A} \quad \ldots(3.6)$$

$$\sigma_0 = \frac{F}{A_0} \quad \ldots(3.7)$$

$$\varepsilon = \ln\left(\frac{l}{l_0}\right) \ldots(3.8)$$

$$\varepsilon_0 = \frac{\Delta l}{l_0} \ldots(3.9)$$

The resolved shear stress τ and the resolved shear strain α were calculated from the geometrical relation shown in Fig. 3.7 (Kelly *et. al.*, 2000):

$$\tau = \frac{F \cos\phi_0}{A_0}\left[1-\left(\frac{l_0}{l}\right)^2 \sin^2\lambda_0\right]^{1/2} \quad \ldots(3.10)$$

$$\alpha = \frac{\cos\lambda}{\cos\phi} - \frac{\cos\lambda_0}{\cos\phi_0} \quad \ldots(3.11)$$

,where F is the measured load, A_0 is the initial cross-sectional area of the specimen, A is the instantaneous cross-sectional area of the specimen, l_0 is the initial specimen length, l is the instantaneous specimen length, ϕ_0 is the initial angle between the tensile axis and the sip plane normal, and λ_0 is the initial angle between the tensile axis and the slip direction. Work hardening θ is given by:

$$\theta = \frac{d\sigma}{d\varepsilon} \ldots(3.12)$$

where σ is the true stress and ε is the true strain represented by Equations (3.6) and (3.8), respectively.

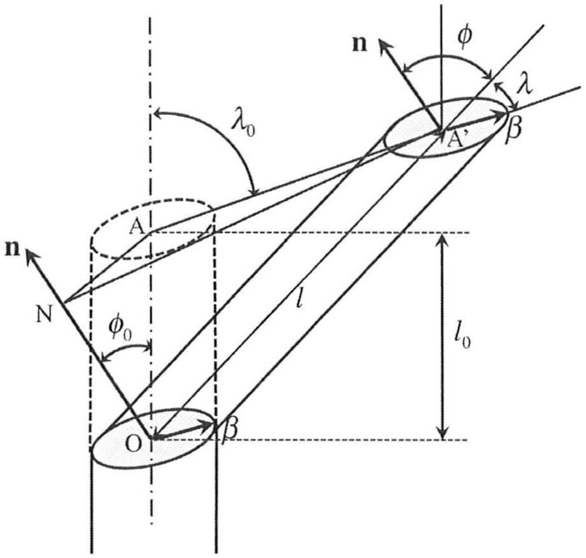

Fig. 3.7 Schematic illustration of extension of a single crystal under conditions of a single slip (Kelly *et. al.*, 2000).

3.3 Preparation of secondary samples

Small samples called secondary samples were cut out from deformed parent crystals in various directions with respect to the tensile axis of the parent crystals. In this paper, a clockwise direction with respect to tensile axis of parent crystal is +θ, while an anti-clockwise direction is - θ, as shown in Fig. 3.8.

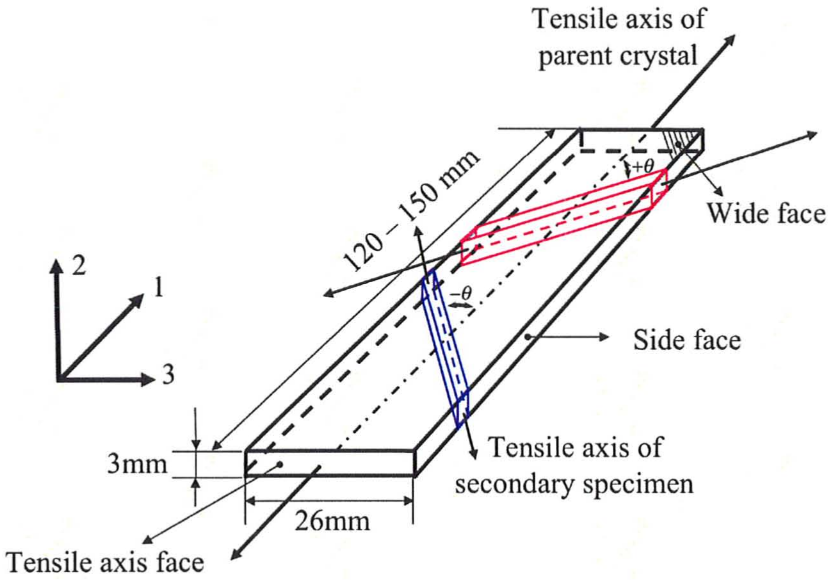

Fig. 3.8 Schematic illustration of a parent crystal and secondary samples cut from the parent crystal. 1, 2, and 3 coordinate directions show tensile axis, wide face normal, and side face normal, respectively.

The orientations of secondary samples were chosen to excite different secondary slip systems based on the variations of Schmid factors for these systems. Fig. 3.9 shows Schmid factor variations for basal slip as a function of the cutting angle in crystal A. Similarly, the orientations of secondary samples were selected in crystals B and C. The traces of the wide sides of parent crystals labeled A – A, B – B, and C – C were shown and the orientations of tensile axis face of secondary samples were marked as full circles on the stereographic projection in Fig. 3.10. Their corresponding Schmid factors of secondary samples and the angle between parent crystals and secondary samples are listed in Table 3.5.

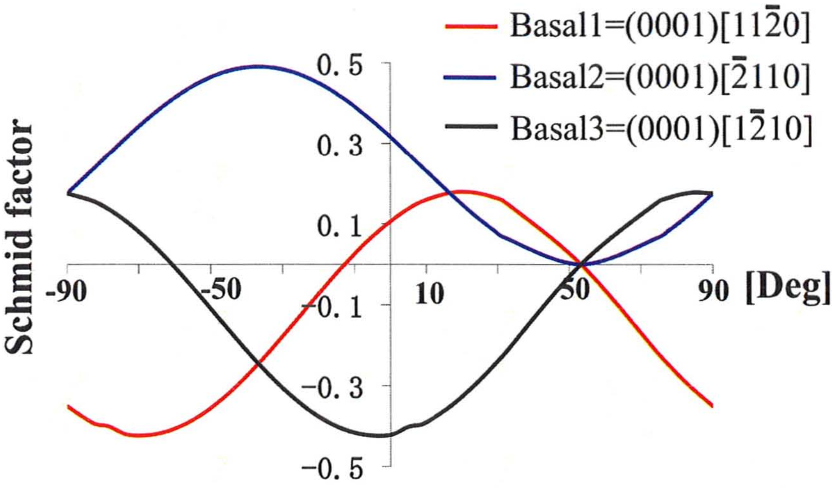

Fig. 3.9 Variations of the Schmid factors for three basal <**a**> slip systems in the parent crystal A.

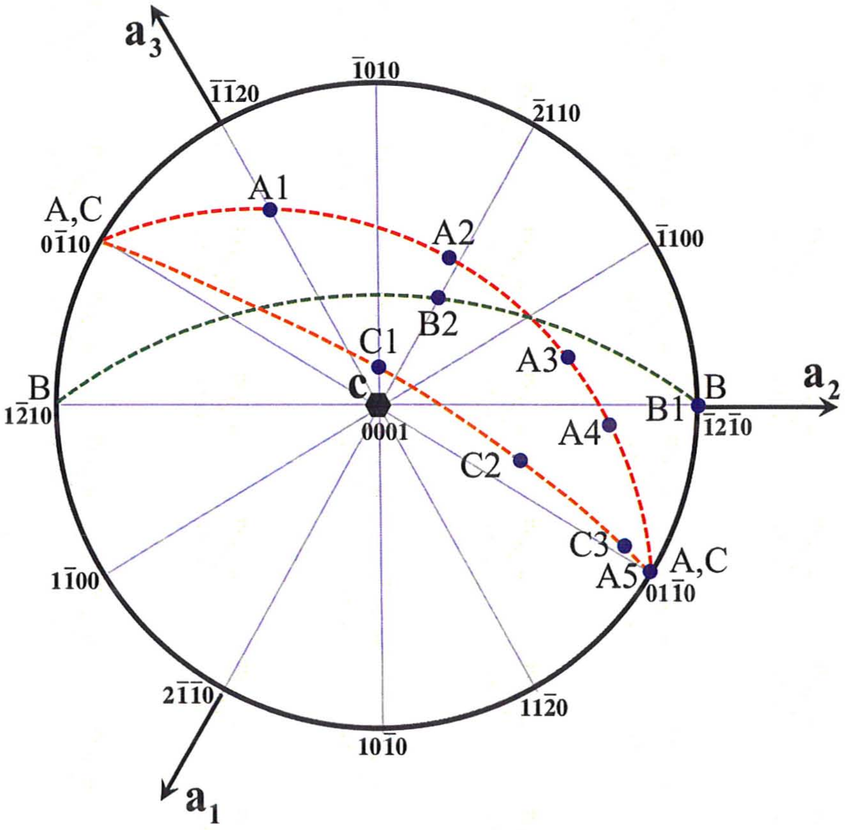

Fig. 3.10 Stereographic projection showing the traces of the wide faces of the parent crystals (dashed curves) and the orientations of the secondary samples marked as A1 – A5, B1 – B2 and C1 – C3, respectively.

Table 3.5 Schmid factors of slip systems in all the secondary samples.

Parent crystal			A				
Secondary specimens			A1	A2	A3	A4	A5
Angles between the primary system and Latent systems			-90°	-40°	0°	+20°	+55°
Schmid factors	Basal <**a**> Slip	(0001) [11-20]	**-0.35**	-0.29	0.11	0.18	0
		(0001) [-2110]	0.18	**0.48**	0.32	0.13	0
		(0001) [1-210]	0.17	-0.21	**-0.42**	**-0.31**	0
	2nd order pyramidal <**c+a**> Slip	(11-22) [-1-123]	-0.48	-0.04	0.14	0	**-0.33**
		(-1212) [1-213]	-0.11	0.22	0	-0.21	**-0.33**
		(-2112) [2-1-13]	0.05	0.13	0.09	0.04	0
		(-1-122) [11-23]	-0.16	0.21	0.05	-0.16	**-0.33**
		(1-212) [-12-13]	0.05	0.04	-0.38	-0.49	**-0.33**
		(2-1-12) [-2113]	-0.11	-0.30	-0.20	-0.08	0
	$\{10\bar{1}2\}$ Twinning	(10-12) [-1011]	-0.23	-0.02	0.11	0.05	-0.12
		(01-12) [0-111]	-0.23	0.19	-0.07	-0.33	**-0.50**
		(-1102) [1-101]	0.07	0	-0.25	-0.26	-0.12
		(-1012) [10-11]	-0.27	-0.07	0.09	0.05	-0.12
		(0-112) [01-11]	-0.27	0.18	-0.03	-0.29	**-0.50**
		(1-102) [-1101]	0.07	0.03	-0.19	-0.23	-0.12
Remarks			Basal slip	Basal slip	Basal slip	Basal slip	2nd py. slip

Parent crystal			B		C		
Secondary specimens			B1	B2	C1	C2	C3
Angles between the primary system and Latent systems			0°	+70°	0°	+40°	+90°
Schmid factors	Basal <**a**> Slip	(0001) [11-20]	-0.24	0	-0.19	**-0.48**	0.10
		(0001) [-2110]	**0.49**	0	0.19	0.09	0
		(0001) [1-210]	-0.24	0	0	0.38	-0.10
	2nd order Pyramidal <**c**+**a**> Slip	(11-22) [-1-123]	0.11	-0.11	0.32	-0.22	-0.28
		(-1212) [1-213]	0.33	**-0.45**	0.42	-0.10	-0.28
		(-2112) [2-1-13]	0.31	-0.11	**0.49**	0.24	0.01
		(-1-122) [11-23]	0.33	-0.11	**0.49**	0.21	**-0.37**
		(1-212) [-12-13]	0.11	**-0.45**	0.42	0.24	**-0.37**
		(2-1-12) [-2113]	-0.13	-0.11	0.32	0.16	0.01
	$\{10\bar{1}2\}$ Twinning	(10-12) [-1011]	0.18	0	0.46	0.14	-0.12
		(01-12) [0-111]	0.30	-0.37	**0.47**	0.01	**-0.49**
		(-1102) [1-101]	0.12	-0.37	0.46	0.21	-0.12
		(-1012) [10-11]	0.12	0	0.43	0.10	-0.11
		(0-112) [01-11]	0.30	-0.37	0.46	-0.06	-0.48
		(1-102) [-1101]	0.18	-0.37	**0.47**	0.19	-0.11
Remarks			Basal slip	2nd py. slip	$\{10\bar{1}2\}$ twin	Basal slip	2nd py. slip

Secondary samples were spark-cut very carefully with the cutting speed ~ 1mm/h, by electron spark cutting machine, using 30 μm in diameter molybdenum wire. The surface layer exposed to the spark operation was removed by mechanical and chemical polishing (85% orthophosphoric acid). Finally, secondary specimens were submitted to electropolishing just before secondary tests. (See Fig. 3.6 and Table 3.5 in details.)

3.4 Tensile test for secondary samples

All the secondary samples were deformed in tension at room temperature using Instron tensile test machine. Fig. 3.11 shows photographs of tensile test set-up for secondary samples. Special jigs to hold secondary samples were used in tensile tests, as shown in Fig. 3.11. The strain rate during secondary deformation was the same as during primary tensile tests i.e. 10^{-4} s^{-1}. The average dimensions of secondary tensile samples were 2.5mm x 2.8 mm x 23 mm.

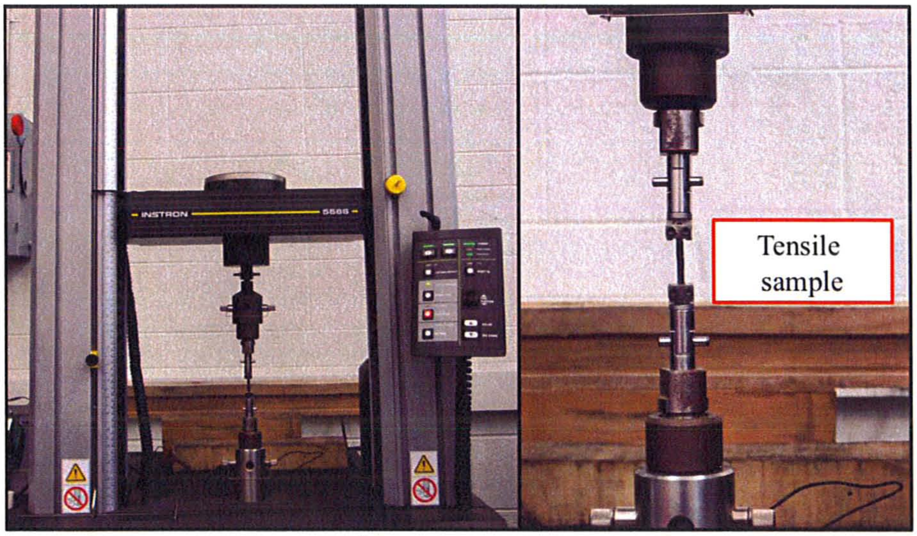

Fig. 3.11 Experimental set-up for secondary tensile test.

3.5 Surface observation

The slip bands and twinning surface patterns formed on the surfaces of parent crystals and secondary samples were observed with an optical microscopy (Nikon). The slip bands and fracture surfaces of some secondary samples were observed with scanning electron microscopy (Philips SEM515).

3.6 SEM/EBSD analysis

The application of scanning electron microscope/electron backscattering diffraction (SEM/EBSD) technique has been increasing rapidly in metallurgical and materials science fields since the middle of 1990's (Engler and Randle, 2009; Schwartz *et. al.*, 2009). A SEM/EBSD technique enables to automatically determine individual crystal orientations, local texture, phase identification and distributions and point-to-point orientation relations on the surface of crystals. SEM/EBSD technique has been used in the present studies to analyze deformation process of single crystals. A SEM/EBSD system used in this work consists of the SEM, charge coupled device (CCD) camera (or silicon intensified target (SIT)), and the software. Fig. 3.12 shows schematic drawing of the typical EBSD set up, indicating the pole piece of the SEM, the electrons beam, the tilted specimen, and CCD camera.

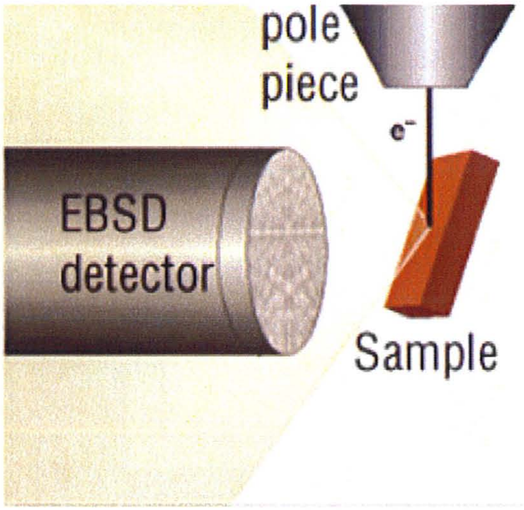

Fig. 3.12 Schematic illustration of the typical EBSD geometry: the pole piece of the SEM, the electron beam, the tilted sample, and the phosphor screen (Schwartz *et. al.*, 2009).

Pole figures were used to represent crystallographic orientations of the crystals. Pole figures show the position of a pole relative to the sample reference frame defined as rolling direction (RD), transverse direction (TD), and normal direction (ND). This notation is used to orient single crystal samples, as shown in Fig. 3.13. In this study, tensile axis of the samples corresponds to rolling direction. For example, Fig. 3.14 (a) shows the situation where the **c**-axis and the $\mathbf{a}_1$-axis in hexagonal lattice are parallel to rolling direction and transverse direction, respectively. Corresponding 0001 and $2\bar{1}\bar{1}0$ pole figures are shown in Fig. 3.14 (b).

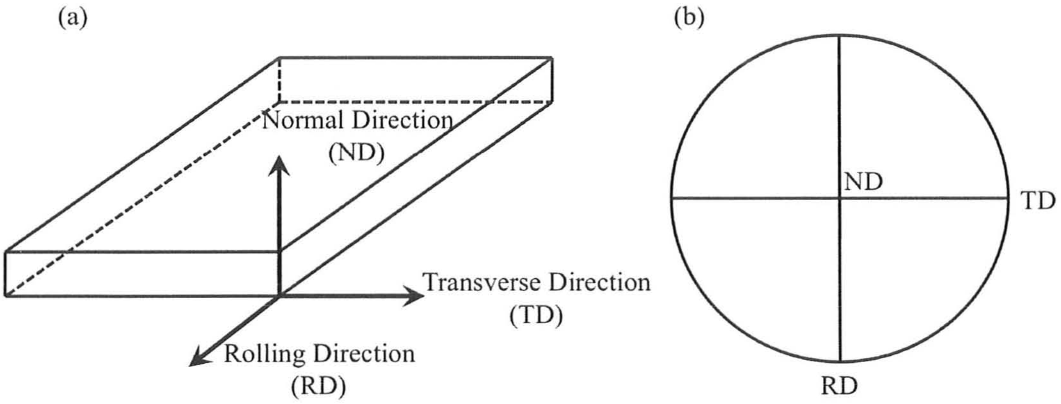

Fig. 3.13 Schematic illustration of a standard pole figure with respect to the orientation of a single crystal sample. RD, TD, and ND correspond to rolling direction, transverse direction, and normal direction, respectively.

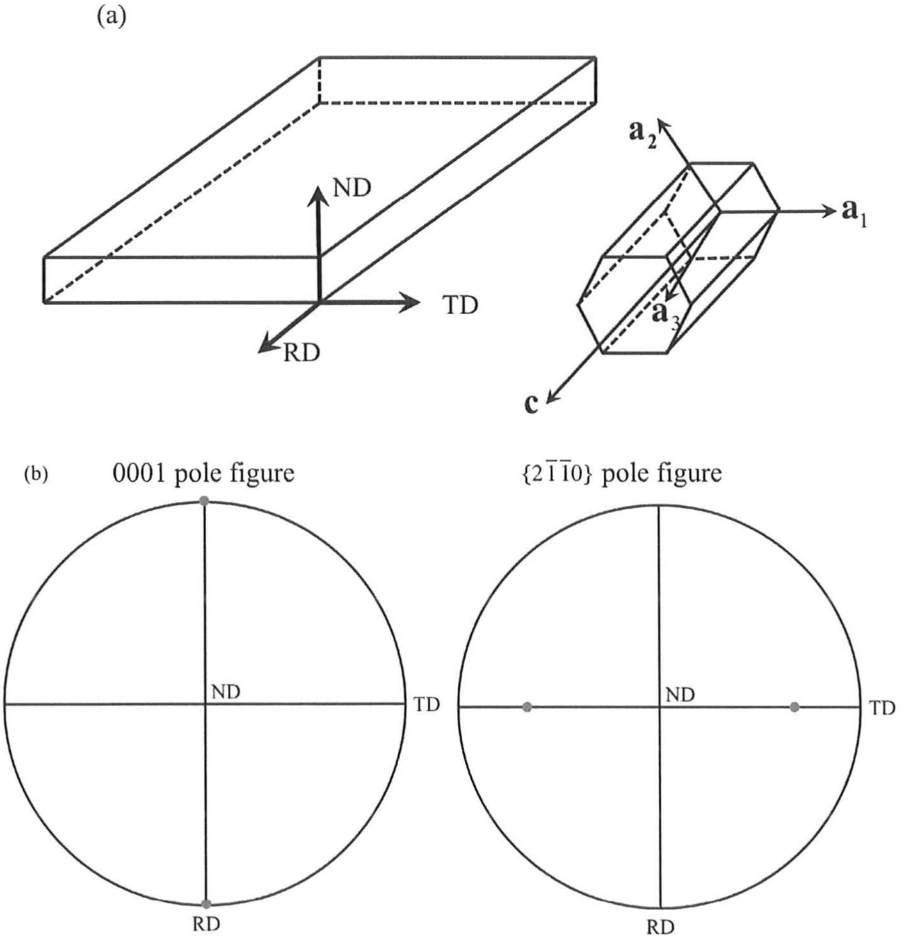

Fig. 3.14 Schematic illustration of pole figures on 0001 and $2\bar{1}\bar{1}0$. RD, TD, and ND correspond to rolling direction, transverse direction, and normal direction, respectively.

An inverse pole figure is another method to describe orientations of the single crystals and the method was also used in the present work. An inverse pole figures shows the position of a sample direction relative to the crystal reference frame. Consider the same situation as Fig. 3.14 (a) again. The full inverse pole figure is shown in Fig. 3.15 (a). The unit triangle is usually used to present one unique orientation in texture analysis. The unit triangle in hexagonal crystals is made from the triangle surrounded by 0001, $2\bar{1}\bar{1}0$, and $10\bar{1}0$ poles. As a result of such convention, the orientations of RD, TD, and ND on the inverse pole figures are shown in Fig. 3.15 (b).

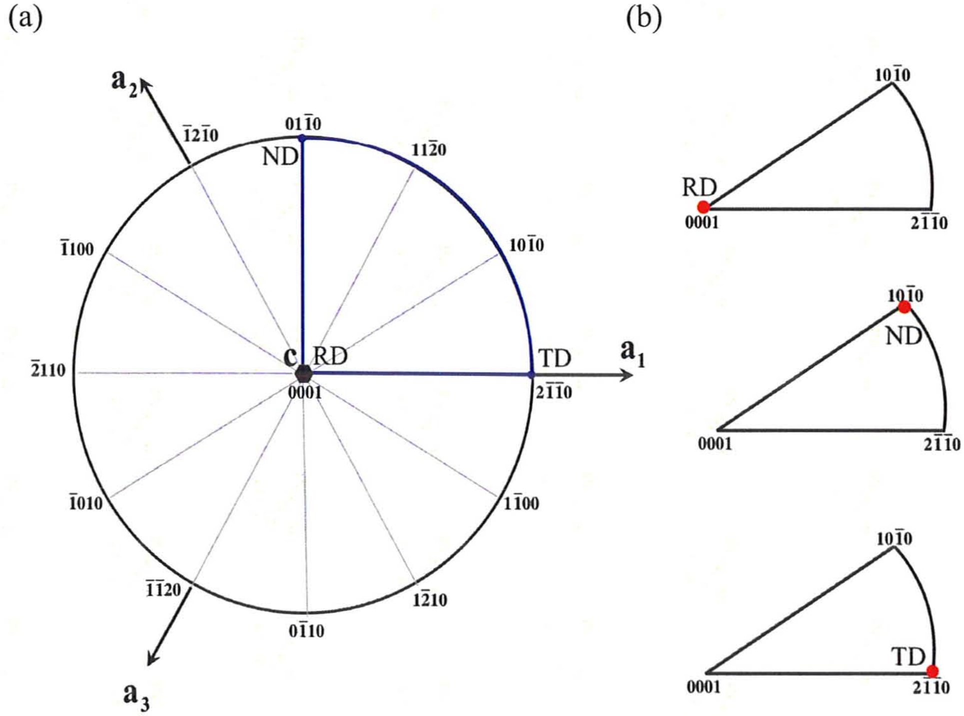

Fig. 3.15 Schematic illustration of inverse pole figure. RD, TD, and ND correspond to rolling direction, transverse direction, and normal direction, respectively.

In the present work, the orientation images were obtained with a scanning electron microscopy (SEM) (LEO (now, Carl ZEISS) 1455) and a scanning electron microscopy with a field emission electron gun (FE-SEM) (Carl ZEISS NVision40 Crossbeam Workstation) with OIM Data Collection (EDAX-TSL). Observation surface of the crystals was chemically polished with a solution of ethanol 60 mL, acetic acid 15 mL, nitric acid 5 mL, and distilled water 20 mL. Samples were polished in the solution for 15 seconds, then quickly cleaned in pure ethanol and dried with an air blower. The orientation maps of all the samples were recorded in an area of approximately 1x1 mm^2 with a beam step of 3 μm. In the specific samples (C1T, C2T, and C3T), high-resolution EBSD maps were recorded with a beam step of 0.10 or 0.50 μm. OIM analysis software 5.3 (EDAX-TSL) was used to analyze EBSD results.

The main purpose of using SEM/EBSD technique is to identify crystallographic nature of twins formed in deformed magnesium single crystals and to measure the orientation of the crystals after deformation. As discussed in Chapter 2, there exist crystallographic relationship between matrix and twin. $\{10\bar{1}2\}$ twin, $\{10\bar{1}1\}$ twin and $\{10\bar{1}1\}-\{10\bar{1}2\}$ double twin are well reported in magnesium and magnesium alloys. $\{10\bar{1}2\}$ twin is associated with the rotation of **c**-axis by 86° around $<11\bar{2}0>$ axis (**a**-axis), as shown in Fig. 3.16. $\{10\bar{1}1\}$ twin accompany the rotation of **c**-axis by 56° around $<11\bar{2}0>$ axis (or **a**-axis). The $\{10\bar{1}1\}-\{10\bar{1}2\}$ double twin is associated with the rotation of **c**-axis by 38° about $<11\bar{2}0>$ axis (**a**-axis) (See Table 3.6).

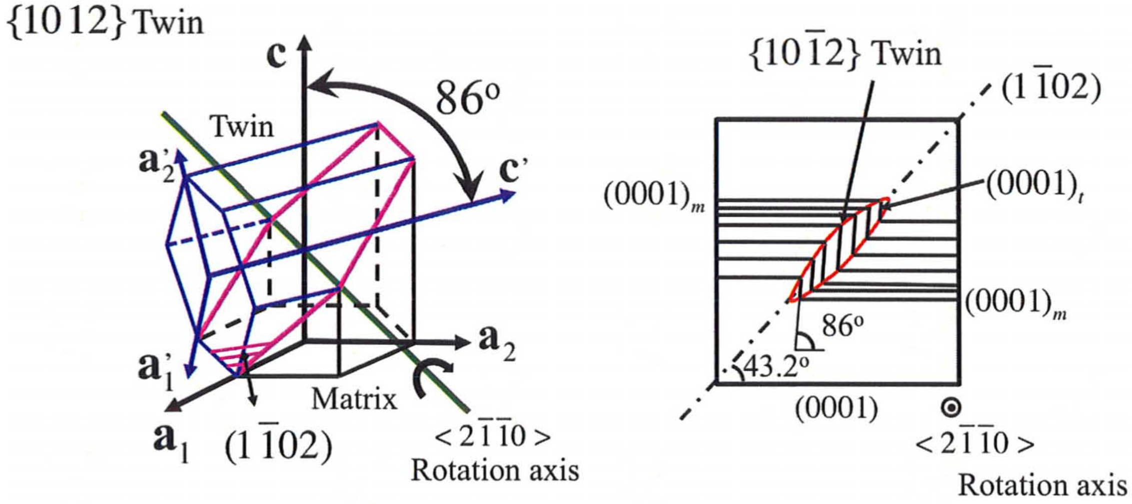

Fig. 3.16 Geometrical relationship between the matrix lattice and the twin lattice in $\{10\bar{1}2\}$ twin.

Table 3.6 Geometrical factors of twinning in magnesium (Chou *et. al.*, 2005).

Twinning type	Rotation (Common) Axis	Misorientation
$\{10\bar{1}2\}$	$<11\bar{2}0>$	86°
$\{10\bar{1}1\}$	$<11\bar{2}0>$	56°
$\{10\bar{1}2\}-\{10\bar{1}1\}$	$<11\bar{2}0>$	38°

Chapter 4 Experimental Results

4.1 Primary deformation tests

Parent crystals A and B are oriented for basal slip and parent crystal C is oriented for tension twinning, as shown in Table 3.2. Fig. 4.1 (a) and (b) show macroscopic photographs of parent crystals B and C after deformation at room temperature, respectively. Parent crystal A and B were deformed by basal single slip as shown in Fig. 4.2 (a). In parent crystal C, on the other hand, deformation with bending and twisting started in the middle part of the sample and then relatively wide deformation bands were developed. $\{11\bar{2}0\}$ type kinking accompanied with many $\{10\bar{1}2\}$ twins and slip bands corresponding to basal plane as shown in Fig. 4.2 (b) were observed. Fig. 4.3 shows true stress – engineering strain curves and work hardening – true stress plot of parent crystals at room temperature. Table 4.1 shows the value of the yield stress and final work hardening for parent crystals.

In parent crystals A and B, easy glide started after elastic deformation and yielding. The yield stress of parent crystal B, which has higher Schmid factor for basal <**a**> slip, was lower than that of parent crystal A. The work hardening of parent crystal A was higher than that of parent crystal B. In parent crystal A, the Schmid factor for basal <**a**> slip was 0.42 and some inhomogeneous deformation was observed based on the slip line patterns formed on the lateral surface of the crystal. Small amounts of $\{10\bar{1}2\}$ twins were formed in the middle part of the parent crystal A.

In the parent crystal C, the activation of basal slip was difficult during the initial stage of deformation because the Schmid factor for basal slip is very small ~ 0.18. In this case, it was observed that deformation proceeded by kink bands formation and $\{10\bar{1}2\}$ twin propagation in the initial stage of deformation (Fig. 4.2(b)). The work hardening rate showed sudden increase after about 3% strain (Fig. 4.3(b)). Crystallographic orientation of the sample was changed as a result of deformation with twisting and bending, resulting in the increasing in the Schmid factor for basal slip. In the region after 3% strain, deformation proceeded by basal slip and twin propagation. From slip trace analysis, the angle between basal plane normal and tensile axis was about 20° – 30°.

The tensile deformation of the parent crystals was stopped at the easy glide stage i.e., at about 5% strain in crystal A, about 15% strain in crystal B, and about 10% strain in crystal C, to examine latent hardening behavior in magnesium single crystals.

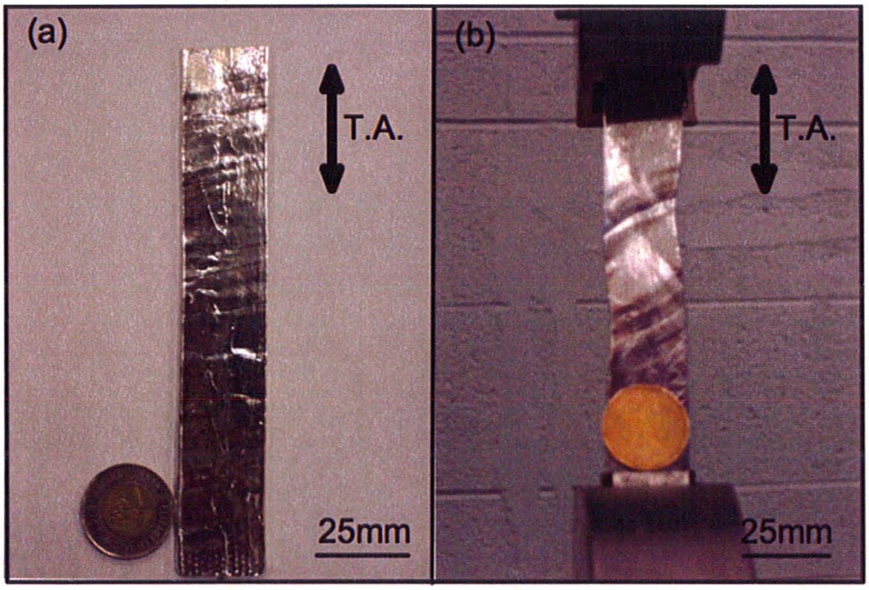

Fig. 4.1 Photographs of parent crystals (a) B oriented for basal slip and (b) C oriented for tension twinning after deformation (strain 15% in crystal B and strain 10% in crystal C) at room temperature.

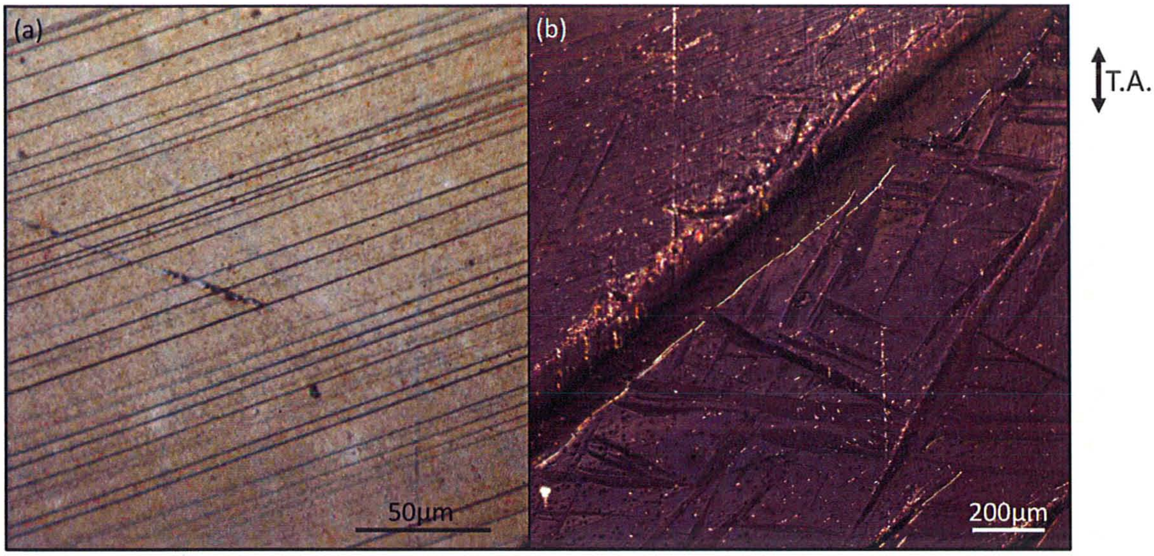

Fig. 4.2 Optical microscopy images of (a) slip bands in parent crystal B and (b) activated twins in parent crystal C.

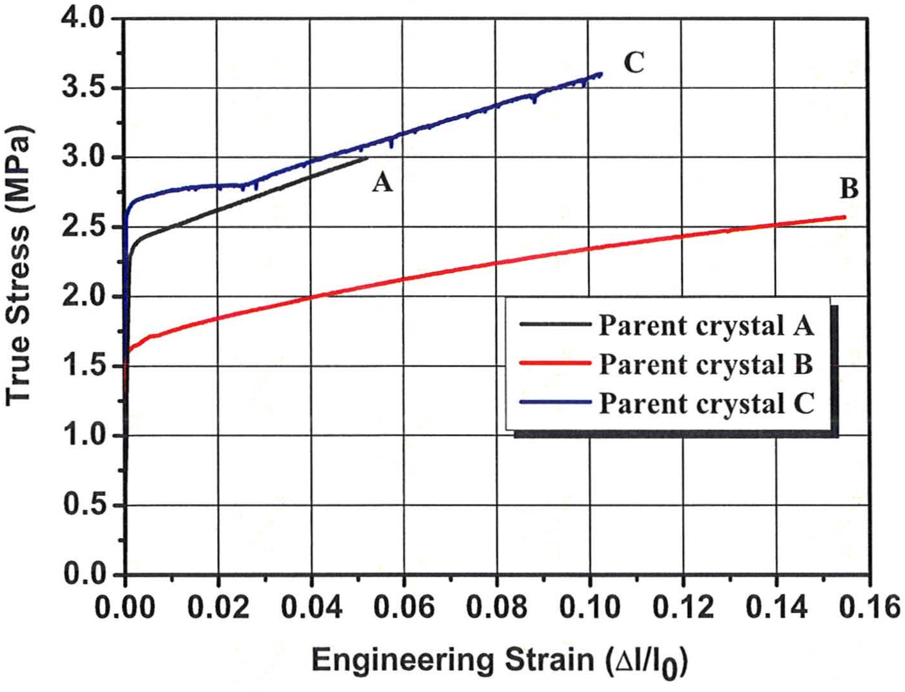

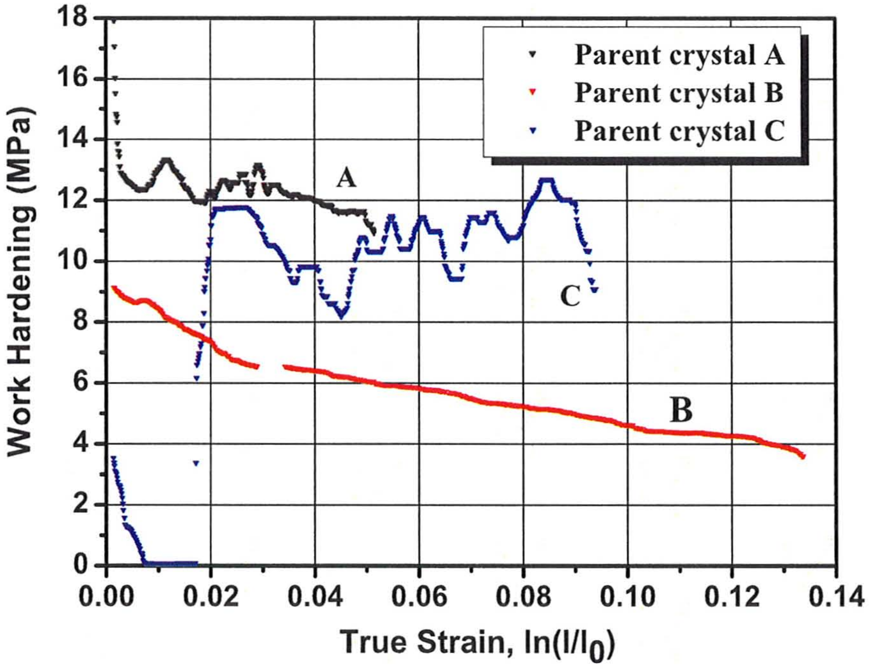

Fig. 4.3 True stress – engineering strain characteristics and work hardening – true stress plot of parent crystals A, B, and C at room temperature.

Table 4.1 Tensile test data for parent crystals.

Parent crystal	Yield stress [MPa]	Final work hardening [MPa]
A	1.72	10.5
B	2.38	5.5
C	2.73	8.6 (jerky)

4.2 Secondary tensile tests in crystals A and B

We first review the orientations of secondary samples cut from deformed parent crystals. Fig. 4.4 shows a stereographic projection indicating the trace of the wide face of parent crystals and the initial orientations of tensile axes of secondary samples. The tensile axes of secondary samples are marked on a great circle representing the trace of wide face of parent crystals as orientations A1 – A5 and B1 – B2. The information about secondary samples is summarized in Table 4.2, containing the angle between the tensile axis of primary and secondary sample, Schmid factor for basal <**a**> slip, and the type of dislocation interactions in the primary and secondary test. In table 4.2, Basal 1, Basal 2, and Basal 3 indicate three different basal slip systems, respectively. From the calculation of the Schmid factor for basal <**a**> slip, secondary samples A1, A2, A3, A4 and B2 were oriented for basal <**a**> slip, while secondary samples A5 and B1 were oriented for 2nd order pyramidal <**c**+**a**> slip.

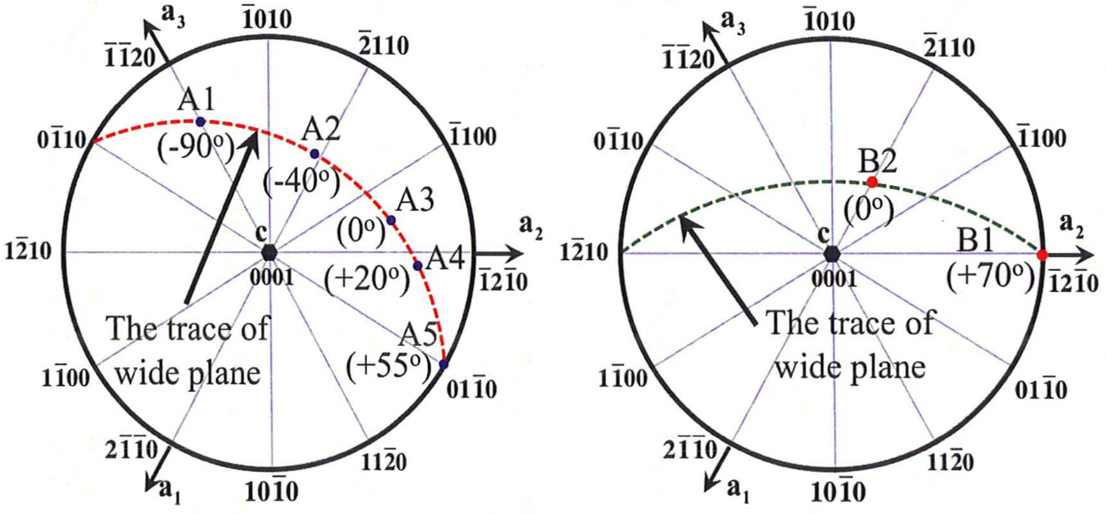

Fig. 4.4 Stereographic projection showing trace of the wide planes of parent crystals A and B (dashed lines) and the orientations of tensile axes of secondary samples (Orientations A1 – A5 and B1 – B2).

Table 4.2 Schmid factors for basal slip systems in secondary samples and types of dislocation interactions expected to occur between primary and secondary dislocations.

Parent crystals	A				B
Secondary specimens	A1	A2	A3	A4	B2
Cutting angle	± 90°	-40°	0°	+20°	0°
Basal 1=(0001)[11-20]	**-0.35**	-0.29	0.11	0.18	-0.24
Basal 2=(0001)[-2110]	0.18	**0.48**	0.32	0.13	**0.49**
Basal 3=(0001)[1-210]	0.17	-0.21	**-0.42**	**-0.31**	-0.24
Interaction type Primary/secondary	B.3/B.1	B.3/B.2	B.3/B.3	B.3/B.3	B.2/B.2

Parent crystals	A	B
Secondary samples	A5	B1
Cutting angle	+55°	+70°
Basal 1=(0001)[11-20]	0	0
Basal 2=(0001)[-2110]	0	0
Basal 3=(0001)[1-210]	0	0
Interaction type Primary / Secondary	B.3/ 2nd Py.	B.2 / 2nd Py.

4.2.1 Tensile tests for basal orientation

Fig. 4.5 shows true stress – engineering strain curves and work hardening – true stress plot of secondary tensile samples (A1T, A2T, A3T, A4T, and B2T) at room temperature. Table 4.3 shows the value of the yield stress and final work hardening for secondary samples. There was no difference in the yield stress among the secondary samples. The mechanical characteristics of secondary samples were divided into two groups according to work hardening behavior. One group was A1T, A3T, and A4T samples where the slip system was Basal 3. Another group was A2T and B2T samples where the slip system was Basal 2.

Table 4.3 Tensile test data for secondary samples oriented for basal slip.

Parent crystal	Secondary sample	Yield stress [MPa]	Final work hardening [MPa]
A	A1T (-90°)	2.28	13.4
	A2T (-40°)	2.06	3.6
	A3T (0°)	2.12	13.9
	A4T (+20°)	2.13	11.5
B	B2T (0°)	2.30	4.1

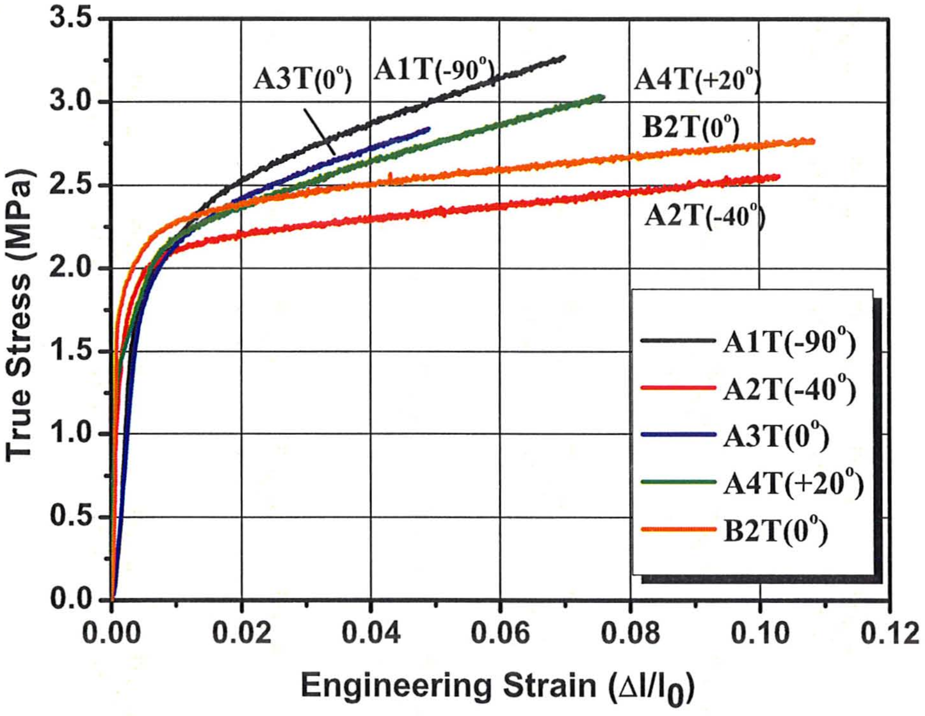

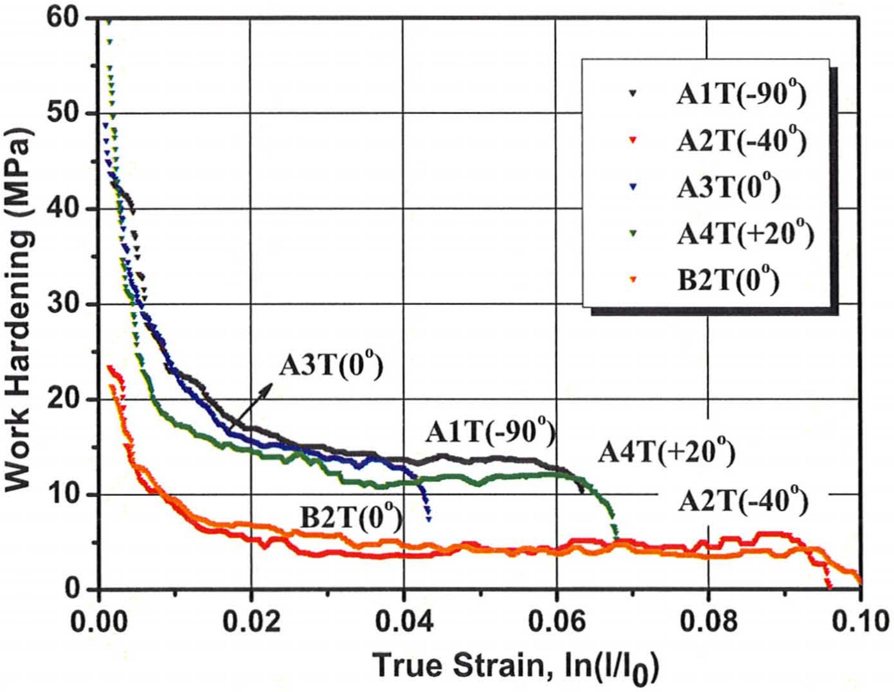

Fig. 4.5 True stress – engineering strain characteristics and work hardening – true stress plot of the A and B type secondary specimens oriented for basal <**a**> slip. (Secondary samples A1T, A2T, A3T, A4T and B2T).

4.2.2 Tensile tests for 2nd order pyramidal <**c**+**a**> orientation

Fig. 4.6 shows true stress – engineering strain curves and work hardening – true stress plot of secondary tensile samples A5T and B1T at room temperature. The mechanical behavior of secondary samples A5T and B1T were completely different from that of basal orientation. The mechanical properties of A5T and B1T were characterized by very rapid work hardening and much higher yield stress than that observed in basal orientation. The highest true stress in A5T and B1T were as large as 120 MPa and 167 MPa, respectively. The fracture occurred in the early stage of deformation in both secondary samples. Optical microscopy observation on the surface of secondary samples A5T and

B1T showed that there was no clear slip traces corresponding to 2nd order pyramidal <**c**+**a**> slip. However, Yoshinaga and Horiuchi (1962) reported similar pyramidal fracture mechanism for magnesium single crystals whose initial orientation was 2nd order pyramidal <**c**+**a**> slip. Recently, Bhattacharya (2006) studied dislocation distributions of magnesium single crystals oriented along the $<11\bar{2}0>$ direction with zero Schmid factor for basal <**a**> slip after large deformation by transmission electron microscopy and observed the short-range activation of 2nd order pyramidal <**c**+**a**> slip in the sample. Based on these findings, it was concluded that when tensile force was applied parallel to the **a**-axis of a hexagonal lattice, pyramidal fracture takes place at the early stage of deformation.

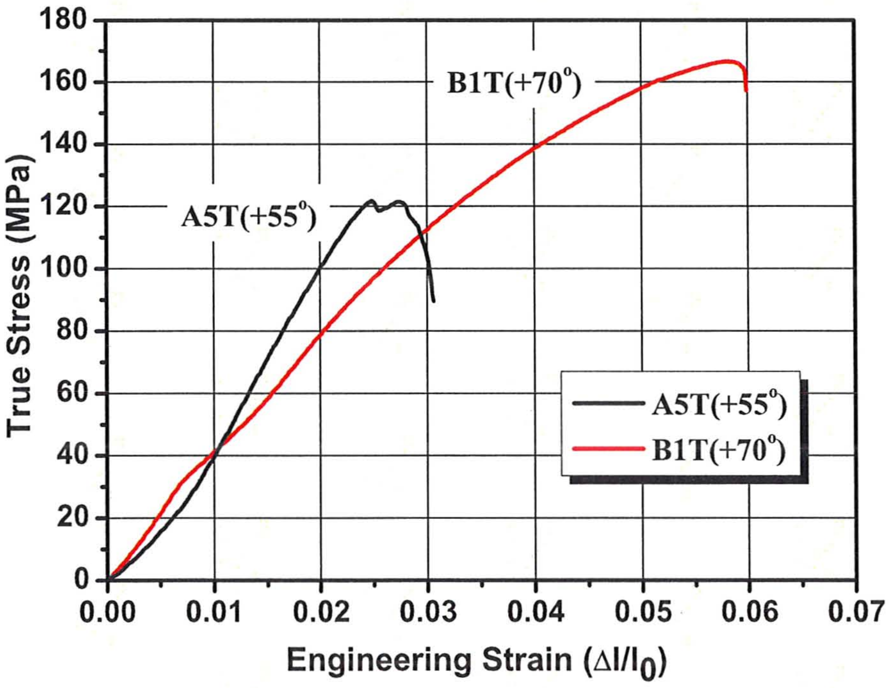

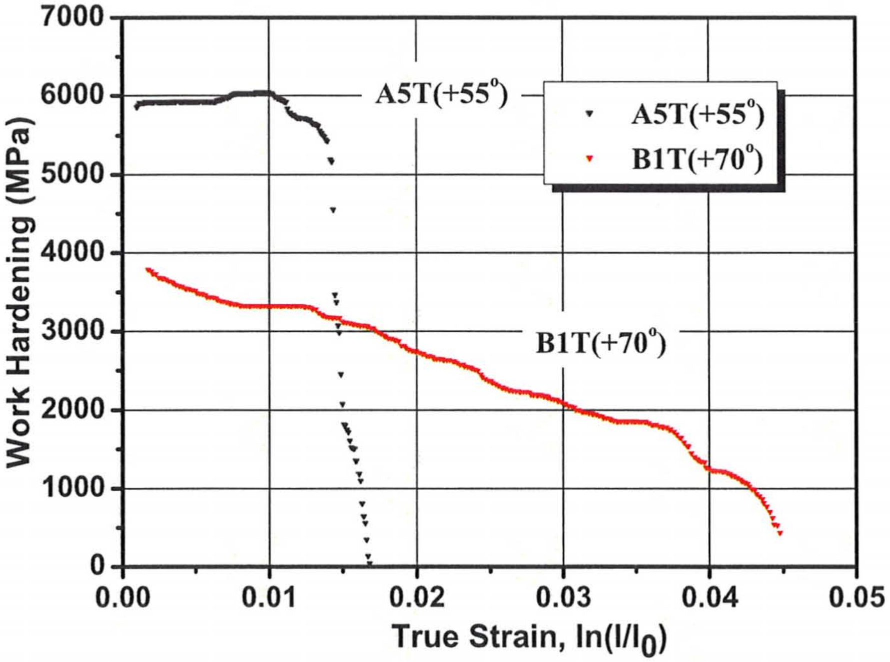

Fig. 4.6 True stress – engineering strain characteristics and work hardening – true stress plot of the A and B type secondary specimens oriented for 2nd order pyramidal <**c**+**a**> slip. (Secondary samples A5T and B1T).

4.3 Latent hardening behavior in crystals A and B

When analyzing latent hardening tests, two important factors have to be considered namely: size effect and recovery effect at room temperature. As mentioned in Chapter 3, parent crystals had dimensions of 3mm x 26mm x 120 – 150mm, while secondary tensile samples cut from the pre-deformed parent crystals had dimensions of approximately 2.5mm x 2.8mm x 23 mm. Thus, there is a big difference of sample size. Therefore, we must consider how the difference of sample size influences the mechanical behavior of single crystal samples. Fig. 4.7 shows true stress – engineering strain characteristic of both large sample and small sample in a magnesium single crystal oriented for basal <**a**>

slip where large and small samples have the same dimensions as a parent crystal and a secondary tensile sample and the initial orientation of the sample for size effect is the same as that of crystal B, with the Schmid factor for basal <**a**> slip of 0.49. It was found that the difference of sample size gave rise to the elastic-plastic transition region and large sample exhibited sharpe elastic – plastic transition. The yield stress of large sample was smaller by about 0.1 MPa than that of small sample however, the work hardening rate during the onset of plastic flow was the same in both samples.

In addition to the sample size effect, we must consider recovery (annealing) effect at room temperature because latent hardening test involves unloading and sample cutting processes. Magnesium single crystals (dimensions: 3mm x 26mm x 120mm) oriented for basal <**a**> slip (Schmid factor for basal slip = 0.49) were prepared for the recovery test that includes unloading and annealing of the sample at room temperature during 24 hours, as shown in Fig. 4.8. Fig. 4.9 (a) shows true stress – engineering strain curve resulted from the recovery tests at room temperature using the sample oriented for basal <**a**> slip. In this study, $\Delta\sigma$ is defined as the recovery effect at room temperature, where $\Delta\sigma$ is equal to $\sigma_A - \sigma_B$ or the difference between the yield stress in the test after annealing and final flow stress of the sample before annealing. Fig. 4.9 (b) shows the recovery effect plot $\Delta\sigma$, as a function of σ_A the yield stress of the sample before annealing at room temperature. The recovery effect at room temperature was approximately constant ~ 0.3MPa. The crystal A (the Schmid factor for basal <**a**> slip = 0.42) showed also recovery effect at room temperature. However, the effect was larger and equal to about 0.3 MPa, in this case.

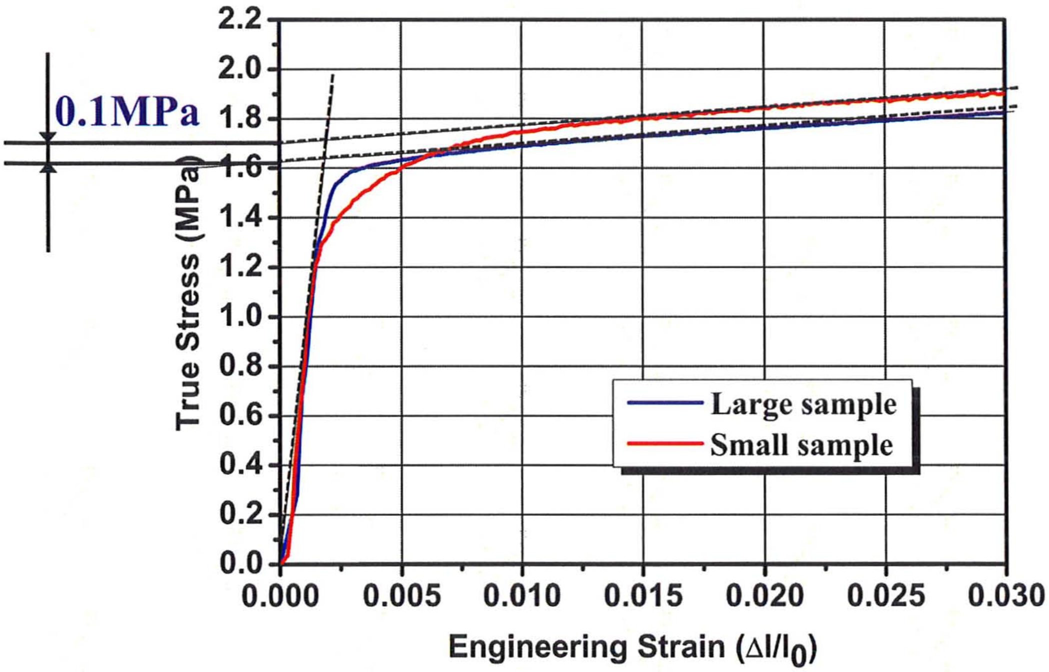

Fig. 4.7 The difference of mechanical properties arising from the sample size. Large and small samples have the same dimensions as a parent crystal and a secondary tensile sample, respectively.

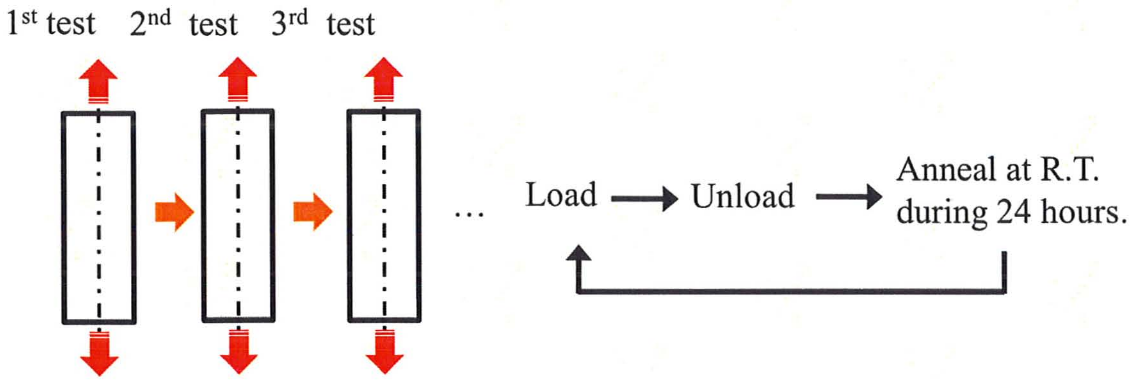

Fig. 4.8 Schematic illustration of recovery test procedure.

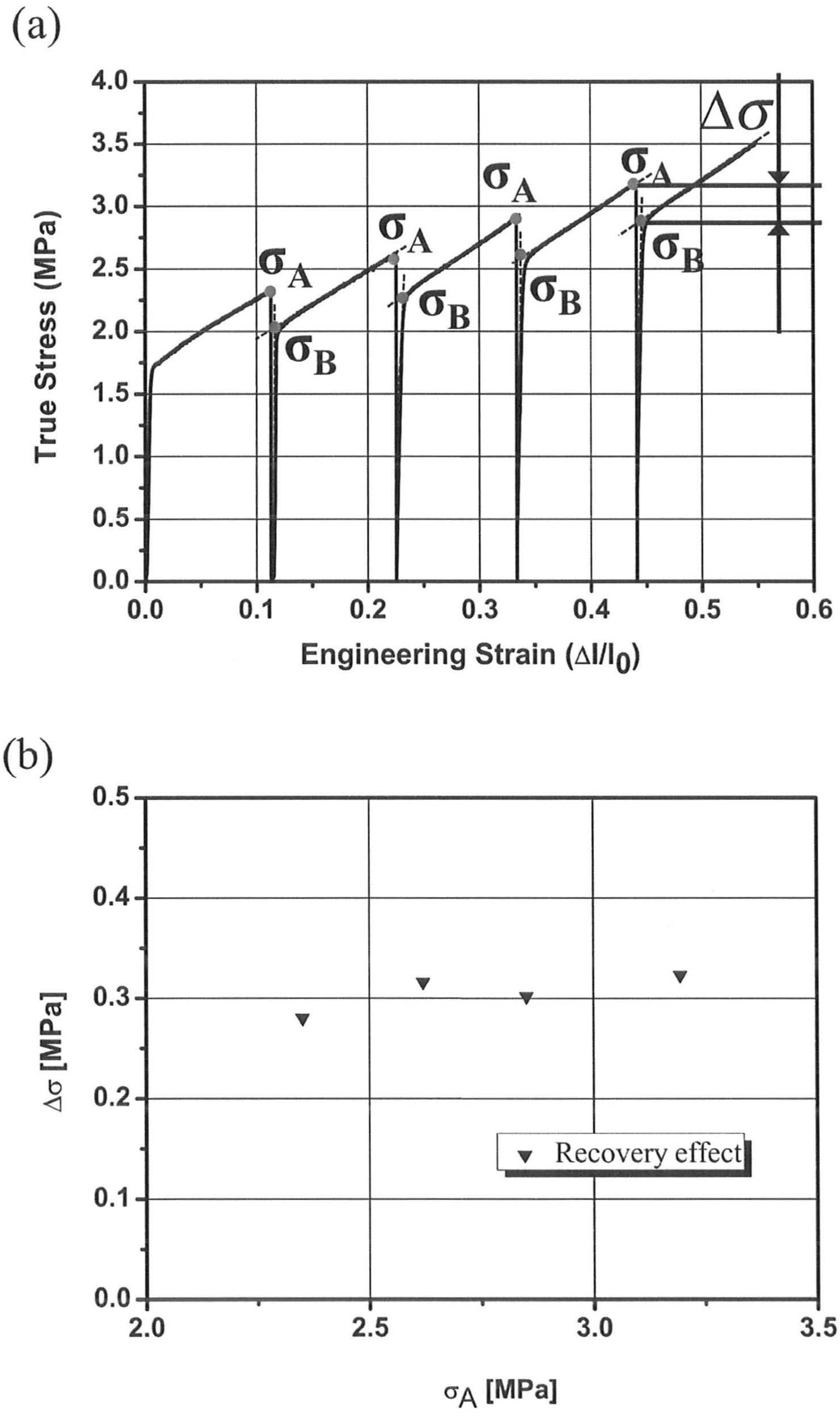

Fig. 4.9 Recovery effect, $\Delta\sigma = f(\sigma_A)$, in the sample oriented for basal slip at room temperature.

4.3.1 Latent hardening behavior in coplanar system.

Fig. 4.10 shows the hardening behavior of parent crystal B and secondary sample B2T. Secondary sample B2T was cut at 0^o from pre-deformed parent crystal B. As shown in Table 4.2, the Schmid factor for basal <**a**> slip in both parent crystal B and secondary sample B2T were 0.49 and homogeneous deformation by single basal slip occurred in both tensile tests. The flow stress of secondary sample B2T was lower than that of parent crystal B. As discussed earlier, we must take into account the size and recovery effect. The blue curve indicates the flow stress of secondary sample B2T after correcting the sample size and recovery effects. Following by latent hardening tests in FCC crystals, the latent hardening ratio (LHR), which is defined as σ_2/σ_1 or the ratio of the yield stress in the secondary test over final flow stress in the primary test, was calculated after correcting for the size effect and recovery effect at room temperature. As a result, the LHR in coplanar system, for basal – basal dislocation interaction, was very close to unity.

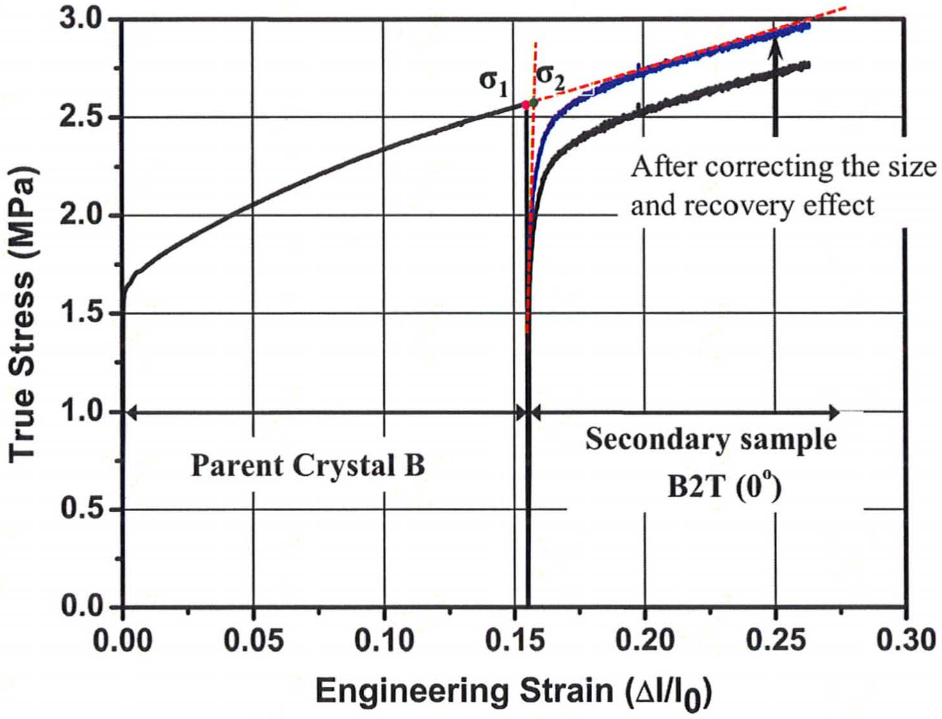

Fig. 4.10 Latent hardening behavior in coplanar system obtained from parent crystal B and secondary sample B2T.

Fig. 4.11 shows latent hardening behavior from parent crystal A and secondary sample A3T. Secondary sample A3T was cut at 0° from pre-deformed parent crystal A. As shown in Table 4.2, the Schmid factor for basal <**a**> slip in both parent crystal A and secondary sample A3T were 0.42. The main deformation mode was basal <**a**> slip. Optical observations revealed small amount of $\{10\bar{1}2\}$ twins formed in both parent crystal A and secondary sample A3T. Similar to Fig. 4.10, the blue curve indicates the flow stress of secondary sample A3T after correcting for sample size and recovery effects. In this case, LHR was about 0.8, smaller than 1. We must consider not only the size effect and the recovery effect at room temperature but also other softening mechanism that may operate in A3T sample. These softening mechanisms seem to be related to inhomogeneous deformation of parent crystal A and secondary sample A3T. In chapter 5, other softening mechanism related to inhomogeneous deformation will be discussed.

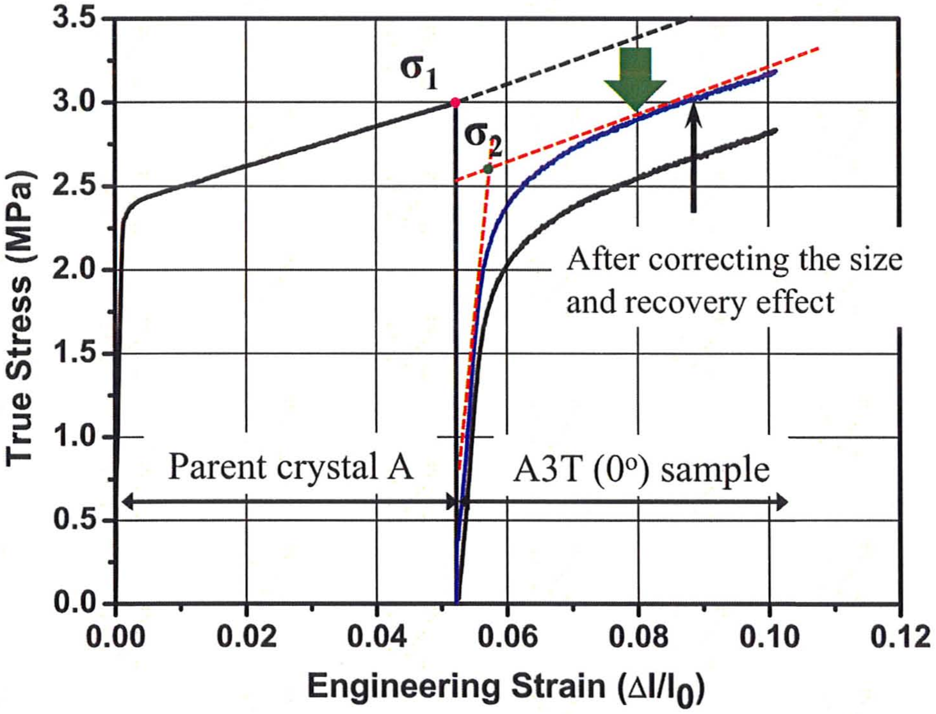

Fig. 4.11 Latent hardening behavior in coplanar system obtained from parent crystal A and secondary sample A3T.

Fig. 4.12 shows hardening behavior of parent crystal A and secondary samples A2T and A3T. As shown in Table 4.2, the slip direction in secondary sample A2T was different from parent crystal A. Let us compare flow stresses in A2T and A3T samples. Work hardening rate in A2T was different from A3T. However, the yield stress of A2T was very closed to that of A3T. Therefore, there was little effect on LHR when the slip direction shifted to different direction. We should note that the Schmid factor for basal

<**a**> slip in parent crystal A is ~ 0.42, causing inhomogeneous deformation. The latent hardening test from parent crystal A and secondary sample A3T will be discussed in the next section.

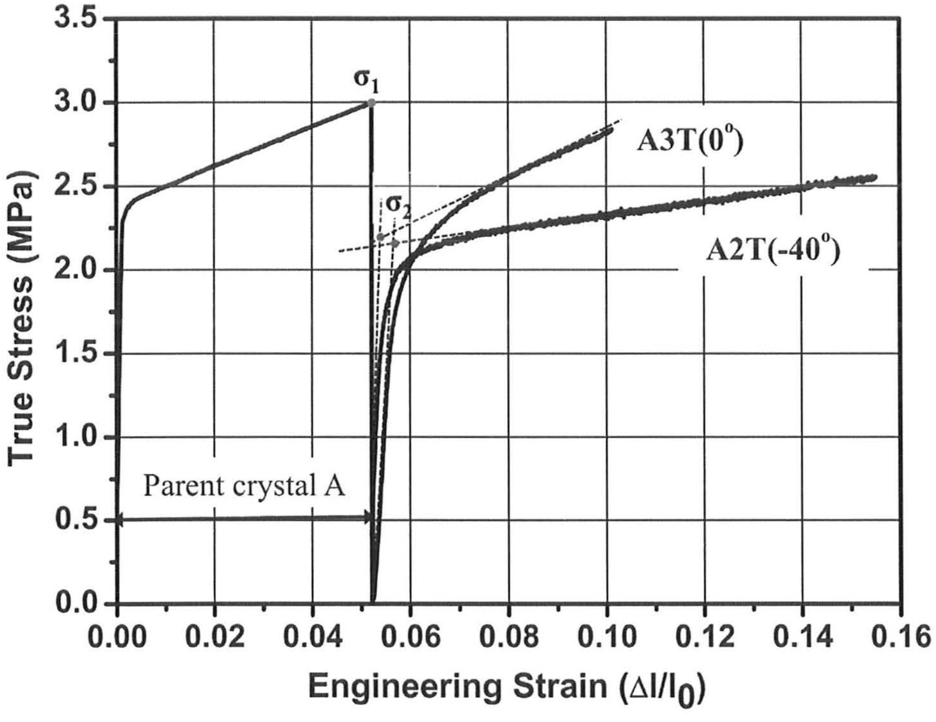

Fig. 4.12 The effect of shifting slip direction in parent crystal A, secondary samples A2T, and A3T samples.

4.3.2 Latent hardening behavior in non-coplanar system

Secondary sample was cut at an angle 70° to the tensile axis of predeformed parent crystal B. As shown in Table 4.2, the Schmid factor for basal <**a**> slip in the parent crystal B was 0.49, while the Schmid factor for basal <**a**> slip in the secondary sample B1T was 0. This indicates that tensile direction in secondary sample B1T is parallel to **a**-axis of the hexagonal lattice. It is well known that when tensile stress parallel to the **a**-

axis is applied in a magnesium single crystal, 2nd order pyramidal <**c**+**a**> slip occurs. Therefore, in this experiment one can obtain information about latent hardening behavior in non-coplanar system, namely the interaction between basal <**a**> dislocations and 2nd order pyramidal <**c**+**a**> dislocations. Fig. 4.13 shows latent hardening behavior from parent crystal B and secondary sample B1T. When slip system shifted from basal slip to 2nd order pyramidal slip, the mechanical property dramatically changed. In the case of basal – 2nd order pyramidal dislocation interaction, LHR was about 15.

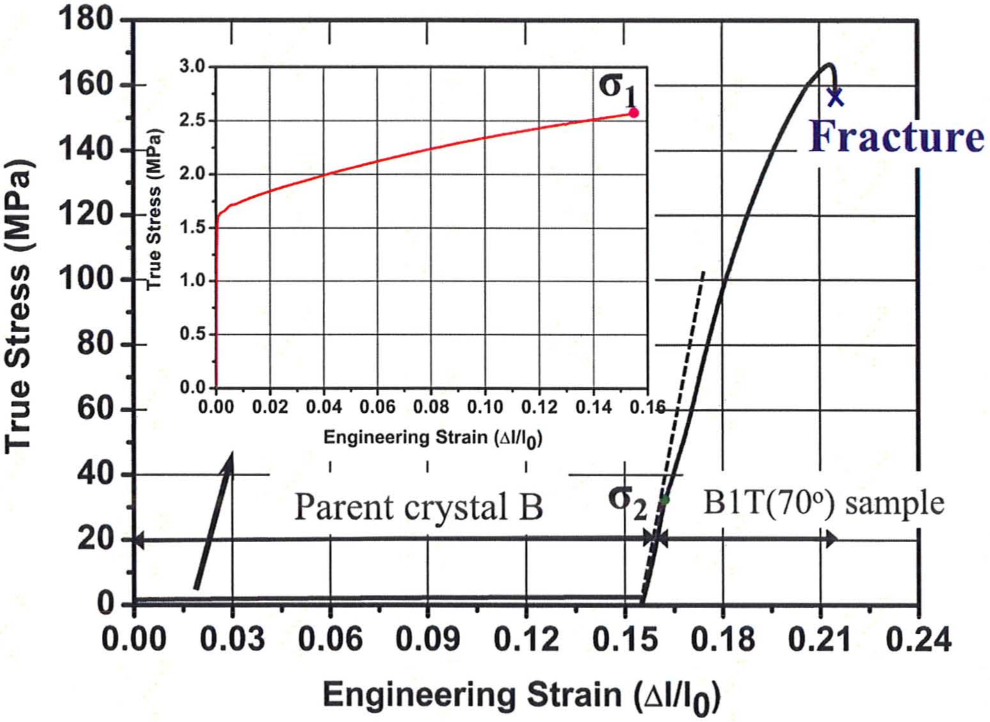

Fig. 4.13 Latent hardening behavior in non-coplanar system obtained from parent crystal B and secondary sample B1T.

4.4 Secondary tensile tests in crystal C

In parent crystal C, it was difficult to activate basal <a> slip in the initial stage of deformation because the Schmid factor for basal <a> slip is very low, 0.17. The main deformation mode was kink band formation and $\{10\bar{1}2\}$ twinning. During deformation, the orientation of the tensile axis rotated by 20° – 30° and basal slip and $\{10\bar{1}2\}$ twins occurred simultaneously. As a result, many $\{10\bar{1}2\}$ twins were induced in parent crystal C during the primary test. Secondary samples were cut at various angles from pre-deformed crystal C. Table 4.4 shows the Schmid factor for basal <a> slip system in C type secondary sample calculated from the initial orientation in parent crystal C and the anticipated slip system or twin mode. One should keep in mind that one could not trust the criteria based on the basal Schmid factor calculated from the initial orientation because the orientation was rotated 20 – 30° locally during deformation in the primary test. Furthermore, we should keep in mind that in this case the secondary samples are no longer single crystals but contain some $\{10\bar{1}2\}$ twin boundaries and they might be regarded as polycrystalline magnesium samples. However, one can study the interaction between various slip dislocations and $\{10\bar{1}2\}$ twin dislocations by using the secondary samples cut from pre-deformed parent crystal C.

Table 4.4 Schmid factors for basal <a> slip system in C type secondary samples.

Parent crystal		C	
Secondary samples	C1	C2	C3
Cutting angle	0°	40°	90°
Basal 1= (0001)[11-20]	-0.19	-0.48	0.10
Basal 2=(0001)[-2110]	0.19	0.09	0
Basal 3=(0001)[1-210]	0	0.38	-0.10
Remarks	Tension twin	Basal slip	2nd py. slip

4.4.1 Secondary sample C1T

Fig. 4.14 shows mechanical properties of secondary sample C1T and parent crystals A, B, and C. Secondary sample C1T was cut at 0° from pre-deformed parent crystal C. Mechanical property of secondary sample C1T was very similar to parent crystal C. At first, heterogeneous deformation by kink band formation and $\{10\bar{1}2\}$ twin occurred. During deformation, the orientation was changed. As a result, after 6% of strain both basal slip and $\{10\bar{1}2\}$ twin were activated. SEM/EBSD analysis was conducted on the wide surface in secondary sample C1T. Fig. 4.15 (a) shows inverse pole figure (IPF) map constructed from EBSD data from the region in which twins are activated in the C1T sample. The microstructure consists of many matrix and twin interfaces. Fig. 4.15 (b) shows 0001 and $2\bar{1}\bar{1}0$ pole figures obtained from the same area. It is clear that there is the crystallographic relationship between two regions indicated as M (matrix) and T (twin), corresponding to 86° orientation relationship. The interface is classified as $\{10\bar{1}2\}$ twin boundaries. From the misorientation profile plot (Fig. 4.16) obtained from the line A – A', the orientation relation between T_1 and T_2, marked in Fig. 4.15 (a), was the $(\bar{1}012)$ and $(10\bar{1}2)$ twins, as shown in Fig. 4.17. Fig. 4.18 shows IPF map, grain boundaries map, and 0001 and $2\bar{1}\bar{1}0$ pole figures from the kink band boundary accompanied by many twins. From grain boundary map, kink band boundaries were essentially low angle tilt boundaries, which produce a rotation of the matrix about the **a**-axis of shear. Near the kink boundaries, the $\{10\bar{1}2\}$ twins were observed.

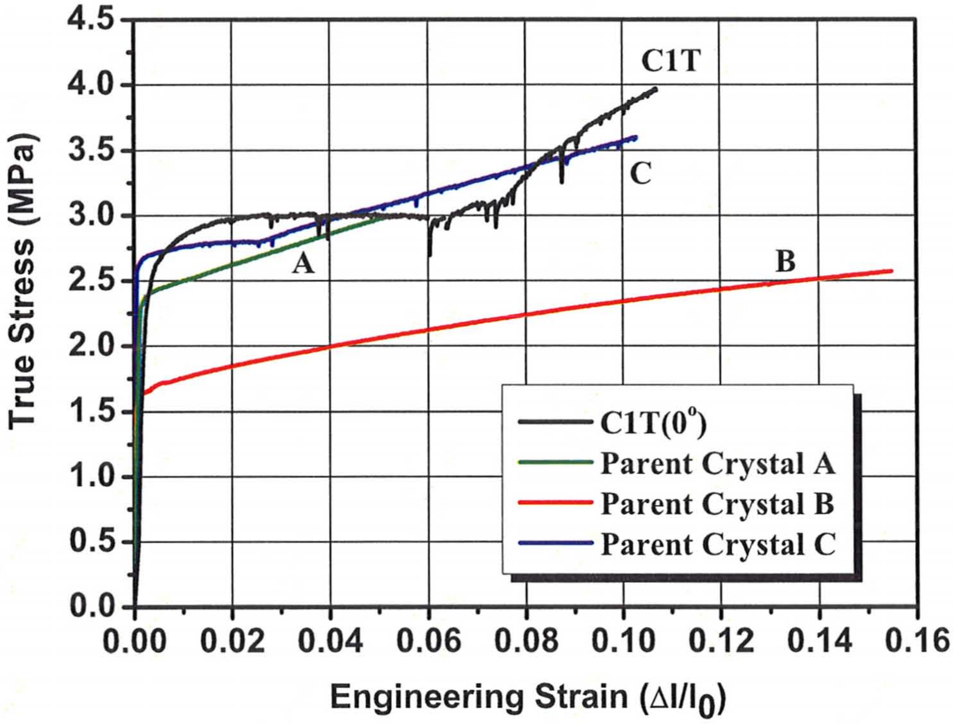

Fig. 4.14 True stress – engineering strain characteristic of the secondary sample C1T and parent crystals A, B, and C.

(a)

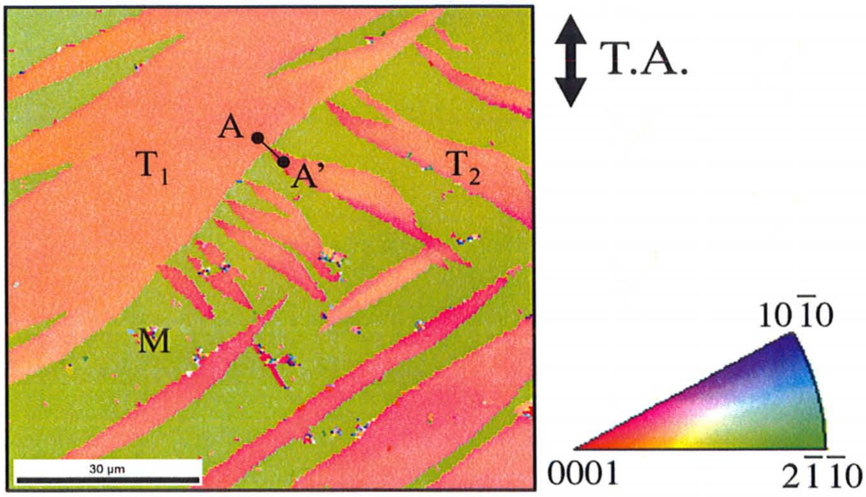

(b)

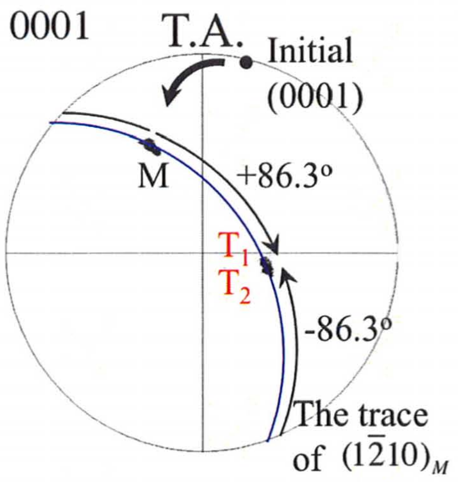

Fig. 4.15 (a) Inverse pole figure (IPF) map, (b) corresponding 0001, and $2\bar{1}\bar{1}0$ pole figures constructed from EBSD data in C1T sample. Black line shows the trace of 0001 pole in the matrix, red line shows the trace of 0001 pole in the twins, blue line shows the trace of the common $2\bar{1}\bar{1}0$ pole between the matrix and the twins, and blue circle shows the common $<11\bar{2}0>$ axis between the matrix and the twins.

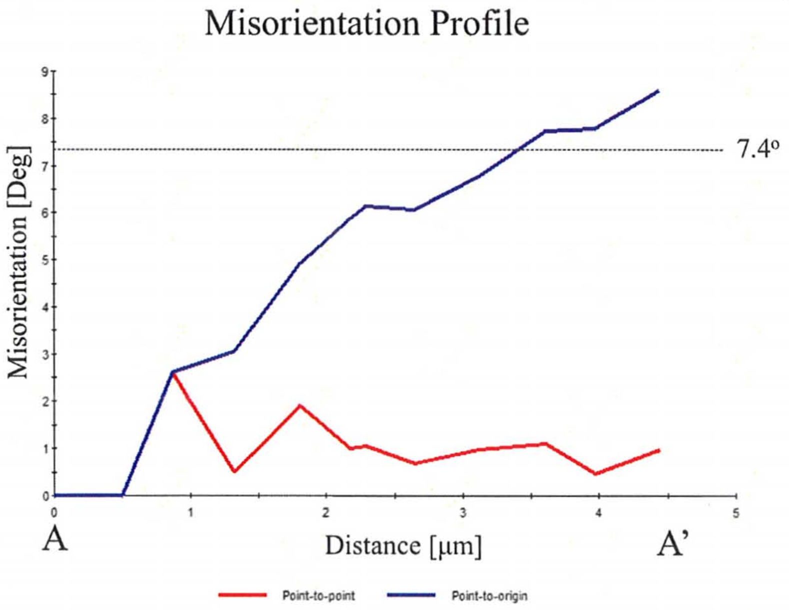

Fig. 4.16 Misorientation profile plot obtained from the line A-A' in Fig. 4.15 (a).

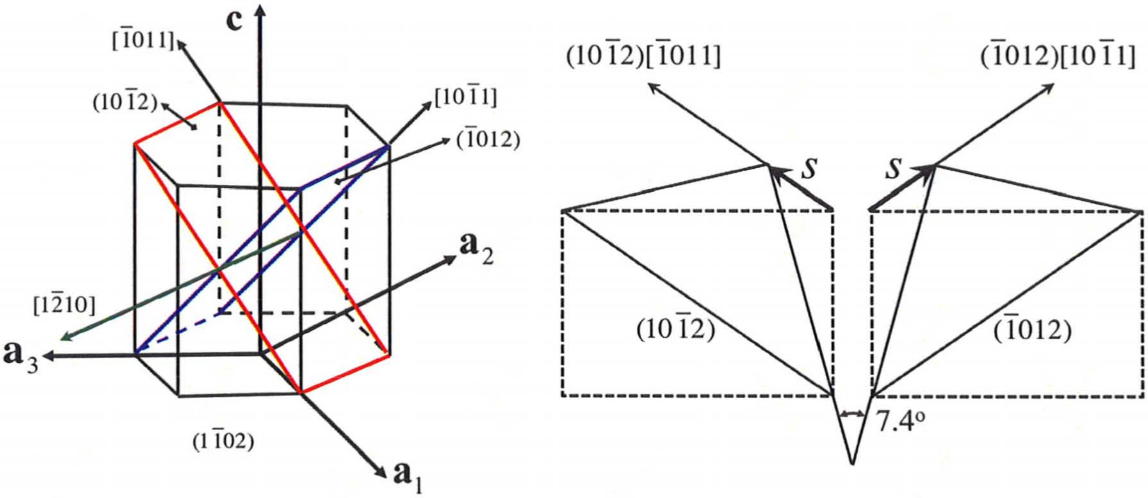

Fig. 4.17 Schematic diagram of the ($\bar{1}$012) and (10$\bar{1}$2) twins in the common plane of shear. The orientation difference between two lattices in the twins can be described by a simple rotation in this plane of 7.4°.

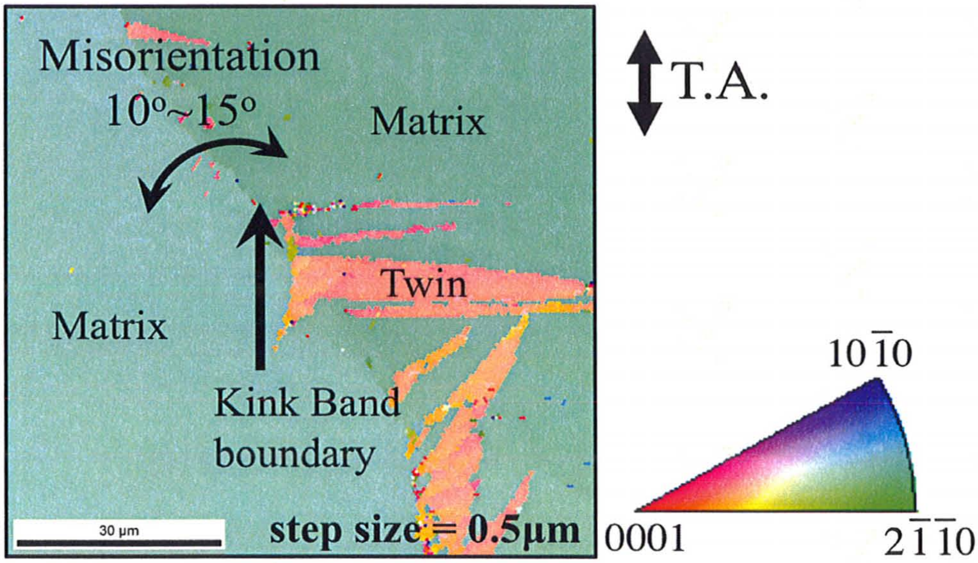

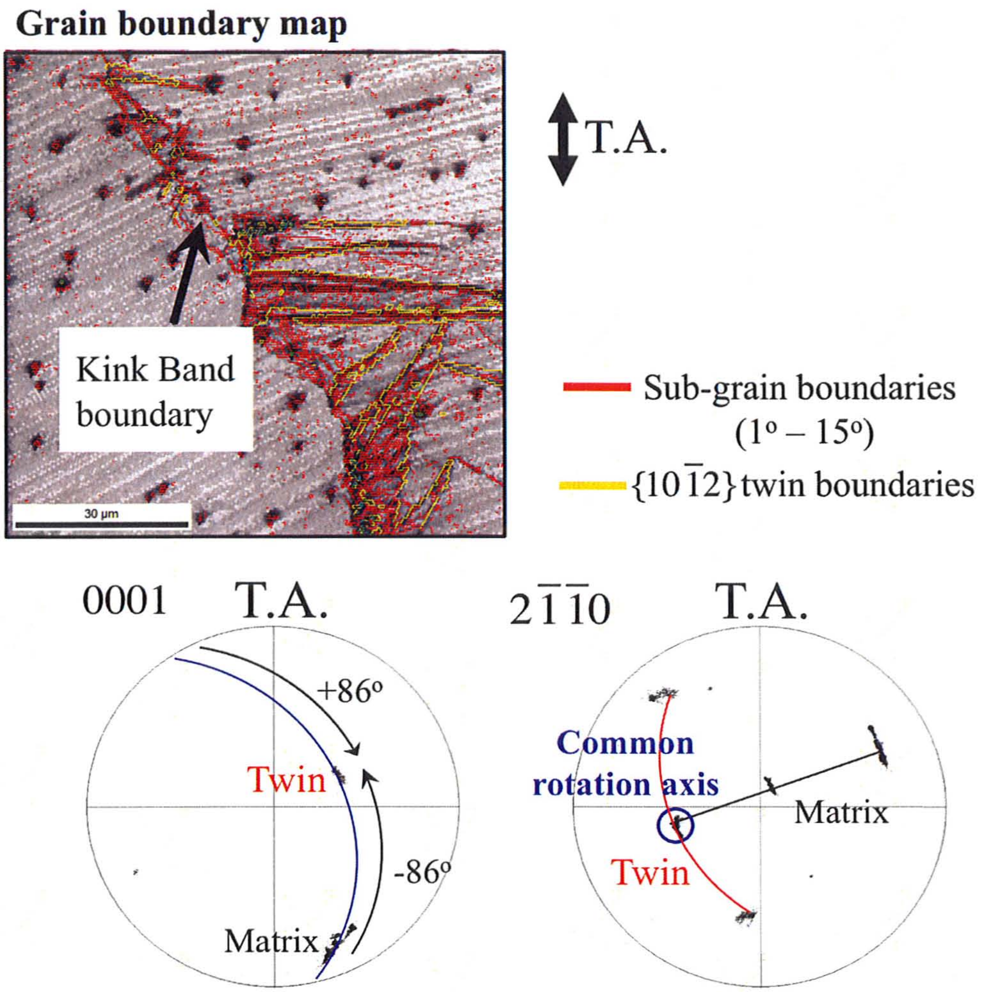

Fig. 4.18 Inverse pole figure (IPF) map, grain boundaries map, and corresponding 0001, $2\bar{1}\bar{1}0$ pole figures near the kink band boundaries constructed from EBSD data in C1T sample. Black line shows the trace of 0001 pole in the matrix, red line shows the trace of 0001 pole in the twins, blue line shows the trace of the common pole between the matrix and the twins, and blue circle shows the common axis between the matrix and the twins.

4.4.2 Secondary sample C2T

Fig. 4.19 shows mechanical properties of secondary sample C2T and parent crystals A, B, and C. Secondary sample C2T was cut at 40° from pre-deformed parent crystal C. The mechanical property of secondary sample C2T was characterized by rapid work hardening and fracture at the early stage of deformation. SEM/EBSD analysis was conducted on the side surface in secondary sample C2T. Fig. 4.20 shows inverse pole figure (IPF) map, 0001, $2\bar{1}\bar{1}0$ pole figures constructed from EBSD data from the region in C2T sample. In 0001 pole figure, it was found that 0001 pole of matrix after deformation was almost parallel to normal direction (ND), which means tensile axis was almost parallel to **a**-axis of hexagonal lattice. This proves that pyramidal fracture takes place in C2T sample. One should pay attention to the interaction between 2^{nd} order pyramidal <**c**+**a**> dislocations and $\{10\bar{1}2\}$ twin dislocations. In the case of secondary sample A5T and B1T oriented for 2^{nd} order pyramidal <**c**+**a**> slip, pyramidal fracture occurred at 3% strain and 6% strain, respectively. However, pyramidal fracture of secondary sample C2T occurred in the later stage of deformation, about 10% strain. This phenomenon is likely to be related to the role of $\{10\bar{1}2\}$ twin boundaries in the fracture process and it will be discussed in chapter 5.

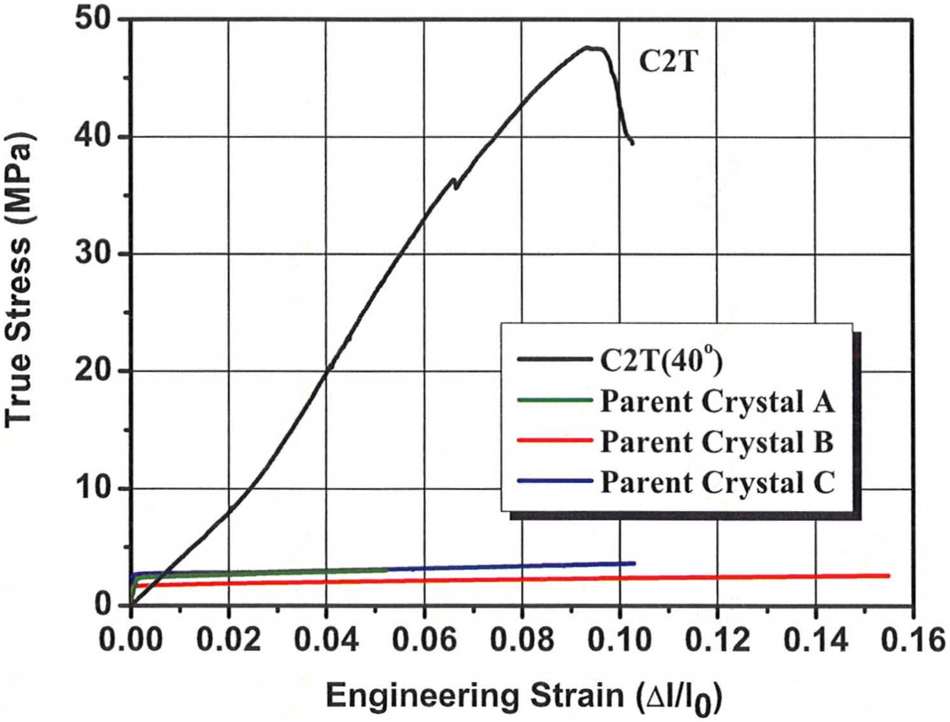

Fig. 4.19 True stress – engineering strain characteristic of the secondary sample C2T (40°) and parent crystals A, B, and C.

(a)

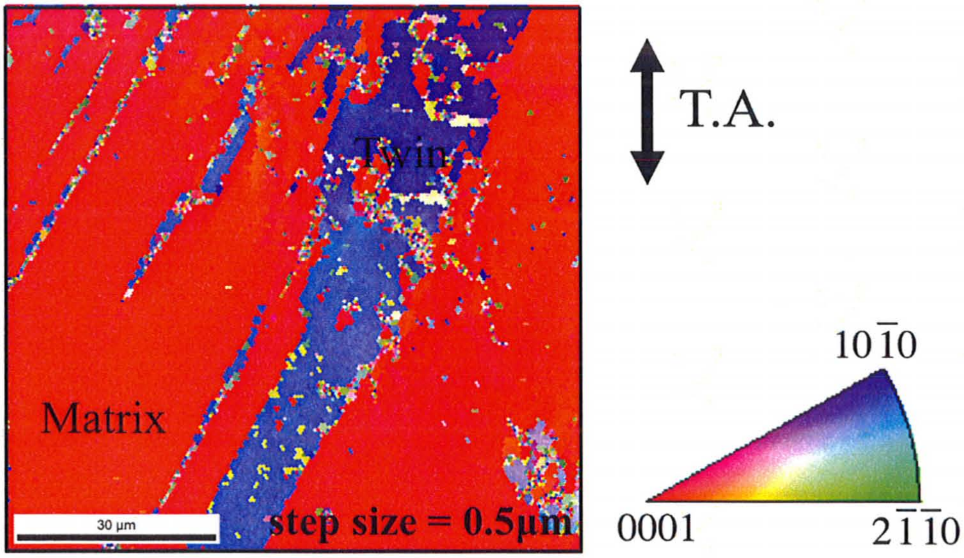

(b)

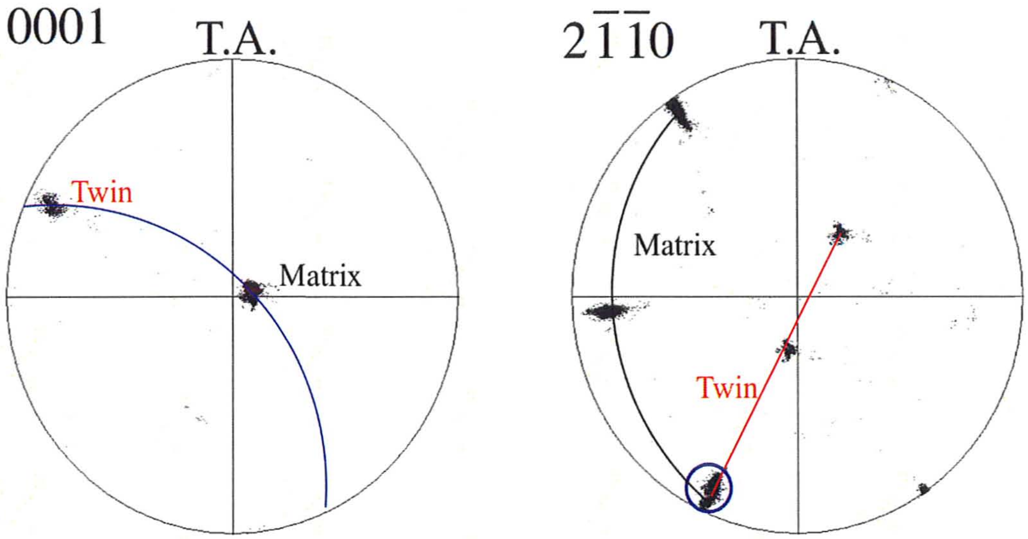

Fig. 4.20 (a) Inverse pole figure (IPF) map, (b) corresponding 0001, and $2\bar{1}\bar{1}0$ pole figures constructed from EBSD data in C2T sample. Black line shows the trace of 0001 pole in the matrix, red line shows the trace of $2\bar{1}\bar{1}0$ pole in the twins, blue line shows the trace of the common $2\bar{1}\bar{1}0$ pole between the matrix and the twins, and blue circle shows the common $<11\bar{2}0>$ axis between the matrix and the twins.

4.4.3 Secondary sample C3T

Fig. 4.21 shows the mechanical properties of secondary sample C3T and parent crystals A, B, and C. Secondary sample C3T was cut at 90° from pre-deformed parent crystal C. Compared to mechanical properties of single crystals (parent crystals A, B, and C), the yield stress of secondary sample C3T was slightly larger, 3.1MPa, and secondary sample C3T had very rapid work hardening rate. This result suggests that $\{10\bar{1}2\}$ twin boundary induced by primary test may influence the mechanical properties of secondary sample C3T. In order to understand this behavior, microtexture on the wide surface in C3T was observed by SEM and the orientation after deformation and twinning type were determined by SEM/EBSD technique. Fig. 4.22 shows SEM images from the region in which there are twin boundaries by pre-straining in the C3T sample and from the region in which there is no twin boundaries by pre-straining in the C3T sample. In Fig. 4.22, the black arrowheads show primary twin boundaries induced by the primary test. It was found that many secondary twins, shown as the white arrowheads, take place inside primary twin. In addition, basal slip is activated in the matrix and in the secondary twins. Fig. 4.23 (a) and (b) show inverse pole figure (IPF) map and 0001 and $2\bar{1}\bar{1}0$ pole figure constructed from EBSD data, respectively. In the pole figures, the misorientation between matrix and primary twin along the common (rotation) axis was 86^{o}, indicating that the primary twin type was $\{10\bar{1}2\}$ twin. Similarly, the misorientation between primary twin and secondary twin along the common (rotation) axis was 86^{o}, indicating that primary twin type was also $\{10\bar{1}2\}$ twin. Fig. 4.24 (a) shows SEM image from the area inside primary twin and Fig. 4.24 (b) shows IPF map from the same area constructed from EBSD data. Ternary twin that is $\{10\bar{1}2\}$ twin type was observed inside secondary twin.

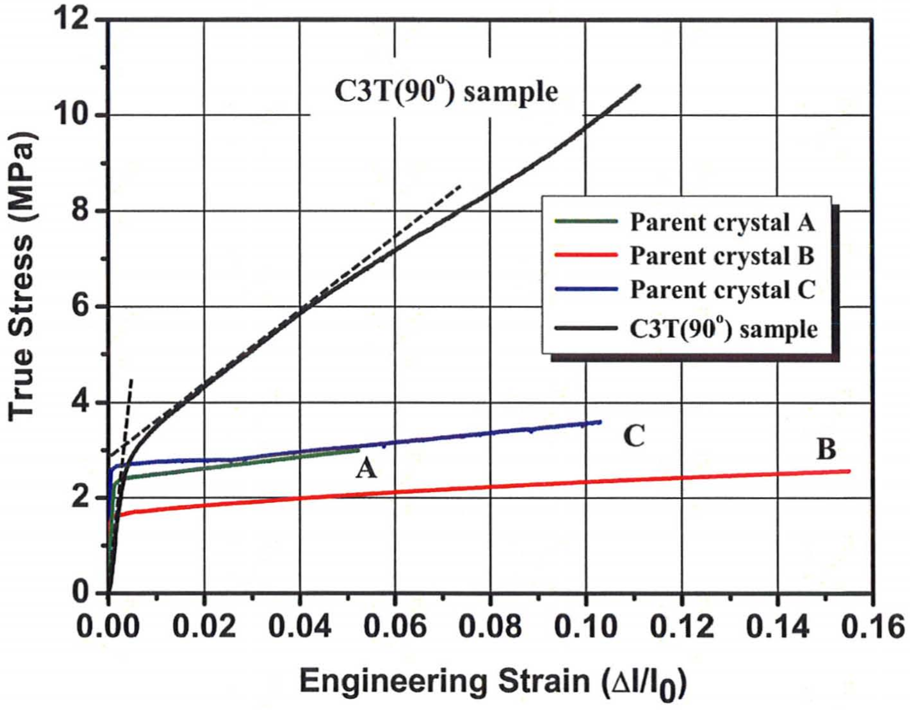

Fig. 4.21 True stress – engineering strain characteristic of the secondary sample C3T (90°) and parent crystals A, B, and C.

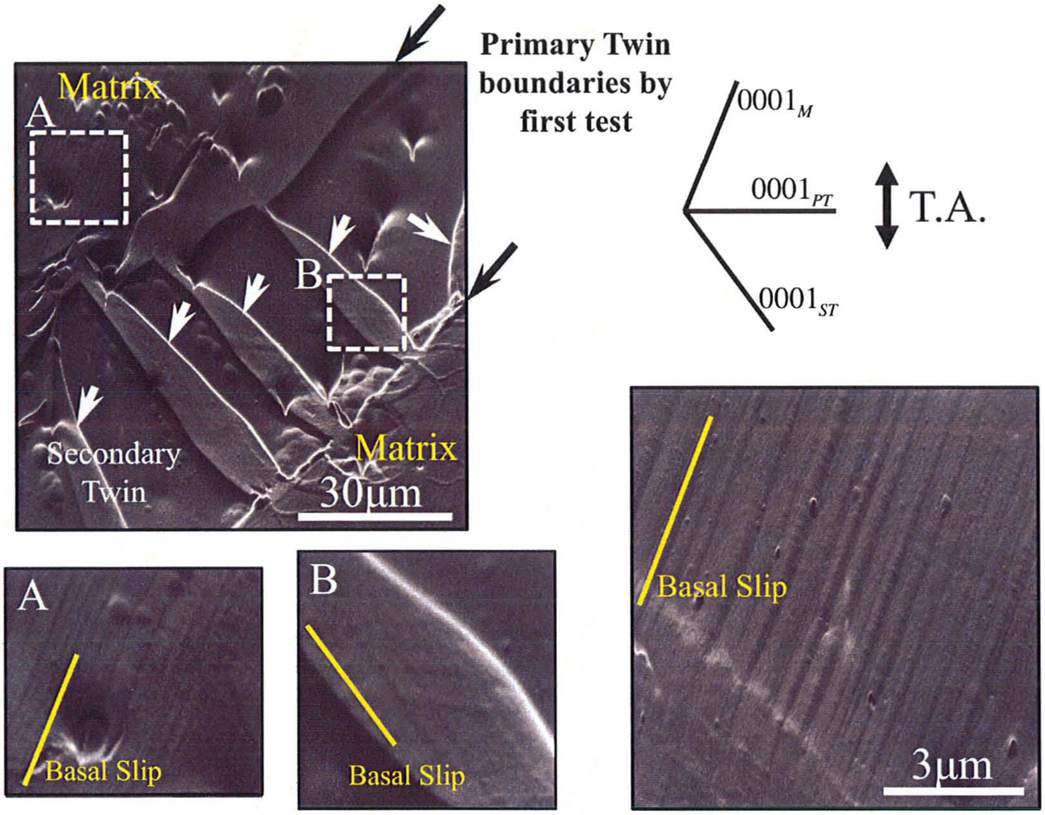

Fig. 4.22 SEM images from the region in which secondary twins, shown as the white arrowheads, take place inside primary twin in C3T sample.

(a)

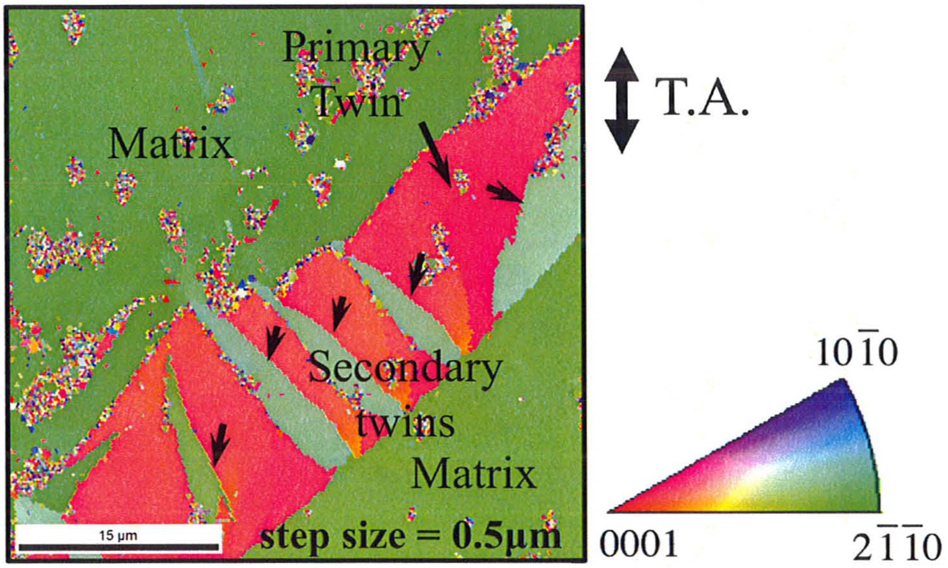

(b)

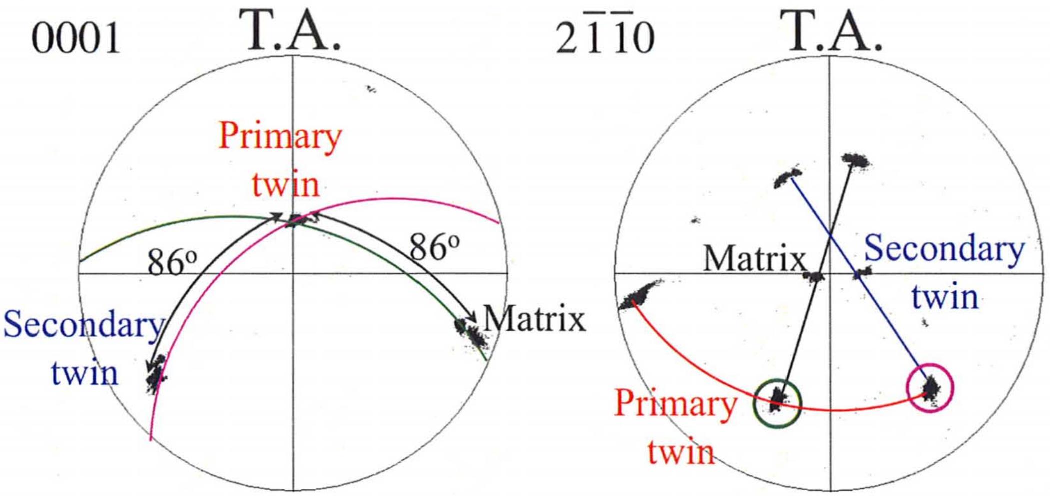

Fig. 4.23 (a) Inverse pole figure (IPF) map, (b) corresponding 0001 and $2\bar{1}\bar{1}0$ pole figures constructed from EBSD data in C3T sample. Black line shows the trace of 0001 pole in the matrix, red line shows the trace of 0001 pole in the primary twins, blue line shows the trace of 0001 pole in the secondary twins. In $2\bar{1}\bar{1}0$ pole figure, green circle indicates the common axis between matrix and primary twin and pink circle indicates the common axis between primary twin and secondary twin. In 0001 pole figure, green curve shows the trace of the common axis between matrix and primary twin, corresponding to green circle in $2\bar{1}\bar{1}0$ pole figure. Similarly, pink curve shows the trace of the common axis between primary twin and secondary twin.

(a)

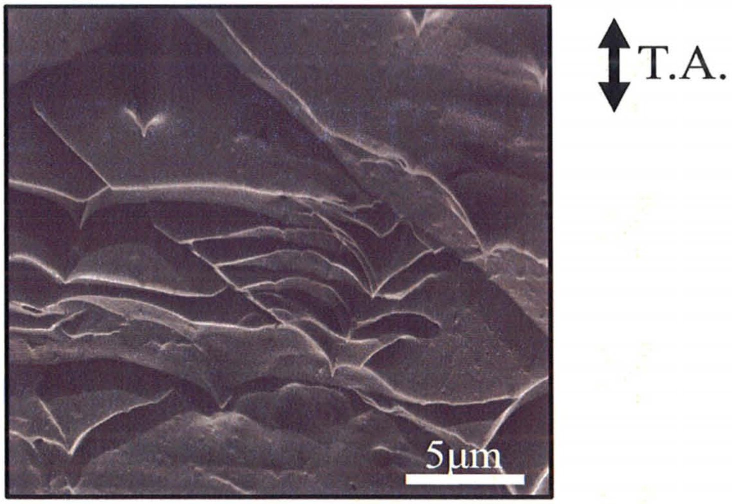

(b)

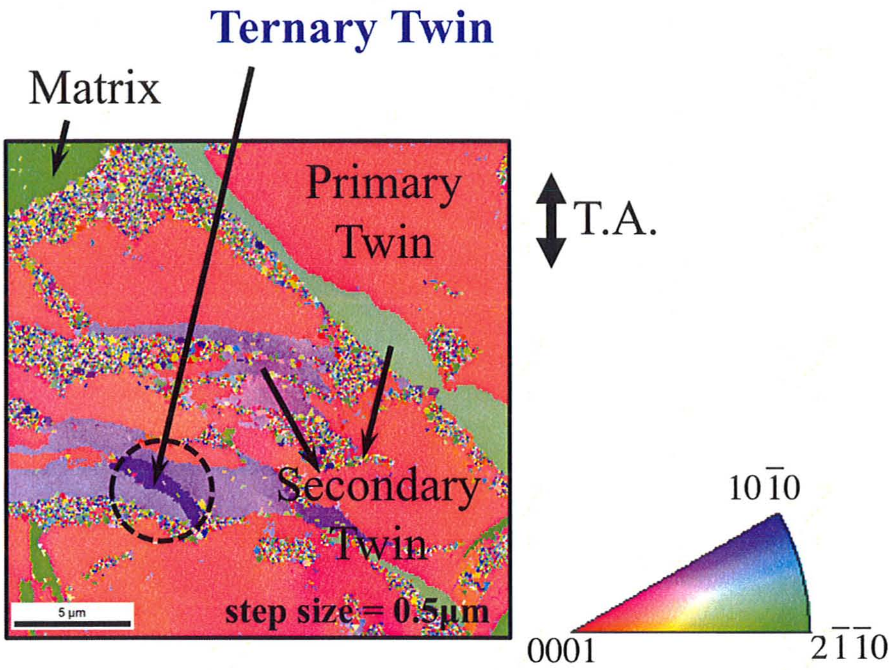

Fig. 4.24 (a) SEM image and (b) IPF map from the area inside primary twin constructed from EBSD data.

Chapter 5 Discussion

5.1 Latent hardening behavior in crystals A and B

Latent hardening tests were carried out using large magnesium single crystals oriented for basal <**a**> slip and secondary tests with samples cut at any directions from the pre-deformed large single crystals. The latent hardening ratio (LHR), which is a parameter to characterize latent hardening behavior, in coplanar system and non-coplanar system was calculated. In previous studies, latent hardening tests in HCP crystals were carried out by means of a pure shear test (Edwards *et. al.*, 1953; Edwards and Washburn, 1954; Phillips Jr. and Robertson, 1958; Phillips Jr., 1961). The authors were not able to measure LHR in non-coplanar system of magnesium single crystals due to severe sample shape restriction as described in section 2.4. Recently, Ando *et. al.* (1992, 2000) observed that 2nd order pyramidal <**c**+**a**> slip was active preferably when the sample was deformed in tension in the direction of $[2\bar{1}\bar{1}0]$ i.e. along the **a**-axis in a magnesium single crystal. In the present work, the latent hardening behavior in non-coplanar systems was studied for the first time under conditions when the parent crystal was deformed in tension by basal single slip and then the secondary sample was deformed in tension by 2nd order pyramidal <**c**+**a**> slip.

The present results show that there is a clear distinction between the latent hardening of coplanar system and forest system. The LHR in coplanar system, for basal – basal dislocation interactions, was very close to unity. On the other hand, the LHR in non-coplanar system, for basal – 2nd order pyramidal dislocations interaction was about 15. These results show good agreement with the general features of latent hardening in FCC crystals, where it is known that the LHRs of non-coplanar systems are generally greater than those of the coplanar system, as reviewed in section 2.5.

In the case of the dislocation interaction in coplanar system of magnesium single crystals, LHR was close to unity and independent of pre-strain, similar to the behavior of copper single crystals where dislocations were subjected to coplanar interactions (Jackson and Basinski, 1965). It follows from this finding that dislocation arrangements formed by the primary test do not produce strong obstacle structure to new gliding basal dislocations during secondary tests. Yoshinaga and Horiuchi (1962) reported that the mean spacing of basal slip bands observed in the early stage of deformation was $10^{-3} – 10^{-4}$ cm. Therefore, the interactions of the parallel dislocations on the basal planes separated by relatively large distance cause only small obstructing stress to moving dislocations and the new gliding dislocations can easily overcome the obstacles produced by the first test and there is no effect of large strain hardening.

The effect of shifting slip direction on basal plane was investigated by parent crystal A and secondary sample A2T (See Fig. 4.12). These results revealed that there is no differences between the yield stress of secondary sample A2T and that of secondary sample A3T, where the tensile axis of secondary sample A3T is parallel to that of parent crystal A. Therefore, it is concluded that when only the slip direction is changed within the same glide plane, i.e. when coplanar dislocations are interacting, these interactions do not contribute to large strain hardening.

In contrast, the most outstanding feature of the results is that magnesium has considerably high LHR in non-coplanar system, ~ 15, compared to FCC crystals. It is well known that in FCC crystals, the LHR of system that forms Lomer – Cottrell sessile locks is the highest in latent hardening tests. The LHR in this case is at most 2.5 in stage I for copper single crystals (Jackson and Basinski, 1965) and ~ 1.6 – 2.2 in stage I for aluminum single crystals (Franciosi *et. al.*, 1980). In order to understand this result, it is important to consider the characteristics and the mobility of 2nd order pyramidal <**c**+**a**> dislocations. Generally, a dislocation with a Burgers vector <**c**+**a**> tends to reduce its energy by dissociation or decomposition. Previous studies have discussed this effect and proposed some dissociation reaction mechanisms.

Ando *et. al.* (1992) observed dislocation distributions obtained from magnesium foils stretched a few percent strain in the $[2\bar{1}\bar{1}0]$ direction at temperatures ranging from 77K to 293K by transmission electron microscopy. According to their TEM studies from the deformed sample at 293K, <**c**+**a**> dislocations with edge components tend to decompose into <**a**> and <**c**> perfect dislocations by a thermally activated process. The dissociated <**a**> dislocations, which have extremely high mobility, can slip easily. However, the dissociated <**c**> perfect dislocation cannot slip by applied stress in the **a**-axis tension and is left as sessile dislocations on the pyramidal plane. This suggests that the sessile <**c**> dislocation can act as strong obstacles to other dislocations movement and influence on the mechanical behavior of the sample. On the other hand, <**c**+**a**> dislocations with screw components can cross-slip onto new slip planes and <**c**+**a**> screw dislocations have relatively high mobility. Compared to lower temperature sample, 133K with room temperature sample, 293K, the immobilization of <**c**+**a**> dislocations becomes more frequent with increasing temperature. At the same time, <**c**+**a**> screw dislocations are forced to double cross slip to propagate slip bands with the assistance of an applied stress. Recently, Ando *et. al.* (1996) studied the core structures of <**c**+**a**> edge dislocation by molecular dynamics (MD) simulation based on Lennard – Jones type inter-atomic potential in order to support the mechanism obtained from their TEM observation. The

<**c**+**a**> edge dislocation has two stable core structures at 0K: one type is the perfect dislocation and the other is two 1/2<**c**+**a**> partial dislocation. However, the core of <**c**+**a**> edge dislocation becomes sessile due to the core structure change, in which the core extends parallel to the basal plane, as temperature increases, resulting in very low mobility of the <**c**+**a**> edge dislocation. The TEM study of the **c**-axis compression sample of magnesium single crystals by Obara *et. al.* (1973) supports the mechanism that Ando and his group have suggested. They also observed the dissociation of <**c**+**a**> edge dislocations into the <**a**> and <**c**> perfect dislocations in the **c**-axis compression sample.

Stohr and Poirer (1972) observed other kinds of partial dislocations in the **c**-axis compression sample represented by the following dislocation reaction:

$$\frac{1}{3}[11\bar{2}3] \rightarrow \frac{1}{6}[20\bar{2}3] + \frac{1}{6}[02\bar{2}3] \ldots \text{(5.1)}.$$

Frank and Nicholas (1953) showed the Shockley type reaction on the 2nd order pyramidal plane given by equation (5.1) based on a hard-sphere model and they also recognized that this dissociation may be sessile due to the corrugated nature of the slip plane.

The situation of latent hardening test is more complex because we must take into account the influence of dislocation arrangements lying on the primary plane. As a further study, TEM observation in secondary sample B1T and the determination of dislocation characteristics will be necessary in order to understand how the dislocation distributions produced by the first test influence on latent hardening behavior in non-coplanar system.

5.2 Selection of crystal orientation for latent hardening test in magnesium

LHR in a coplanar system obtained from type A crystal (parent crystal A and secondary sample A3T) is 0.8, after correcting for effect of sample size and the recovery effects at room temperature. It is considered that inhomogeneous deformation occurs in parent crystal A and secondary sample A3T because the Schmid factor for basal <**a**> slip in parent crystal A and A3T sample was 0.42. As a result, small amount of $\{10\bar{1}2\}$ twins were observed in both parent crystal A and A3T sample. Early studies in HCP crystals such as magnesium (Vohringer, 1970; Rohatgi *et. al.*, 2001), zirconium (Kaschner *et. al.*, 2006) and titanium (Kalidindi *et. al.*, 2003) have shown that twinning can have a softening effect. When the twinning is activated, the slip planes unfavorably oriented for basal <**a**> slip can be reoriented to more favorable orientations, resulting in structural softening. A secondary sample A3T and also other secondary samples for basal orientation, that is A1T, A2T, and A4T, showed clearly latent softening phenomena, as shown in Fig. 4.5.

In the experiments of latent hardening in FCC crystals such as copper (Jackson and Basinski, 1965) and aluminum (Kocks and Brown, 1966), latent softening effect has also been observed. Wessels and Jackson (1969) stated that multi-slip on the primary system would cause to softening on a latent system. Later, Franciosi *et. al.* (1980) pointed out that homogeneous deformation by single slip was required to get clear information of the interactions between different slip systems from latent hardening tests in FCC crystals and the activation of multi-slip during primary test should be avoided.

This is also true of latent hardening test in HCP crystals. In order to obtain more accurate information of latent hardening behavior in magnesium, the present author suggests that we should choose both a parent crystal and secondary samples having the orientations where inhomogeneous deformation does not occur, namely the Schmid factor for basal <**a**> slip is closed to 0.5. In the present work, the results from B type crystals were reliable because the Schmid factor for basal <**a**> slip was 0.49, very closed to 0.5 and homogeneous deformation took place by basal single slip in parent crystal B. The information about latent hardening behavior in coplanar system (the same basal system: Basal 2 / Basal 2, namely self hardening) and in non-coplanar system (Basal 2 / 2nd order pyramidal) has already obtained from B type crystals. However, the effect of shifting slip direction on the same basal plane was measured only by parent crystal A (Schmid factor for basal <**a**> slip = 0.42) and secondary sample A2T. In order to obtain more accurate knowledge of the effect of shifting slip direction on the same basal plane, we should use B type crystals as a future work. When the B type secondary sample is cut at - 40° from pre-deformed parent crystal B, Basal 1 system has the maximum basal Schmid factor and the original system, Basal 2, is lower than Basal 1 system, as shown Fig. 5.1 and Table 5.1. Therefore, we can measure the effect of shifting slip direction by parent crystal B and - 40° secondary sample (hereafter, called secondary sample B3).

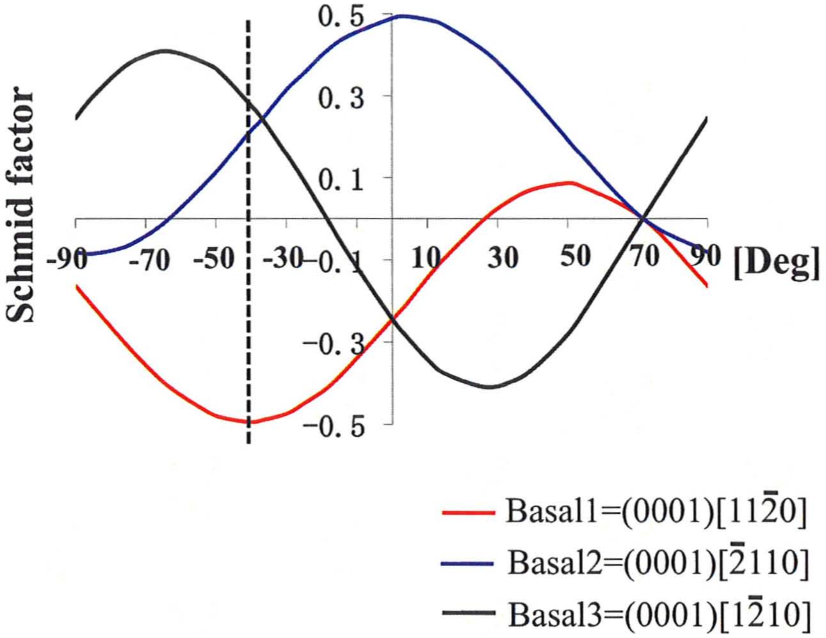

Fig. 5.1 Schmid factor variation for basal slip as a function of cutting angles in parent crystal B.

Table 5.1 Schmid factors for basal slip system in proposed secondary samples and the types of interactions expected to occur between primary dislocation and secondary dislocation.

Parent crystal	B	
Secondary samples	B2	B3 (Proposed sample)
Cutting angle	0°	-40°
Basal 1=(0001)[11-20]	-0.24	**-0.49**
Basal 2=(0001)[-2110]	**0.49**	0.21
Basal 3=(0001)[1-210]	-0.24	0.28
Interaction type Primary / Secondary	B.2 / B.2	B.2 / B.1

As discussed in section 2.3, Ando *et. al.* (1992 and 2000) have confirmed that only 2nd order pyramidal <**c**+**a**> slip is activated when the tensile axis of the sample is exactly parallel to the $<11\bar{2}0>$ direction. However, Yoshinaga and Horiuchi (1963c) reported that prism <**a**>, $\{10\bar{1}0\}<11\bar{2}0>$, slip and 1st order pyramidal <**a**>, $\{10\bar{1}1\}<11\bar{2}0>$, slip were activated principally in the **a**-axis tensile test. Later, Yoshinaga (2009) discussed the difference between experimental results of his and Ando's group in his review paper. The initial orientation of Yoshinaga's sample was not exact in the $<11\bar{2}0>$ direction and about 5° titled towards the $<01\bar{1}0>$ direction. As a result, the Schmid factor for 2nd order pyramidal <**c**+**a**> slip in Yoshinaga's sample became smaller than in the case of exactly in the $<11\bar{2}0>$ direction. For that reason, the difference of favorable slip mode happens. Now, let us consider the secondary samples oriented for 2nd order pyramidal slip, B1T and A5T, dealt with my study. The tensile axis of secondary sample B1T was in the $[\bar{1}2\bar{1}0]$ direction, while the tensile axis of secondary sample A5T was in the $[01\bar{1}0]$ direction, as shown in Fig. 5.2. Table 5.2 show the Schmid factors for basal <**a**> slip system, prism <**a**> slip system and 2nd order pyramidal <**c**+**a**> slip system for secondary samples A5T and B1T. The Schmid factor for prism <**a**> slip and 2nd order pyramidal <**c**+**a**> slip system in secondary sample A5T in which the tensile axis was in the $[01\bar{1}0]$ direction were 0.43 and 0.31, respectively. The surface observations on secondary samples A5T and B1T showed that there were no slip traces corresponding to prism <**a**> slip and 2nd order pyramidal <**c**+**a**> slip in the present work. But, the mechanical behavior of A5T sample was different from that of B1T sample as shown in Fig. 4.6. This may indicate that in the A5T sample multi-slip systems such as prism <**a**> slip, 1st order pyramidal <**a**> slip and 2nd order pyramidal <**c**+**a**> slip were activated, similar to Yoshinaga experiments. Therefore, we must choose the secondary sample where the tensile axis is exactly parallel to **a**-axis of hexagonal lattice to measure latent hardening behavior from the interaction between basal <**a**> dislocation and 2nd order pyramidal <**c**+**a**> dislocation.

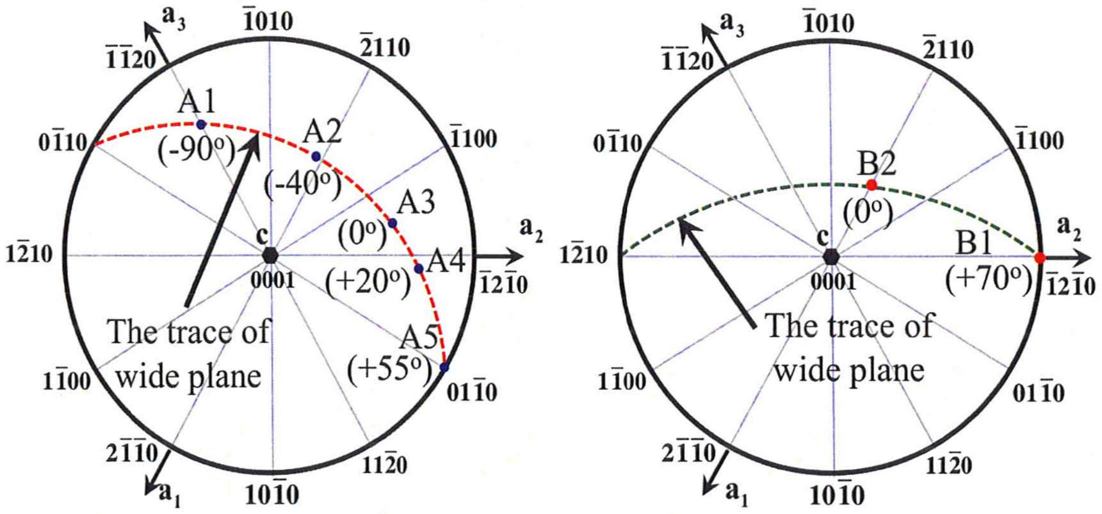

Fig. 5.2 Stereographic projection showing trace of the wide planes of parent crystals A and B (dashed lines) and the orientations of tensile axes of secondary samples (Orientations A1 – A5 and B1 – B2).

Table 5.2 Schmid factors for basal <**a**> slip system, prism <**a**> slip system and 2nd order pyramidal <**c**+**a**> slip system for secondary samples A5 and B1.

Parent crystal Secondary samples Cutting angle	A A5 55°	B B1 70°
Basal 1= (0001)[11-20]	0	0
Basal 2= (0001)[-2110]	0	0
Basal 3 = (0001)[1-210]	0	0
Prism 1=(10-10)[-12-10]	**0.43**	0
Prism 2= (01-10)[-2110]	0	0.43
Prism 3= (-1100)[-1-120]	**-0.43**	-0.43
2nd Py. 1= (11-22)[-1-123]	0.31	0.11
2nd Py. 2= (-1212)[1-213]	0.31	**0.45**
2nd Py. 3= (-2112)[2-1-13]	0	0.11
2nd Py. 4= (-1-122)[11-23]	0	0.11
2nd Py. 5= (1-212)[-12-13]	0.31	**0.45**
2nd Py. 6= (2-1-12)[-2113]	0.31	0.11

5.3 Mechanical properties and deformation textures for magnesium having $\{10\bar{1}2\}$ twin boundaries by pre-straining (Crystal C)

In parent crystal C, inhomogeneous deformation occurred due to a small basal Schmid factor for the basal slip system, 0.17 and many $\{10\bar{1}2\}$ twins were induced in the sample during the primary deformation. The tensile deformation behavior and texture evolution in magnesium with $\{10\bar{1}2\}$ twin boundaries was obtained by using secondary samples cut from the pre-deformed parent crystal C.

Deformation behavior of the secondary sample C1T was very similar to that of the parent crystal C, which was characterized by inhomogeneous deformation with $\{11\bar{2}0\}$ kink bands and $\{10\bar{1}2\}$ twin formations. On the other hand, the deformation behavior of the secondary samples C2T and C3T were completely different to that of parent crystal C. In the following, the mechanical properties of C2T and C3T samples will be discussed.

- Basal <**a**> dislocation – $\{10\bar{1}2\}$ twin dislocation interactions

Secondary sample C3T was cut at 90° from pre-deformed parent crystal C. In the sample, many secondary $\{10\bar{1}2\}$ twins were formed inside primary twin boundaries formed by the first test and basal <**a**> slip bands were observed both in the matrix and in the secondary twins. As a result, the work hardening of secondary sample C3T was more rapid than that of the single crystal oriented for basal <**a**> slip. The present results reveal that $\{10\bar{1}2\}$ twins largely contribute to strain hardening of magnesium. One of the reasons is that the $\{10\bar{1}2\}$ twin boundaries can act as obstacles to moving dislocations.

Another reason is that the $\{10\bar{1}2\}$ twinning can reduce the effective grain size resulting in strengthening the material by Hall-Petch mechanism (Hall, 1951; Petch, 1953):

$$\sigma = \sigma_0 + kD^{-1/2} \ldots (5.2)$$

,where σ is the flow strength, σ_0 is the friction stress and k is the stress intensity constant. The latter is supported by the present result and many early studies. In the present work, the secondary twins were observed in the primary twin boundaries and the ternary twins were observed in the secondary twins. To put it another way, when higher order $\{10\bar{1}2\}$ twins are produced in the sample, the grain size of the sample becomes smaller producing larger strain hardening effect. On the other hand, there are still unclear questions about the interaction between moving basal <**a**> dislocation and $\{10\bar{1}2\}$ twin dislocation. Basinski *et. al.* (1997) observed that in a Cu – 8%Al alloy, twinning propagated in the late stage of deformation and found that the twin boundaries transform glissile dislocations into sessile dislocations inside twins and this contributes to strain hardening due to the trapping of the sessile dislocations. Some researchers have applied Basinski *et. al.* mechanism to magnesium (Barnett *et. al.*, 2004, 2005, and 2007; Xu *et. al.*, 2005; Caceres *et. al.*, 2008) in order to describe the mechanism of strain hardening due to $\{10\bar{1}2\}$ twinning. Caceres *et. al.* (2008) explain the mechanism as described below. "$\{10\bar{1}2\}$ twinning turns basal plane into prismatic plane and vice versa, that is, when $\{10\bar{1}2\}$ twinning propagates, basal <**a**> dislocations will lie on the harder prism planes, while prism <**a**> dislocations will lie on the softer basal planes, thereby balancing the respective hardening and softening effects. If Basinski *et. al.* mechanism is also applied to magnesium, basal <**a**> dislocations should be more numerous than prism <**a**>

dislocations." However, nobody has provided experimental proof to support Basinski *et. al.* mechanism in magnesium. Therefore, the understanding to dislocation reactions around $\{10\bar{1}2\}$ twin boundaries in secondary sample C3T remains as one of the main issues to be clarified.

- 2nd order pyramidal <**c**+**a**> dislocation – $\{10\bar{1}2\}$ twin dislocation interaction

Secondary sample C2T was cut at 40° from pre-deformed parent crystal C. The mechanical property of C2T sample was characterized by rapid work hardening and fracture in the early stage of deformation. As written in section 4.4.2, 2nd order pyramidal <**c**+**a**> slip is considered to be activated in C2T sample. Fracture happened in B1T sample oriented for 2nd order pyramidal <**c**+**a**> slip at 6% strain, while fracture took place in C2T sample in the later stage of deformation, 10% strain. In the following, the role of $\{10\bar{1}2\}$ twin boundaries induced by primary test in the ductility and the fracture process of magnesium will be discussed.

Yoo (1969) studied the energetic feasibility of a dislocation at a twin boundary in HCP crystals based on the energy criteria associated with the anisotropic energy factors. As a result, the interaction between basal <**a**> dislocation and $\{10\bar{1}2\}$ twin is repulsive in magnesium and this indicates that a local stress concentration occurs at the twin interface and twin interfaces can be the source of <**c**+**a**> dislocation. Recently, Agnew *et. al.* (2002) confirmed the enhancement of 2nd order pyramidal <**c**+**a**> dislocation activity near the twin boundaries from TEM study in magnesium polycrystalline sample and magnesium – 10 at% Lithium alloy sample. In the present work, the interaction between basal <**a**> slip dislocation and $\{10\bar{1}2\}$ twin dislocation in the primary tensile test with parent crystal C produced many sources of <**c**+**a**> dislocation and the activation of 2nd order pyramidal <**c**+**a**> dislocation in the C2T sample was easily occurred compared to the secondary sample B1T.

Finally, the selection of C type secondary samples will be described below. In parent crystal C, inhomogeneous deformation took place and the middle part of crystal C was locally bent and twisted due to $\{11\bar{2}0\}$ kink band formation and many $\{10\bar{1}2\}$ twins. As a result, the orientations of parent crystal C and the density of $\{10\bar{1}2\}$ twins after tensile deformation are quite different depending on the location of the sample.

The advantage of C type secondary samples is that we can study the simple interaction between various slip dislocations and $\{10\bar{1}2\}$ twin dislocation in magnesium. The interactions between basal <**a**> dislocation and $\{10\bar{1}2\}$ twin dislocation or 2nd order pyramidal <**c**+**a**> dislocation and $\{10\bar{1}2\}$ twin dislocation were obtained from secondary samples C2T and C3T. But, the simple comparison among the results of the C type secondary samples is very ambiguous. In the future work, we must take into account the orientations of the secondary samples, the volume fractions of $\{10\bar{1}2\}$ twins and their density after the primary test to better explain the hardening effect arising from $\{10\bar{1}2\}$ twinning in magnesium.

Chapter 6 Conclusions

In the present work, latent hardening tests in magnesium single crystals were carried out for the first time in research history and the latent hardening ratio in magnesium determined by measuring the flow stresses in the different tests. The most important conclusions arising from this work are as follows:

1. The latent hardening ratio (LHR) for basal – basal dislocation interactions is very close to 1.
2. The LHR for basal – 2nd order pyramidal plane dislocation interactions is appoximately 15.
3. Homogeneous deformation by basal single slip in the primary test is required to obtain correct LHRs in magnesium single crystals. Otherwise, latent softening phenomena occurs during the secondary tests.
4. The deformation in the parent crystal C was inhomogeneous and occurred by kink bands formation and $\{10\bar{1}2\}$ twinning. Complex dislocation interactions with forest dislocations and $\{10\bar{1}2\}$ twins were observed in the latent hardening experiments based on the C typed samples.
5. $\{10\bar{1}2\}$ twin boundaries induced by pre-straining in the primary test significantly influenced the hardening behavior of the secondary samples. It is concluded that the hardening behavior arises, at least in part, from a dynamic Hall-Petch contribution. Further studies are required to elucidate Basinski's hardening contribution to the hardening behavior of twinned magnesium.

References

Agnew S.R., Horton J.A., and Yoo M.H., (2002), Metal. Mat. Trans. A, **33A**, 851.

Akhtar A. and Teghtsoonian E. (1969a), Acta Metall. **17**, 1339.

Akhtar A. and Teghtsoonian E. (1969b), Acta Metall. **17**, 1353.

Akhtar A. and Teghtsoonian E. (1972), Phil. Mag. **25**, 897.

Alden T.H., (1963), Acta Metall., **11**, 1103.

Alden T.H., (1964), Trans. AIME, **230**, 649.

Ando S., Nakamura K., Takahashi K., and Tonda H., (1992), J. Jpn. Inst. Light Met., **42**, 765.

Ando S., Takashima K., and Tonda H., (1996), Mater. Trans., **37**, 319.

Ando S. and Tonda H., (2000), Trans. JIM, **41**, 1188.

Ando S., Goto T., and Tonda H., (2002), Metal. Mat. Trans. A, **33A**, 823.

Asada H. and Yoshinaga H., (1958), J. Jpn, Inst. Met., **23**, 67.

Asada H. and Yoshinaga H., (1959), J. Jpn, Inst. Met., **23**, 649.

Baird J. D. and Gale B., (1965), Phil. Trans. R. Soc., **A257**, 553.

Barnett M.R., Nave M.D., and Bettles C.J., (2004), Mat. Sci. Eng. A, **A386**, 205.

Barnett M.R., Keshavarz Z., and Beer A.G., (2004), Acta Mater., **52**, 5093.

Barnett M.R., Davies C.H.J., and Ma X., (2005), Scripta Mater., **52**, 627.

Barnett M.R., (2007), Mater. Sci. Eng. A, **A464**, 1.

Basinski Z.S., (1960), Aust. J. Phys., **13**, 284.

Basinski Z.S., Szczerba M.S., and Niewczas M., (1997), Rev. Metall., **94**, 1037.

Bhattacharya B., (2006), Ph. D. Thesis, McMaster University.

Burke E.C and Hilbbard W.R Jr., (1952), J. Metals, Trans. AIME, **194**, 295.

Caceres C.H., Lukac P., and Blake A., (2008), Phil. Mag., **88**, 991.

Chou J., Shimauchi H., Ikeda K., Yoshida F., and Nakajima H., (2005), J. Jpn. Inst. Light Met., **55**, 131.

Edwards E.H., Washburn J., and Parker E.R., (1953), Trans. AIME, **197**, 1525.

Edwards E.H. and Washburn J., (1954), Trans. AIME, **200**,1239.

Engler O. and Randle V., (2009), Introduction to Texture Analysis (2nd Edition), CRC Press.

Franciosi P., Merveiller M., and Zaoui A., (1980), Acta Metall., **28**, 273.

Franciosi P. and Zaoui A., (1982), Acta Metall., **30**, 1627.

Franciosi P., (1985), Acta Metall., **33**, 1601.

Frank F.C. and Nicholas J.F., (1953), Phil. Mag., **44**, 1213.

Groves G. W. and Kelly A., (1963), Phil. Mag., **8**, 877.

Hall E.O., (1951), Proc. Phys. Soc., **B64**, 747.

Hirsch P.B and Lally J.S, (1965), Phil. Mag., **12**, 595.

Hirth J.P. and Lothe J., (1992), Theory of Dislocation (2nd Edition), Krieger.

Hull D. and Bacon D. J., (2001), Introduction to Dislocations (4th Edition), Elsevier Butterworth-Heinemann.

Jackson P. J. and Basinski Z. S., (1967), Can. J. Phys., **45**, 707.

Kainer K.U., (2003), Magnesium Alloys and Technologies, Wiley-VCH.

Kalidindi S.R., Salem A.A., and Doherty R.D., (2003), Adv. Eng. Mater., **5**, 229.

Kaschner G.C., Tome C.N., and Beyerlein I.J., (2006), Acta Metall., **54**, 2887.

Keh A.S. and Nakada Y., (1967), Can. J. Phy., **45**, 1101.

Kelly A., Groves G.W., and Kidd P., (2000), Crystallography and Crystal Defects (Revised Edition), Wiley.

Kocks U.F., (1964), Trans. AIME, **230**, 1160.

Kocks U.F. and Brown T. J., (1966), Acta Metall., **14**, 87.

Lake J.S.H. and Craig G. B., (1972), Scripta Metall., **6**, 1023.

Miura H., Yang X., Sakai T., Nogawa H., Miura S., Watanabe Y., and Jonas J., (2005), Phil. Mag., **85**, 3553.

Miura S., (2004), Hokkaido University, unpublished research.

Miyamoto H., Funami K., and Uehara M., (1977), J. Fac. Eng. Tokyo Univ., **34**, 349.

Nakada Y. and Keh A.S., (1966), Acta Metall., **14**, 961.

Obara T., Yoshinaga H., and Morozumi S., (1973), **21**, 845.

Ohashi T., (1994), Phil. Mag. A, **70**, 793.

Okamoto P.R. and Thomas G., (1968), Phys. Status Solidi, **25**, 81.

Otte H. and Crocker A.G., (1965), **9**, 441.

Partridge P.G., (1967), Met. Rev., **12**, 169.

Petch N.J., (1953), J. Iron Steel Inst., **174**, 25.

Phillips Jr. W.L. and Robertson W.D., (1958), Trans. AIME, **212**, 406.

Phillips Jr. W.L., (1961), Trans. ASM, **54**, 50.

Ramaswami B., Kocks U.F., and Chalmers B., (1965), Trans. AIME, **233**, 927

Reed-Hill R.E. and Robertson W.D., (1957), Acta Metall., **5**, 717.

Reed-Hill R.E. and Robertson W.D., (1957), Trans. AIME, **209**, 496.

Rohatgi A., Vecchio K.S., and Gray III G.T., (2001), Metall. Met. Trans. A, **A32**, 135.

Schmid E. and Boas W., (1935), Kristallplastizat, Springer.

Schwartz A. J., Kumar M., Adams B.L., and Field D.P., (2009), Electron Backscatter Diffraction in Materials Science (2nd Edition), Springer.

Sheely W.F. and Nash R.R., (1960), Trans. AIME, **218**, 416.

Shoeck G. and Frydman R., (1972), Phys. Stat. Sol. B, **53**, 661.

Stohr J.F. and Poirer J.P., (1972), Phil. Mag., **25**, 1313.

Taylor G.I. and Elam C.F., (1925), Proc. Roy., Soc., **A108**, 28.

Tonda H. and Ando S., (2002), Metal. Mat. Trans. A, **33A**, 831.

Von Mises R. and Angew Z., (1928), Math. Mech., **8**, 161.

Vohringer O., (1970), Z. Metall., **67**, 518.

Ward Flynn P., Mote J., and Dorn J.E., (1961), Trans. AIME, **221**,1148.

Washburn J. and Parker E. R., (1952), J. Metals, **4**, 1076.

Wessels E. J. H. and Jackson P.J., (1969), Acta Metall., **17**, 241.

Wessels E. J. H. and Nabarro F. R. N., (1971), Acta Metall., **19**, 903.

Wonsiewicz B.C. and Backofen W.A., (1967), Trans. TMS-AIME, **239**, 1422.

Wu. H., Przystupa. M. A., and Ardell A. J., (1997), Metall. Mat. Trans. A, **A28**, 2353.

Xu S., Gertsman V.Y., and Thompson J.P., (2005), Can. Metall. Q., **44**, 155.

Yang P., Yu Y., Chen L., and Mao W., (2004), Scripta Mater., **50**, 1163.

Yoo M.H., (1969), Trans. AIME, **245**, 2051.

Yoo M.H., (1981), Metall. Trans., **12A**, 409.

Yoo M.H., Agnew S.R., Morris J.R., and Ho K.M., (2001), Mat. Sci. Eng., **A319**, 87.

Yoo M.H., Morris J.R., Ho K.M., and Agnew S.R, (2002), Metall. Mat. Trans. A, **33A**, 813.

Yoshinaga H. and Horiuchi R., (1962), Trans. JIM, **3**, 220.

Yoshinaga H. and Horiuchi R., (1963a), Trans. JIM, **4**, 1.

Yoshinaga H. and Horiuchi R., (1963b), Trans. JIM, **4**, 134.

Yoshinaga H. and Horiuchi R., (1964), Trans. JIM, **5**, 14.

Yoshinaga H., (2009), J. Jpn. Inst. Light Met., **59**, 450.